THE UNIVERSITY OF HULL

Development of a Low-Cost Zinc Oxide-Based Material Hybrid Memristor

being a Thesis submitted for the Degree of Doctor of Philosophy (PhD)

in the University of Hull

by

Robert James Gray, BSc., MSc.

July 2017

Abstract

In recent years, there has been a resurgence of interest in two-terminal resistive devices as a new universal memory, which has the speed of static random access memory (SRAM), simplicity of dynamic random access memory (DRAM) and non-volatile storage of Flash memory. This has arisen from a report in 2008 that links switching in TiO_2 memristor (dubbed the HP memristor) with Leon Chua's memristor theory from 1970. The work importantly helped establish a framework for understanding and developing the field forward, which combined with the potential to scale devices down beyond the limits of complementary metal-oxide semiconductors has stimulated progress, enabling significant improvement in the technology.

In this thesis, we have developed a new material-hybrid zinc oxide (ZnO) nanorod-polymethyl methacrylate (PMMA) memristor fabricated using a novel microwave-based technique that enables devices to be made in a simple, quick and low-cost manner. A study into the growth of the nanowires identifies the significance of a uniform and aligned seed layer in producing dense distributions of aligned and homogeneous nanowire arrays, which is necessary for controlling the properties of the spacing layer and avoiding short-circuits. The rate of heating affects the nanowire growth significantly by inducing the formation of larger crystallites when heating at high power for very short durations, while low-power heating over larger durations reduces the formation of these larger particles.

We also find that the transport mechanisms are dependent on the device configurations. Through electrical I-V measurements, we observe that devices with gold (Au) top and bottom electrodes produce on/off resistance ratios (referring to the ratio of the low resistance state to the high resistance state) of typically around 5 - 8 and exhibit electrical behaviour typical of Poole-Frenkel emission and space charge limited conduction (SCLC). Devices with an aluminium (Al) top electrode and Au bottom electrode typically exhibit on/off ratios of approximately 10 (one order of magnitude), and their on/off ratios are larger than the best achieved with both Au electrodes; these devices typically exhibit Schottky emission behaviour, but do not exhibit clear Poole-Frenkel or SCLC behaviour. Devices using indium tin oxide (ITO) as a bottom electrode typically have on/off ratios of ~5 and appear to be dominated by Schottky emission behaviour.

The introduction of a PMMA layer affects the behaviour of all configurations. None of the transport models clearly fit the data for the Au/ZnO/PMMA/Al configuration; Poole-Frenkel emission and SCLC behaviour can be observed in ITO/ZnO/PMMA/Al devices, with many SCLC regimes being clearly identifiable that were not present in the configuration without PMMA. The additional PMMA layer is observed to affect the SCLC behaviour in Au/ZnO/PMMA/Au configurations, as the device no longer produces the higher-order trap charge limited conduction regime observed in the device without PMMA; the Poole-Frenkel behaviour is also affected, as the change in gradient for the Poole-Frenkel plot indicates that the data fits the “modified Poole-Frenkel effect” model. This suggests that additional trap centres may be created with the addition of a PMMA layer.

This thesis concludes that, while the devices require further optimization (particularly in terms of endurance and retention) to become commercially viable, the technique has much potential for future application.

Thesis Chapter List

Statement of Originality

I hereby declare that the content of this thesis is a product of my own work. Where I have consulted the published work of others, it has been properly referenced and acknowledged.

Acknowledgements

This thesis represents the culmination of over five years in the School of Mathematics and Physical Sciences at the University of Hull. Working on a PhD is an emotional rollercoaster; it can be very exciting when things all fall into place, but can leave you feeling overwhelmed when things don't go as expected, and the repetitive nature of the work can drain the emotion out of you when things don't seem to be progressing despite your best efforts. Here, I wish to thank all those individuals and groups who have supported and inspired me through this long journey – without them, I would not have been able to persevere through to the end of this project.

First, I want to thank Dr. Neil Kemp, my primary supervisor. Your guidance, support and inspiration helped push me through my PhD studies, and your advice and encouragement has continuously pushed me to strive for the best that I can achieve with my PhD. We have, of course, butted heads over aspects of my work in the past, as do all those with a pride and passion for their work. But we finally got there in the end, and our work together has resulted in a few nice papers being published, with a few more pending publication, and we would not have achieved this if we had not worked together. So, thank you.

I would like to thank Dr. Emanuele Verrelli. Your guidance and advice helped me through the early stages of my PhD, when I really had no idea what I was doing. The thorough training you gave me on how to use many of the key pieces of equipment that I have used through much of my project gave me a strong foundation from which

to develop my work, and your reassurance, when everything seemed to be going wrong, helped me to push myself to keep going. Thank you.

I would like to thank Ayoub Hamdiyah, a PhD student who works within my research group. Having another student with whom to discuss key ideas is very helpful, and you helped to give me insight from a different point of view from my supervisors and other academic supporters, that allowed me to approach my project from other perspectives than I might have otherwise. Thank you, and I wish you the best of luck in completing your own PhD and with your future endeavours.

I would like to thank my examiners, Dr. Ali Adawi from the University of Hull, and Dr. Jessamyn Fairfield from the National University of Ireland Galway. The detailed questioning you gave me during my Viva, coupled with the precise and specific notes you gave me for my many, many (many) thesis corrections, allowed me to probe deeper into my work and develop a much stronger understanding, particularly of the underlying mechanics behind the transport mechanisms observed in my work, than I had up to the original submission of my thesis. Thank you both; I hope you are as pleased with the finished result of this thesis as I am proud to have written it.

I would like to thank all of the technical support personnel with whom I have had the privilege of working. I appreciate the hard work each of you put in to making sure students and staff alike are capable of carrying out their work; we cannot thank you enough. Of particular mention are David Stavenau, Robert Knight, Tony Sinclair, and Garry Robinson. Dave, you helped me to construct several of the key pieces of

equipment and apparatus required for my project and were always very happy to go above and beyond where necessary; further to this, you were a person I could always turn to for advice, guidance and support, especially at times when I was feeling overwhelmed. Thanks for putting up with me bothering you all the time!

Bob, you were kind enough to allow me to use your Mars 5 scientific grade microwave. This was key for my studies into the growth of the zinc oxide nanorods, as it allowed control over both the temperature and the pressure within the vials to ensure the best quality of growth that we could achieve. Thank you for making time for me to use it so that I could carry out the work I needed to do, especially given that it is intended for use for your own department (Chemistry) and not really for mine.

Tony Sinclair and Garry Robinson: you both assisted me by allowing me access to your respective scanning electron microscopy (SEM) equipment. While Tony's machine is considerably more powerful than Garry's, both were incredibly useful throughout the course of my PhD studies and I visited them both frequently. In addition to helping me to acquire SEM images of my nanorods and crystallite structures on my samples, both of you were very friendly and accommodating, and went above and beyond – often working a little bit later than they would normally choose to – in order to ensure that I was satisfied with the results we had obtained from the SEM scans. Thank you both so much for what you did for me. And I probably still owe Garry a jar or two of Douwe Egberts Pure Indulgence coffee, for all the times he poured me one while we were waiting for the SEM to pump down…

I would like to thank the University of Hull in general, and the School of Mathematics and Physical Sciences in particular, for allowing me to embark upon my PhD journey, and for the support I have received as I have progressed with my studies. I would also like to thank the staff at the Graduate School, for your continuous support through my studies.

Now for a few special thanks, to people who inspired me and cheered me up in times when I was feeling down, even though some of them have no idea who I am; the things you do, even if they only seem little to you, have had a big impact on my mental and emotional well-being, and I do not consider it an exaggeration to say that I would have struggled to finish my PhD without you.

I would like to thank Bryce Papenbrook , an actor who brings life through his vocal talents to anime and video game characters that I love, and from whom I drew inspiration and courage during some of the toughest times of my PhD studies. I had the privilege of meeting you at an anime convention in 2017, and your enthusiasm, energy and approachable, friendly nature renewed my motivation towards both my life and my work. You also introduced me to “Anime Unlocked” on Facebook, a Closed Group that brings exclusive content from professional voice actors and industry professionals to the fans. Your passion for your work and your appreciation of your fans drive me to strive to be the best I can be, so thank you so much for being who you are!

I also want to thank Cherami Leigh, an amazing actress who, much like Bryce, brings to life many of the characters I love in anime and video games through her incredible voice. You are responsible for bringing love and light into my life (both figuratively and literally – through your show “Love & Light”, which brings a daily dose of positivity that was certainly much needed at many stages through my PhD). Your “Kawaii IRL” series brought a smile to my face on days when I otherwise felt miserable and overwhelmed. Both you and Bryce are responsible for making me laugh through your “CONfessionals” series, on days when I needed an extra lift. I could go on, but this is already a long book. So I’ll just say thank you, for being who you are and doing all the wonderful things you do – I am immeasurably grateful.

Thanks also to Matthew Mercer, actor, Dungeons & Dragons ambassador, and games master on the “Critical Role” web series on Geek & Sundry’s channel. Again, your vocal talents have brought to life many of my favourite characters, and you’ve even worked alongside Bryce and Cherami on some of my favourite shows and video games. You also inspired me to get back into tabletop roleplaying games, especially D&D 5th Edition, giving me a chance to re-explore my creativity and a reason to get together with friends to escape from reality for a few hours. This form of escapism did wonders for my mental and emotional state in ways I don’t think I can adequately express. Thank you so much.

I would like to thank my family and friends, for your continued support in all of my ventures. Without your strength, love, compassion, patience (which they have certainly needed at times, and for which I am also immeasurably grateful), and faith,

I would not have been able to achieve what I have achieved in my studies. In particular, I would like to thank my Dad, Mum, my brother Tom, and my girlfriend, Edwina Gill. I cannot put into words how much your support has meant to me. I would not have even attempted any of this, without each of you guiding me, inspiring me, reassuring me, and ultimately convincing me that I can do this. A copy of this thesis will now be sitting on a shelf, in my house somewhere where everyone can see it, proving all of you right. So thank you.

Symbols and Abbreviations

ZnO	Zinc Oxide
PMMA	Poly(methyl methacrylate)
HMTA	Hexamethylenetetramine
Au	Gold
Al	Aluminium
ITO	Indium Tin Oxide
Zn	Zinc
SEM	Scanning Electron Microscope/Microscopy
AFM	Atomic Force Microscope/Microscopy
XRD	X-ray Diffraction
MIM	Metal-Insulator-Metal
ECM	Electrochemical Metallization
SCLC	Space Charge Limited Conduction

I (i)	Current
V (v)	Voltage
R	Resistance
q	Charge
φ	Flux Linkage
eV	Electron-Volts

Chapter 1

Introduction

This chapter introduces the topic of memristors, non-volatile memory devices based on resistive switching. Throughout this chapter, an historical perspective on memristors is provided, giving a timeline describing the development of resistive switching memory devices that stretches back over two centuries. This will briefly touch upon the theoretical “discovery” of the memristor as a fundamental circuit element, which will be discussed in more detail in Chapter 2.

Zinc oxide is also discussed in this chapter as a semiconductor material that can be produced in a variety of nanostructures through low-cost, simple fabrication procedures. This material’s applications are briefly discussed, and its role as the semiconductor material in our memristor device architecture will be highlighted. Organic/inorganic hybrid material memristors are introduced, and a general outline of the thesis and the research objectives will be provided.

1.1 An Historical Perspective on Memristors

The rapid progression of information technology from analogue to digital has created an urgent need for ever-increasing digital information storage capacity. To meet this demand, industry and academia race to develop the next generation of memory technologies. Flash Memory, a type of electronically erasable and programmable read-only memory (EEPROM) [*1*] whose erasure process is reminiscent of the "flash" of a camera [*2*], is a very well-known and well-established form of memory technology that currently dominates the non-volatile memory market. Non-volatile memory is memory that retains data without the requirement of constant supply of energy, unlike volatile memories such as DRAM (dynamic random-access memory) and SRAM (static random-access memory). While Flash Memory is the current predominant non-volatile memory, it has significant limitations: its lifespan is limited due to the high voltage (typically either 1.8 V or 3.3 V, depending on cell type, to read the cell, and higher voltages applied via charge pump for the erase operation) [*3*] and high power (drawing currents of >20 mA even when idle) [*4*] application of the devices, with Flash Memory devices typically surviving approximately 100,000 read/write cycles; it has comparatively slow read/write speed when compared with DRAM and SRAM; and there are significant limitations to the density of Flash Memory devices that can be packed onto a single chip. This places a limit on the scalability of Flash Memory devices, to which we are rapidly approaching.

At present, Flash is commonly used in combination with DRAM and SRAM to make up for its relative shortcomings in terms of speed and component density (essentially

the number of individual memory devices that can be held on a chip). DRAM is much cheaper to produce, and has greater component density than SRAM, but falls short of SRAM's speed due to the number of transistors involved in the construction of SRAM devices. DRAM (write speed ~50 ns) and SRAM (write speed 1 - 100 ns) are volatile memory, but are significantly faster than Flash (write speed >1 µs). The table in figure 1.1 compares the three memory technologies.

	SRAM	DRAM	NOR Flash	NAND Flash
Non-volatile	No	No	Yes	Yes
Read Time	1 – 100 ns	30 ns	10 ns	50 ns
Write/Erase Time	1 – 100 ns	50 ns	1 µs/ 10 ms	1 µs / 0.1 ms
Endurance (number of cycles)	10^{16}	10^{16}	10^{5}	10^{5}
Write Power	Low	Low	Very High	Very High
High Voltage Required	No	2 V	6 – 8 V	16 – 20 V
Number of Transistors	6	1	1	1

Fig. 1.1: A table comparing SRAM, DRAM and Flash memories. Data source: Wolf et al [*5*].

New forms of non-volatile memory are a key topic of research in the present climate, with a focus on finding a new "universal memory" that would be able to replace the current main forms of storage device listed above, combining the advantages of all three devices while eliminating the disadvantages. One promising form of storage device that has created tremendous interest is the memristor, an emerging technology that combines smaller, scalable two-terminal device architectures with high-speed, low-energy information processing; if it is possible to reliably fabricate memristors of the appropriate densities required for modern data storage purposes

using organic materials, this would significantly reduce the costs to fabricate the devices.

“Memristors” (a portmanteau of “memory” and “resistor”) are “a two-terminal circuit element characterized by a relationship between the charge, q, and the flux-linkage, φ” [*6*]. Charge and flux linkage are time-integrated functions of current and voltage, respectively, and so the relationship between them is analogous to the relationship between current and voltage (which describes electrical resistance); however, as q and φ are both time-integrated functions, the corresponding relationship describes a resistance that depends upon the complete past history of current that has flowed through the device [*6*].

The name “memristor” was first used by Leon Chua in his 1971 article entitled “Memristor – The Missing Circuit Element” [*6*], although memristors – albeit unnamed and unknown at the time – have had their effects documented for over two centuries [*7*]. Early effects of memristors were observed not necessarily in devices intended for electronic data storage; the earliest observation of “the signature property of memristors” [*7*] was Sir Humphry Davy, the inventor of the electric arc and mentor to Michael Faraday. Davy noted that, when two pieces of charcoal are brought very close together and a high potential difference is applied, a “spark” is produced, and if the potential difference is high enough then the spark will be maintained as an arc of electricity [*8*]. Re-examining Davy’s original electric arc experiments from 1800 [*9*], it has more recently been demonstrated [*10*] that the

carbon arc discharge exhibits the three main fingerprints of memristors, which shall be further explained in the next section of this thesis.

In 1960, Bernard Widrow developed a device named the “memistor” [*11*]. This device is a three-terminal device, like a transistor; in a memistor, however, the conductance between two of the terminals is controlled by the time integral of the current in the third, rather than its instantaneous value as is the case in a transistor. This device was based on an electrochemical circuit element and not a solid-state circuit element, making it unsuitable for the concept of an integrated circuit (also known as chips or microchips; small wafers of semiconductor, usually silicon, that can hold a circuit comprised of millions of electrical components [*12*]) that were dominating electronics in the 1960’s [*13*].

In 1967, Simmons and Verderber published an article [*14*] describing the electrical properties of thin insulating films (20 – 300 nm thick) having been formed by injecting gold ions from one of the electrodes. It was found that the devices also exhibited hysteretic resistive switching behaviour, which was attributed to an electron trapping mechanism (a “trap”, in solid state physics, refers to any location within a solid, typically a semiconductor or an insulator, in which the movement of electrons or holes – the equivalent positive charge resulting from the absence of an electron within a crystal structure – is restricted [*15*]). Hysteresis is a property of a system, in this case an electronic system, that occurs when the output of the system is dependent of the history of past inputs [*16*]; in other words, applying the same voltage to a system can yield different output currents, depending on past voltages applied through the history of the device.

In 1970, Leon Chua proposed a new fundamental circuit element, which he named “memristor”, characterized by the relationship between the fundamental circuit variables of charge, q, and flux linkage, φ (this circuit variable represents the amount of magnetic flux, Φ, that passes through (is “linked” with) the surface created by a closed conducting loop, such as a single loop of wire, or a coil of wire [*17*]), a relationship that had previously not been defined. In 1976, Chua published another paper alongside Sung Mo Kang, entitled “Memristive Devices and Systems”, in which memristors are broadly generalized to be a class of non-linear dynamical systems called “memristive systems” [*18*].

Figure 1.2 shows the relationships between the fundamental circuit variables, and the symbols for the circuit elements that represent those relationships.

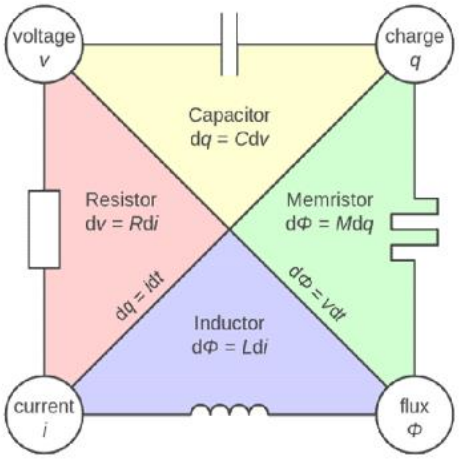

Fig. 1.2: A visual representation of the relationships of the four fundamental circuit elements. The circuit symbols for the resistor, capacitor, inductor and memristor are included along the edges of the square [*19*].

At the time of writing his 1971 paper (and indeed the aforementioned 1976 paper), a memristor in the form of a physical device that did not require an internal power supply had not been discovered. To simulate how a memristor would work, Chua used an *M-R* mutator, an *M-L* mutator, or an *M-C* mutator, connecting an appropriate non-linear resistor, capacitor or inductor across terminal 2. This allowed the realization of a memristor with any prescribed φ-q curve [*6*].

Ten years later in 1986, Robert Johnson and Stanford Ovshinsky receive a patent [*20*] describing the manufacture of a 2-terminal reconfigurable resistance switching array based on phase changing materials (amorphous silicon alloy material or a chalcogenide), using crossbar architecture (a configuration where the top electrode is typically perpendicular to the bottom electrode and “crosses” it at the point of intersection) like that used two decades later in the first physical memristors produced by Stan Williams’ group at HP [*14*, *21*]. It is notable that the device described in the 1986 patent is not a memristor as its behaviour is distinct from that of memristive devices, although there are similarities between the basic elements used in both devices [*22*].

In 1990, an article entitled “Solid-state thin-film memistor for electronic neural networks” was published in the Journal of Applied Physics [*23*]. This memistor is a solid-state device, but as it is a three-terminal device it does not meet the requirements that would make it a memristor as described by Chua’s 1971 paper.

Since 1990, many new patents were released and many new articles published describing devices that behaved in a way that was like memristors; however, these publications did not specifically mention memristors, and no direct links between these devices and memristors were drawn [*22*]. In 2008, however, Stan Williams and his team at HP Labs published an article in Nature identifying a link between the two-terminal resistance switching behaviour of devices made with nanoscale thin films, and Chua's memristor [*21*]. The devices HP Labs made were the first to be identified as memristors, although an article published by Chua in 2011 has redefined all 2-terminal non-volatile memory devices based on resistance switching effects as memristors [*24*, *25*], which includes within the new definition many older devices [*7*] and some newer concepts such as ReRAM (resistive random-access memory, non-volatile RAM that works by changing the resistance across a dielectric solid state material) and spin-transfer torque magnetic tunnel junctions (junctions formed using a fixed layer that does not move, and a free ferromagnetic layer that can be flipped by an applied spin-polarized current, separated by a thin insulating layer through which the current tunnels) [*25*, *26*].

1.2 Zinc Oxide

Zinc oxide (ZnO) is a semiconductor material that has gained a significant amount of interest in recent years. It has a high energy band gap of ~3.4 eV, with a large exciton binding energy of 60 meV at 300 K [*27*, *28*]. A cheap material to produce, it can be synthesized via a range of different procedures including vapour-phase

depositions and solution-phase processes (described below), creating a range of different nanoscale structures including 0-D structures (referring to a structure such as a nanoparticle, that is spatially confined such that no dimensions *x*, *y*, or *z*, exceed the nanoscale range of 100 nm [*29*, *30*]) , 1-D structures (such as nanowires and nanorods, in which only one dimension, corresponding to the structure's length, is not confined to the nanoscale range [*29*, *30*]), and 2-D structures (such as nanoscale thin films, in which two dimensions are not confined to the nanoscale range [*29*, *30*]) [*31*].

Typical deposition methods include both physical vapour deposition (PVD, which generally uses physical processes to evaporate the ZnO and then deposit this vapour onto the substrate as a solid, with no chemical change to the material [*32*]) and chemical vapour depositions (CVD, which generally involves producing a vapour from zinc powder, which then undergoes a chemical reaction with oxygen in the air to become ZnO which is then deposited [*32*]), as well as solution-phase processes, which typically involve either pyrolysis (thermal decomposition) of a solution-based ZnO precursor [*33*] (such as a zinc salt, including zinc acetate or zinc nitrate), or the spin-coating of a colloidal dispersion of ZnO nanoparticles, which then is heat-treated to compact the material and form a solid mass of the material, a process known as sintering [*33*].

ZnO is a material of particular scientific interest due to its applications in solar cells [*34–39*], thin film transistors [*34–36*, *40*, *41*], transparent conductive oxides [*42–46*], resistive switching memory devices (including memristors) [*47–50*], and many other

applications [*51*, *52*]. In solar cells, the properties of ZnO as an *n*-type inorganic semiconductor, as well as its rich defect chemistry (defects in this case referring to formations in the crystalline structure where an atom is missing from a position that ought to be filled, known as a vacancy, or where an atom is present where it would not normally appear, known as an interstitial defect [*53*]), allow it to act as an electron acceptor material in hybrid solar cell configuration that feature an organic semiconductor as an electron donor, or as an electron collector and hole blocking material if used as a buffer layer or as an electrode material in an organic solar cell configuration [*54*].

High electron mobility (the ratio of the velocity of an electron moving through a metal or semiconductor to the applied electric field driving the electron's motion [*55*]) alongside low deposition temperatures and visible transparency as a thin film make ZnO attractive as a material for use in thin film transistors, where typically amorphous silicon has previously been used; amorphous silicon has a lower electron mobility than ZnO, and high mobility is necessary for achieving high frame rates in high-resolution LCD (liquid crystal display) and OLED (organic light-emitting diode) displays [*56*].

ZnO requires heavy doping with group III elements (such as aluminium (Al), gallium (Ga) and indium (In)) if it is to be used as a transparent conductive oxide, but its low cost and simple deposition methods, combined with its non-toxicity, make it a promising alternative to the indium oxide (In_2O_3) films that have seen practical use in the past [*57*].

Many of the aforementioned properties of ZnO, in particular its rich defect chemistry, low cost, simple fabrication, and high electron mobility, lend themselves to its application as a material for resistive memory devices. The mechanisms by which ZnO operates as a resistive memory material will be discussed in chapter 2.

Crystalline ZnO has a wurtzite (B4) crystal structure that has a hexagonal unit cell with two lattice parameters *a* and *c*, as shown in figure 2. Each anion is surrounded by four cations forming a tetrahedral structure that exhibits sp3 covalent bonding [*52*]. This tetrahedral configuration of ZnO gives rise to a noncentrosymmetric structure, having no inversion centre. Figure 1.3, below, shows the tetrahedral wurtzite structure of ZnO.

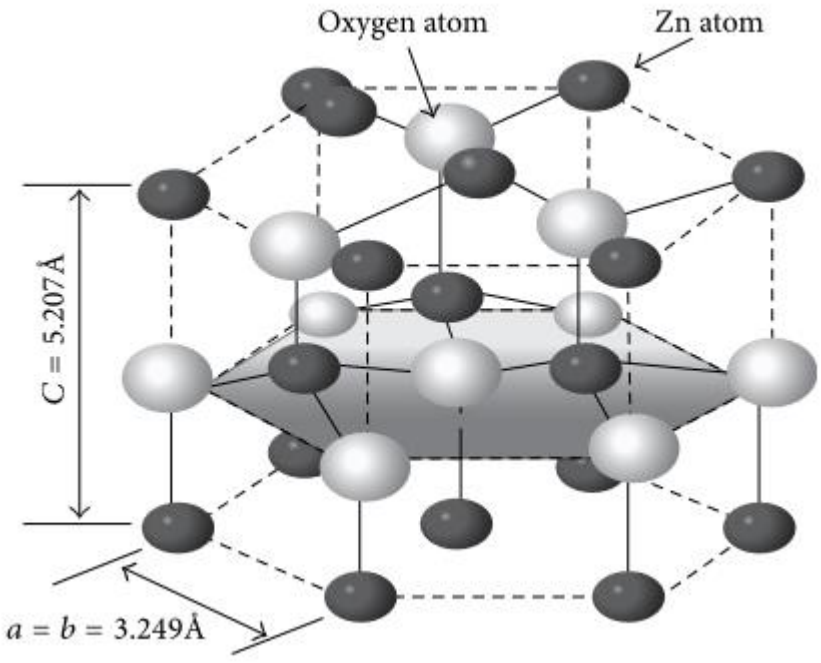

Fig. 1.3: Tetrahedral Wurtzite Structure of ZnO [*52*].

Zinc oxide can also exist in the cubic “zincblende” structure. This structure is less stable at ambient conditions than the wurtzite structure. This is due to the lower ionicity of the zincblende structure compared with the high ionicity of the wurtzite structure, which resides exactly at the borderline between the covalent and the ionic materials [*58*].

This project focuses on the use of a cost-effective and simple microwave-assisted solution-processing method for synthesizing ZnO nanorods [*59*], using the ZnO material as a semi-conductive layer between two electrodes. Other forms of ZnO (nanoparticles and thin films) are investigated but not in significant detail.

1.3 Organic/Inorganic Hybrid Memristors

The use of “hybrid materials” (those containing both organic and inorganic components, often referred to in literature as “composite materials” as well as hybrid materials [*60*, *61*]) is an area in the memristor field that is much less-studied than other areas, including either organic or inorganic memristors in their own rights. These materials combine the electronic properties of semiconductors with the solution-processing advantages of organic materials, allowing for devices to be produced at lower temperatures on lightweight and flexible substrates, as well as allowing production of low cost memristor arrays covering large substrate areas [*59*].

Using a hybrid material configuration or composite material has several advantages alongside those listed above. The use of composite materials may result in the

formation of Schottky barriers (described in detail in chapter 2 as an energy barrier typically at the interface between a metal and a dielectric material, formed as a result of the difference between the work function of the metal and the electron affinity of the dielectric) that act as a threshold element [*60*]. In addition, certain configurations of hybrid/composite materials (in particular, poly(methyl methacrylate) (PMMA) deposited onto the surface of a ZnO nanorod layer) may also smooth out the interface region, masking local effects at the electrodes including surface defects and surface roughness, while also impeding the formation of small filaments caused by the migration of the surface atoms of the electrodes [*59*]. Using different polymer layers can also allow for further applications; for example, use of an optically active polymer can allow switching behaviour that is controllable by polarization of light [*62*]. This is advantageous since switching based on light enables higher bandwidth signalling and faster transmission speeds.

The use of hybrid/composite materials does have its disadvantages, however. Using multiple materials for a hybrid layer can increase the cost to produce the memristor units, as well as increasing the complexity of the device in terms of fabrication procedure. In addition, transport mechanisms for such configurations are not well understood; transport mechanisms for oxide-based memristors often involve, or rely upon, intrinsic defects within the switching material (for example, oxygen vacancies or zinc interstitials in ZnO [*63–65*]), Schottky barriers [*66*] or conductive filament formation [*67*], whilst mechanisms for polymer-based memories are difficult to identify [*68*]. As such, combining different materials can result in messy transfer

physics, as multiple switching mechanisms compete for dominance. Many of the different conduction mechanisms are discussed in chapter 2.

1.4 Research Objectives and Thesis Outline

We have developed a novel memristor device, using zinc oxide (ZnO) as a semi-conductive layer between two electrodes arranged vertically on a glass substrate (with or without the addition of an organic polymer layer of poly(methyl methacrylate) (PMMA) deposited between the ZnO layer and the top electrode), that can be made quickly and at low cost using simple and inexpensive solution processing techniques. Through analysing the behaviour of the memristor devices, we have developed an understanding of some of the mechanisms that underpin the switching behaviour of these devices (specifically, we compare the contributions of Schottky emission, Poole-Frenkel emission, and space charge limited conduction mechanisms, through analysis of the nonlinear regions of the I-V sweep data), enabling us to improve device properties through manipulation of these mechanisms and the physical properties of the device that determine the dominant mechanism.

Chapter 2 discusses the properties of memristors. Leon Chua's memristor theory will be discussed in more detail than in the historical perspective given in this chapter. In addition, Hewlett-Packard's first physical memristor will be discussed. Chapter 2 will also review the transport mechanisms that are typically observed in memristors, particularly those mechanisms related to devices made with zinc oxide.

Chapter 3 reviews some of the most commonly used methods of producing/depositing ZnO nanorods. An explanation of a typical procedure for each method is given, along with the advantages and disadvantages of each method. The methods discussed are physical vapour deposition (PVD), chemical vapour deposition (CVD), electrochemical deposition, and chemical bath deposition.

Chapter 4 details the experimental methods used in this project. The chapter begins with the methods for device fabrication: electrode deposition via thermal evaporation, which applies for both the top and bottom electrodes (in the cases where the bottom electrode is a metal); the nanorod growth procedure, including both the preparation of the seed layer and the microwave-assisted growth of the nanorods from zinc salt solutions; and also the deposition of an insulating layer of poly(methyl methacrylate) (PMMA). Chapter 4 also explains the investigation techniques used to test the memristor devices: scanning electron microscopy (SEM) to investigate nanorod structures; atomic force microscopy (AFM) to investigate the smaller nanoparticles that make up the seed layer; and x-ray diffraction spectroscopy (XRD) for phase identification of the crystalline structures.

Chapter 5 presents the results of a study of the growth of nanorods, including AFM images of the seed layer under a variety of conditions, and SEM images and XRD of nanorods grown using the methods outlined in the previous chapter. The data shows that a uniform seed layer, annealed at temperatures of ~350°C, is required for uniform, well-aligned nanorod growth, and that a slow temperature ramp at low microwave power produces a nanorod layer with fewer undesirable crystallite

formations/depositions on the nanorod layer surface. The SEM and XRD data shows that nanorods are vertically aligned and have the wurtzite blende crystal structure.

Chapter 6 presents the results of electrical measurements on the completed memristor devices. This includes I-V sweep data for memristors constructed in a variety of different configurations. Endurance and retention measurements are included for key configurations as well. The data shows that the choice of electrodes as well as the configuration of materials has a significant effect on the behaviour of the memristor devices produced by our methods, with aluminium (Al) top electrodes and gold (Au) bottom electrodes appearing to have the largest on/off ratios and the most clearly distinct resistance states. The data also shows that, when the device is tested in a nitrogen environment with low ambient oxygen and low humidity, hysteresis does not occur.

Chapter 7 investigates the electrical behaviour of our device configurations to identify the conduction mechanisms, using plots for Schottky emission ($ln\ J/T^2$ vs. $E^{1/2}$), Poole-Frenkel emission ($ln\ {}^{J}/_{E}$ vs. $E^{1/2}$) and space charge limited conduction (I vs. V plotted on logarithmic scale axes). We see that the inclusion of a PMMA layer affects the transport mechanisms in the devices, and typically limits electron transport at the interface between the PMMA and the electrode. Au/ZnO/Au and Au/ZnO/PMMA/Au configurations typically exhibit SCLC behaviour and Poole-Frenkel emission behaviour, as does the ITO/ZnO/PMMA/Al configuration; the Au/ZnO/Al configuration and ITO/ZnO/Al configuration appear to exhibit Schottky emission behaviour, although the addition of PMMA prevents this. All devices exhibit linear

Ohmic conduction at low voltage magnitudes (i.e. prior to switching from one resistance state to the other).

Chapter 8 summarizes the findings from this project and highlights areas that require further study for future work. In particular, further study of the transport mechanisms is needed, at a range of different temperatures, to confirm that the temperature-dependent mechanisms of Schottky emission and Poole-Frenkel emission are indeed occurring as our results thus far indicate, as well as to help determine the ideal operating temperatures of our devices. Further study into the effects of the defect chemistry in ZnO on the hysteresis behaviour of the devices is also needed, and the endurance and retention characteristics of devices needs to be optimised. Conclusions are also drawn from the findings presented in this chapter.

Chapter 2

Properties of Memristors

This chapter discusses the background and theory behind memristors. First, the conception of the theoretical memristor device, as proposed by Leon Chua, will be reviewed, highlighting key theoretical concepts. The development of Hewlett-Packard's first memristor based on titanium dioxide (TiO_2) will also be discussed, with explanation as to what was seen to occur during the memristor's switching operation.

From here, the mechanisms that underpin the resistance-switching behaviour will be discussed in more detail. Specifically, five different mechanisms will be examined: the first of these is electrochemical metallization (ECM), a filamentary switching mechanism that occurs between the two electrodes through an insulating (or semi-conductive) thin film; the other mechanisms are interface mechanisms, occurring at the interface between one of the electrodes and the insulating (or semi-conductive) layer, including Ohmic conduction, Schottky emission, the Poole-Frenkel effect, and Space Charge Limited Conduction (SCLC). Each of these mechanisms are discussed in terms of the role they play in the overall switching effects observed in memristors.

2.1 Chua's Memristor Theory

In electronic circuit theory, there are three fundamental circuit elements – two-terminal elements that are defined by the relationships between the fundamental circuit variables of voltage *V*, current *I*, charge *q*, and flux-linkage *φ*, which is the circuit variable that links the magnetic flux, *Φ*, passing through a coil with the number of turns in the coil. These basic circuit elements are the resistor (defined by the relationship between *V* and *I*), the capacitor (defined by the relationship between *q* and *V*), and the inductor (defined by the relationship between *φ* and *I*). In total, there are six relationships [*6*, *24*] that link the four fundamental circuit variables: three of these ($R = \frac{V}{I}$, $L = \frac{\varphi}{I}$, and $C = \frac{q}{V}$) are the relationships defining the basic circuit elements as mentioned above; two others define *φ* and *q* as the time-integrated functions of *I* and *V* respectively:

$$q(t) \equiv \int_{-\infty}^{t} I(\tau)d\tau \qquad (1)$$

$$\varphi(t) \equiv \int_{-\infty}^{t} V(\tau)d\tau \qquad (2)$$

where τ is a small increment of time compared with the total time *t*. However, prior to 1970, the sixth relationship – that between *φ* and *q* – had not been defined.

In his 1970 paper, Chua proposed a fourth basic circuit element, named a "memristor" (because it "behaves somewhat like a nonlinear resistor with memory" [*6*]), that is defined by the relationship between *φ* and *q*.

From Chua's paper, a memristor is characterized by a relation of the type $g(\varphi, q) = 0$. A memristor can be said to be charge-controlled if this relation can be expressed as a single-valued function of the charge q, and can be said to be flux-controlled if the relation can be expressed as a single-valued function of the flux-linkage φ [*6*]. These relations allow the voltage across a charge-controlled memristor to be calculated using the formula:

$$V(t) = M\big(q(t)\big)I(t) \tag{3}$$

where

$$M(q) \equiv \frac{d\varphi(q)}{dq} \tag{4}$$

As can be seen from equation 4, above, *M(q)* ("incremental memristance", as described by Chua) links together the charge and the flux linkage, the missing relationship that Chua identified from his considerations of the fundamental circuit elements. Equation 3 can be rearranged to show that memristance has the units of resistance.

Also, from the above relations we can see that in the case of a flux-controlled memristor, the current can be found by

$$I(t) = W\big(\varphi(t)\big)V(t) \tag{5}$$

where

$$W(\varphi) \equiv \frac{dq(\varphi)}{d\varphi} \tag{6}$$

W(φ), having units of conductance, is described as the “incremental memductance” [*6*].

A memristor behaves like an ordinary resistor at any given instant of time t_0, but the resistance, *R*, or conductance, *G*, of the device depends on the complete past history of the memristor current or voltage respectively; this results from the fact that memristance is defined by the relationship between *φ* and *q*, which are time-integrated functions of *V* and *I*. Once the voltage or current has been specified, the memristor behaves like a linear time-varying resistor. Chua also identifies that, in the special case where the memristor *φ*-*q* curve is a straight line, so too is the I-V curve as the memristor is reduced to a linear time-invariant resistor, where *M(q)* = *R* and *W(φ)* = *G* [*6*].

For a physical memristor device to be realized that did not require its own internal power supply, it would need to meet the following fundamental criteria:

- The “Passivity Criterion” states that: “A memristor characterized by a differentiable charge-controlled *φ*-*q* curve is passive if, and only if, its incremental memristance *M(q)* is non-negative; i.e. *M(q)* ≥ 0” [*6*]. As a memristor behaves like a linear resistor at any instant of time, this criterion can be viewed as analogous to the behaviour of an ordinary resistor, in that the resistance of an ordinary resistor cannot be negative, as a result of Ohm’s Law. This criterion therefore demonstrates that only memristors characterized

by a monotonically increasing *φ-q* curve can exist as a single device form without its own internal power supply. It is also noted that passive memristor devices do not seem to violate any of the known laws of Physics [*6*].

- The "Closure Theorem" [*69*] states that: "A one-port containing only memristors is equivalent to a memristor" [*6*]. This criterion essentially tells us that, in the case of a two-terminal circuit network made up of only memristors (a single memristor also applies, as it is a two-terminal device), the network would also be equivalent to a single memristor. This is similar to creating a cell of resistors (either in series or in parallel), where the output of the cell would be either the sum of the resistances (in series, i.e. $R_t = R_1 + R_2 + \cdots + R_n$) or the reciprocal of the sum of their reciprocals (in parallel, i.e. $\frac{1}{R_t} = \frac{1}{R_1} + \frac{1}{R_2} + \cdots + \frac{1}{R_n}$), and the cell would behave as a single resistor with that single output resistance.

- The "Existence and Uniqueness Theorem" [*69*] states that: "Any network containing only memristors with positive incremental memristances has one, and only one, solution" [*6*]. Considered alongside the closure theorem above, reinforces the statement that a network of passive memristors is equal to a single, unique memristor.

Chua regarded the fundamental identifier of the memristor to be a "pinched hysteresis" in the current-voltage characteristics of the device [*25*]. Figure 2.1, below, shows a typical example of a pinched hysteresis effect. The loops that characterize

this hysteresis effect are demonstrative of “switching” behaviour between high and low resistance; high resistance can be treated as a “1” in binary logic, while a low resistance can be treated as a “0”. In general, the mechanism that causes this “resistance switching” depends on the direction of the current flowing through it. The electrical resistance of the memristor device will increase if the current flows one way, while sending the current the other way will decrease the resistance [*70*, *71*].

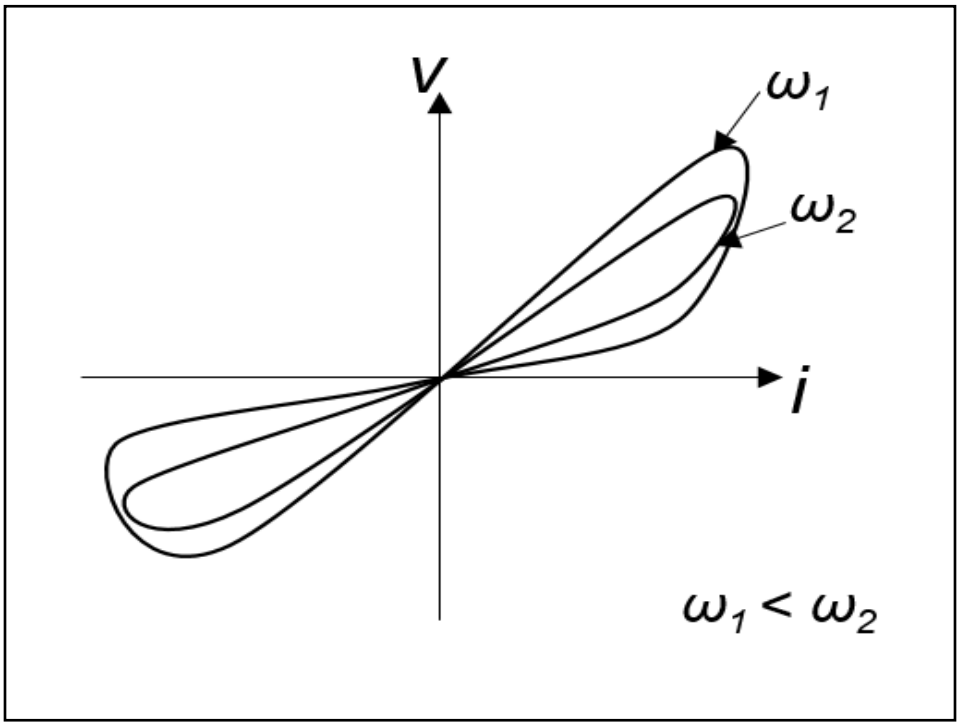

Fig. 2.1: An example of a pinched hysteresis loop showing the loop shrinking with increase in frequency, ω (with ω_1 being a lower frequency than ω_2). Adapted from [*70*].

A particularly important feature of the memristor, however, is that when the current is no longer flowing through the memristor, it will retain its previous state of high or low resistance and will only change state when the current passes through again,

once more depending on the direction of the current. This makes the memristor device a non-volatile memory: a device that retains its state even once power is removed [*72*].

Chua describes the pinched hysteresis loop as being confined to the first and third quadrants of the voltage vs. current plane “whose contour shape in general changes with both the amplitude and frequency of any ‘sine-wave-like’ input voltage source, or current source” [*25*]. Stan Williams of HP explains that the pinched hysteresis effect “looks like a diagonal infinity symbol with the centre at the zero axis, when plotted on a graph of current against voltage” [*73*]. This indicates a change in resistance from high to low, and vice-versa.

Figure 2.1 also shows that the pinched hysteresis loop “shrinks” as the excitation frequency increases [*70*]. As the frequency approaches infinity, the hysteresis loop becomes a straight line and the device behaves as an ordinary resistor. This is another signature feature of memristor devices, and is an important feature that makes memristors ideal for use in various applications, including in analogue circuits as components in sinusoidal oscillators (where some or all of the resistors typically used in the sinusoidal oscillators are replaced with memristors [*74*]), in signal processing applications (including control systems, communication systems, and pattern recognition systems [*75*]), and neuromorphic circuits (where the memristor performs as an electronic synapse with negligible power thrust [*74*, *76*, *77*]).

2.2 Physical Memristor Devices

In November 2008, Hewlett Packard's R. Stanley Williams reported an experimental solid-state version of the "memristor" based on the behaviour of nanoscale thin films of titanium dioxide, TiO_2 [*21*, *73*]. This device was fabricated as an attempt to address the encroaching end of Moore's Law; an observation that explained the shrinking of transistors and "their commensurate steady doubling on a chip about every two years" [*73*]. Eventually, this observation predicts a limit to the minimum size a transistor can be fabricated, as a result of excess heating and a greater probability of electron tunnelling effects in very small device architectures.

Williams explains in an article explaining the discovery of this memristor device [*73*] that "whether this scaling paradigm lasts for 5 more years or 15, it will eventually come to an end", and that there is now a pressing need to find a way to increase the capability of devices as well as/instead of simply decreasing their size.

Now that a physical memristor device has been realised, its potential as an answer to this scaling problem has become very interesting to the scientific community. Figure 2.2 shows an STM image of the configuration for HP's device.

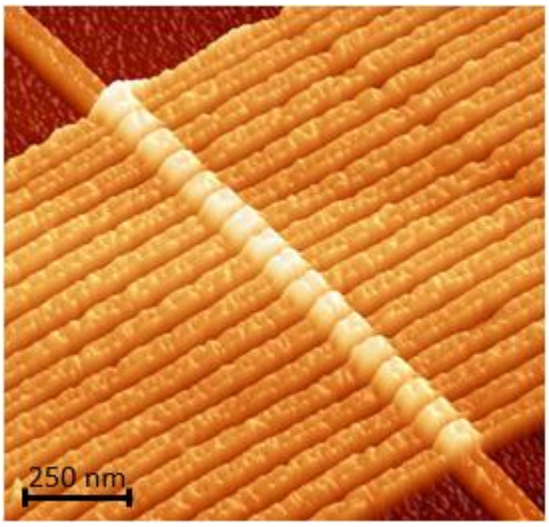

Fig. 2.2: An STM image showing 17 separate memristor devices made of titanium dioxide, as produced by R. Stanley Williams and his team at HP [*73*]. Each wire is about 50 nm wide.

Williams' device, which he describes as being "like a tiny sandwich", was designed initially as follows: a bottom wire of platinum wire was oxidized on one surface only, to create an extremely thin layer of highly-conductive platinum dioxide. On top of this is a monolayer of "specially designed switching molecules", arranged in a dense, single-molecule-thick film. This is covered by a 2 – 3 nm layer of titanium metal, on top of which is another platinum electrode [*73*]. The switching was meant to occur within the layer of special switching molecules, however Williams and his team noticed that even with the switching molecules replaced with soap, in which there is nothing that would be expected to cause switching, a switching effect would still occur. In fact, on closer observation, Williams found that the platinum dioxide layer had donated its oxygen molecules to the titanium, forming pure platinum and titanium dioxide respectively. Also, the titanium dioxide had split into two distinct layers – a layer of pure TiO_2, and a layer closer to the top platinum electrode of TiO_{2-x}, where

x approximated to about 0.5. In the latter case, the titanium oxide was missing some of the oxygen, approximately 2 – 3% [*21*, *73*]. It was found that these two layers were responsible for the switching behaviour; the TiO_2 layer acting as an electrical insulator (in fact, as a semiconductor) and the TiO_{2-x} layer being conductive due to its oxygen vacancies acting as holes (positively charged vacancies that can be occupied by electrons). It was found that applying a positive voltage across the device allowed these holes to travel through to the TiO_2 layer, making the device conductive and lowering the resistance (turning the device "on"); conversely, applying a negative voltage caused the holes to migrate back out of the TiO_2 layer, increasing this layer's thickness and thereby restoring its insulating behaviour, increasing the resistance (turning the device "off") [*21*, *73*]. He explains the discovery that memristance arises in a semiconductor when both electrons and charged dopants are forced to move simultaneously by applying a voltage to the system. It was realised that the layer of special switching molecules was irrelevant to the device, and as such, for the final working sample, this layer was removed entirely. The result was a device in which the oxygen vacancies remained in place once the voltage was no longer applied and would only change states (thereby changing the resistance of the device) when a voltage was applied. This is the memristor – a device that can remember its previous state even without power [*73*].

Chua and Williams both realised that memristor devices have great potential for a wide range of applications outside of that of a simple memory device. Williams observed that the memristor behaved similarly to synapses (connections between neurons) in the human brain [*73*], as they consume very little power and are able to

remember their past dynamical history, as well as being able to store data in a continuous set of states [*77*]. As such, it is believed that memristors could potentially be used to create circuits and systems that mimic certain parts of the brain, using memristors as synaptic connections and other fundamental circuit components to represent the neurons and axons. This could lead to “intelligent” computer systems and sensor arrays that might, for example, be of interest to the military, or the police (Williams gives the example of computer systems with advanced face-recognition technology that could recognise a person’s face in a crowd even if it has changed significantly since its last observation) [*73*].

HP had very ambitious plans for the new technology, as a universal memory that would revolutionize the world of computing. Among their most ambitious plans was to develop a new computer architecture designed around memristors and photonics, known as “The Machine” [*78*]. The aim was to create a new computer architecture that did away with conventional forms of memory and replaced them with memristors as a non-volatile and universal memory, which, combined with silicon-based photonics, would allow for vast quantities of data to be managed at high speeds [*79*]. However, due to uncertainty over when HP would be able to produce memristors in commercial quantities, the Machine was re-designed to use conventional RAM, with a possibility of introducing memristors at a later date [*80*].

2.3 Transport Mechanisms of Memristors

The term “resistive switching” refers to a phenomenon (or rather, a category of phenomena) that results in the change of “state” of the resistance of the memristor or memristive system; the “state” being either one of high resistance (which, as $V = IR$, means that the current must be lower for the same applied voltage, and is thus referred to as the “off” state, or R_{off}) or of low resistance (which is known as the “on” state, or R_{on}). The “switching” can be a clear and abrupt “fuse-antifuse” switch (in which a dramatic change in resistance is observed in the *I-V* characteristics of the device; this is typically observed in filamentary switching, as described later in this chapter) or a more continuous change in resistance (referred to as “homogeneous switching” [*50*]); in many papers this continuous behaviour is still referred to as “switching”, as in the HP paper described above [*73*]. As stated in section 2.1, these two resistance states can be used in binary coding, representing a “1” for the low resistance state (LRS) or a “0” for the high resistance state (HRS). The processes that cause the device to switch from one state to the other are known as “SET” (for the process that switches from HRS to LRS) and “RESET” (for the process that returns the device from LRS to HRS). As will be explained later in this chapter, the “RESET” does not necessarily return the device to its initial state, as the formation of conductive pathways throughout the switching material may change the behaviour of the device after the initial “SET” process.

Resistive switching memory devices can be classified as either “unipolar” (referring to switching for which both the “SET” and “RESET” processes occur in the same

voltage polarity – either positive or negative – but with different magnitudes of the applied voltage) or “bipolar” (referring to switching for which the “SET” and “RESET” processes depend on both the magnitude and the polarity of the applied voltage) [*81*].

Figure 2.3 shows typical I-V sweep behaviour of both unipolar and bipolar switching.

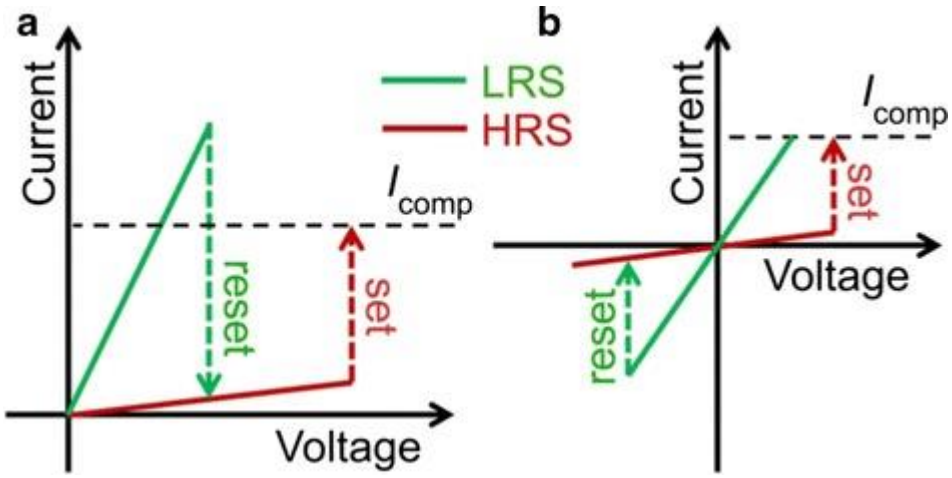

Fig. 2.3: The I-V characteristics of a unipolar (a) and bipolar (b) memristor [*81*]. I_{comp} is the compliance current, a limit imposed by the voltage source to prevent the destruction of the device.

The electronic transport mechanisms occurring within memristors and memristive devices are of key interest to the scientific community at large; while there has been much research carried out into the transport mechanisms, it is still unclear which mechanisms are most dominant and under which circumstances, although it is now widely accepted that different mechanisms exist, and in some devices multiple mechanisms may be responsible for the switching, to different extents [*70*].

This chapter aims to discuss some of the known transport mechanisms, with particular focus on the use of zinc oxide as a switching material. It should be noted that this chapter discusses transport mechanisms that are known to occur, however not all of these mechanisms necessarily apply to the devices that we have developed.

2.3.1 Electrochemical Metallization (ECM)

Electrochemical metallization (ECM) is a process by which conductive filaments are formed or dissolved between the two terminals of the memory cell. The structures of ECM cells are usually asymmetric, with one electrochemically active electrode (e.g. copper [*82*, *83*], silver [*84*, *85*], aluminium [*86*]), an inorganic thin film that functions as an electrolyte (e.g. inorganic oxides [*83–85*] including ZnO [*87*]), and an inactive electrode (e.g. gold [*83*, *85*], platinum [*82*, *84*], palladium [*83*]). The SET process for an ECM cell/device (a switch from HRS to LRS) is described as a three-step process of dissolution, drift and reduction of the metal atoms from the active electrode [*87*, *88*]. The atoms of the active electrode dissolve into the insulating film by means of the application of a high voltage that turns them into a charged species. Once charged, these ions are then dragged through the insulator bulk by the applied electric field, drifting towards the opposite electrode. Upon reaching the inactive electrode, the ions are reduced and begin nucleating, leading to the formation of a conductive metallic filament connecting the two electrode contacts. The RESET process can be achieved by reversing the polarity of the voltage, leading to partial oxidation of the metallic ions back into the contact, or by rupturing the metallic filament through the Joule effect, which randomly spreads the metal particles [*89*].

Figure 2.4, below, shows a schematic of the switching mechanism for electrochemical metallization in metal-insulator-metal (MIM) cells. As the image suggests, the first switch usually appears slightly different from all subsequent switching due to the initial forming stage. Devices then switch between the “SET” and “RESET” states; they do not return to the initial “pristine” state.

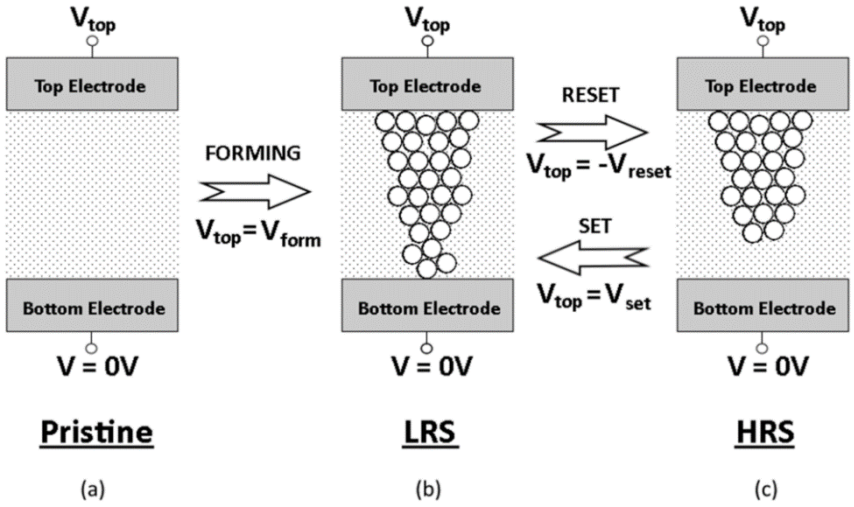

Fig. 2.4: A schematic showing the formation and destruction of a conductive filament between the bottom and top electrodes of an MIM cell [*90*].

For this process to occur and to observe rapid switching between the HRS and LRS states, the electrolyte layer must typically have a thickness of only a few tens of nanometres; diffusion and formation of metallic filaments through films of greater thickness than this would be unlikely, and would be kinetically hindered by the insulating film [*87*, *89*]. Unexpectedly, however, with nanorods – which can typically have lengths in the order of microns – memristive behaviour can still be observed. In this case, investigations have revealed that the active electrode atoms move on

the surface of the nanorods rather than through their bulk. This allows for faster percolation and gives rise to current flow through formation of a surface conductive channel. Using an active Cu electrode with ZnO nanowires, it has been shown [*87*] that the switching effect relies upon ZnO surface doping effects of single Cu adatoms (an atom that adsorbs onto a crystal surface), rather than on the formation of continuous metallic filaments as had been expected from the results of the thin film studies.

2.3.2 Interface-Type Switching

Resistive switching can also occur near the interface between the electrode and the functional layers. Several possible mechanisms have been proposed for such switching behaviour, including electrochemical migration of oxygen vacancies [*91*, *92*], trapping of charge carriers [*93*], and a Mott transition induced by carriers doped at the interface between the functional layer and the electrode [*94–96*].

Unlike filamentary transport mechanisms, interface-type switching is typically homogeneous [*97*]; while ECM filaments form a single conductive path that allows for the resistive switching to take place, interface-type switching occurs throughout the entire area of the interface between the electrode and the functional layer(s). As a result of this feature, interface-type switching typically exhibits electrode-area-dependent resistances [*98*] with switching cells showing clear scaling of device resistances with electrode area.

Many factors can contribute to interface-type switching mechanisms. Schottky emission, the Poole-Frenkel effect, and Space Charge Limited Conduction (SCLC) are three of the most deeply-researched and studied mechanisms, and it is known that in many cases a combination of any of these mechanisms (or all three) may be occurring in a single memristor cell [*97*]. These three mechanisms are significant enough to warrant their own distinct discussion, and so will be covered in the following subchapters.

2.3.3 Fowler-Nordheim Tunnelling

Fowler-Nordheim tunnelling is a quantum-mechanical process whereby electrons can pass through potential energy barriers (tunnelling) when a high enough electric field is present. This occurs because the wave function of electrons decays into the potential energy barrier instead of just stopping at the barrier, and so the probability of electrons existing on the other side of the potential barrier is not zero. This occurs when the barrier is sufficiently thin (<100 Å [*99*]), and so is not typically expected to occur in nanorod layers that are as thick as the ones produced by our methods (1 Å = 0.1 nm, and our nanorod films are typically > 400 nm in thickness). However, the high electric field at the tips of the nanorods may be enough to initiate Fowler-Nordheim tunnelling.

The expression for Fowler-Nordheim tunnelling current density is as follows:

$$J = \frac{q^3 E^2}{8\pi h q \varphi_B} exp\left[\frac{-8\pi(2qm_T^*)^{1/2}}{3hE}\varphi_B^{3/2}\right] \quad (8)$$

where *J* is the current density, *q* is the electronic charge, *E* is the electric field, φ_B is the barrier height, m_T^* is the tunnelling effective mass in the dielectric, and *h* is Planck's constant [*99*]. There is no dependence on temperature for Fowler-Nordheim tunnelling.

This expression shows that *J* is dependent on *E*. Taking the natural logs of the above expression gives us the following:

$$ln\frac{J}{E^2} \propto \frac{1}{E} \tag{9}$$

A plot of $ln\frac{J}{E^2}$ vs. $\frac{1}{E}$ would be linear for Fowler-Nordheim tunnelling. Figure 2.5 shows the energy band diagram for Fowler-Nordheim tunnelling.

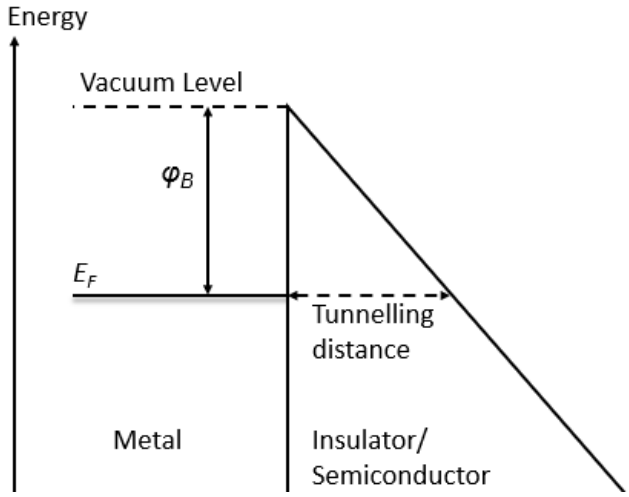

Fig. 2.5: An energy band diagram for Fowler-Nordheim tunnelling through a potential barrier formed between a metal and an insulator/semiconductor. Tunnelling occurs near the Fermi level. Adapted from [*100*].

2.3.4 Schottky Emission

Schottky emission is simply a form of thermionic emission (a thermally induced flow of charge carriers, particularly electrons, over a potential energy boundary, represented in this case by the difference in the work function of two materials) that is enhanced by the application of an electric field. For this reason, it is also known as “field-enhanced thermionic emission” [*101*].

Schottky emission is highly dependent on temperature. For very thin films (around 10 nm thick) at room temperature and pressure, Schottky emission generates currents of similar magnitude to those produced by Fowler-Nordheim tunnelling (field emission) [*102*]. Fowler-Nordheim tunnelling is not dependent on temperature, and generally contributes most heavily in regimes of much higher electric field than would be required for Schottky emission. As a result, Schottky emission is favoured over Fowler-Nordheim tunnelling by films with greater thickness, or materials with high work functions [*102*].

Schottky emission can be expressed mathematically by the following equation [*99*]:

$$J = A^{*}T^{2}exp\left[\frac{-q\left(\varphi_B-\sqrt{qE/4\pi\varepsilon_r\varepsilon_0}\right)}{kT}\right] \qquad (10)$$

where J is the current density, T is the absolute temperature, q is the electronic charge, φ_B is the Schottky barrier height, E is the electric field across the dielectric, k is Boltzmann’s constant, ε_0 is the permittivity of free space, and ε_r is the optical

dielectric constant. A^* is the effective Richardson constant for thermionic emission (named for Owen Willams Richardson, a British Physicist who won the Nobel Prize in Physics in 1928 for his work on thermionic emission), and is given by the equation:

$$A^* = \frac{4\pi q k^2 m^*}{h^3} = \frac{120 m^*}{m_0} \quad (11)$$

where m_0 is the free electron mass, m^* is the effective electron mass in the dielectric, and h is Planck's constant [*99*].

From these equations, it can be seen that current density attributed to Schottky emission is dependent on the electric field (E) and on temperature (T). Taking the natural log of equation 10, an equation of the form y = mx + c can be obtained [*103*]:

$$\ln {}^{J}/_{T^2} = \left[\frac{q\left(\sqrt{q/4\pi\varepsilon_r\varepsilon_0}\right)}{kT}\right]\sqrt{E} - \frac{q\varphi_B}{kT} + lnA^* \quad (12)$$

This can be expressed simply as:

$$\ln {}^{J}/_{T^2} \propto \sqrt{E} \quad (13)$$

As J and E are analogous to current and voltage (in that J is the current density, i.e. the current per unit cross-sectional area of a material, such that $J = {}^{I}/_{A}$, and voltage, or potential difference, is the difference in electrical charge between two points in an electric field, such that $E = -\frac{\Delta V}{d}$), and as the temperature is fixed, this expression may also be written as:

$$\ln I \propto \sqrt{V} \tag{14}$$

Schottky contacts to ZnO have been studied for over 50 years [*104*]. The basic theory of Schottky contact formation, developed by Schottky and Mott [*105*], predicts that, for an *n*-type semiconductor:

$$\varphi_B = \varphi_M - \chi_S \tag{15}$$

where φ_B is the Schottky barrier height of an "ideal" homogeneous contact, φ_M is the work function of the metal, and χ_S is the electron affinity of the semiconductor material [*106*].

Figure 2.6 shows an energy band diagram for a Schottky contact formed at the interface between a metal and an *n*-type semiconductor.

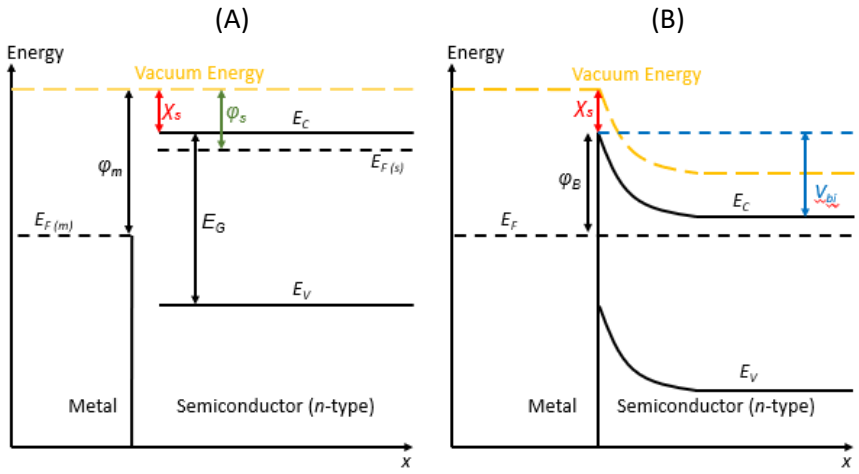

Fig. 2.6: Energy band diagrams of the Schottky emission conduction mechanism, for an *n*-type semiconductor Schottky barrier: (A) represents the band diagram for the metal and semiconductor before contact, while (B) is an ideal band gap of a contact formed between

the metal and the semiconductor. φ_B is the Schottky barrier height, which is dependent on the work function of the metal, φ_m, and the electron affinity of the semiconductor, χ_s. $E_{F\,(m)}$ is the Fermi level for the metal, while $E_{F\,(s)}$ is the Fermi level for the semiconductor. In (B), E_F is the Fermi level of both the metal and the semiconductor, which is aligned at equilibrium. The magnitude of the band bending, V_{bi}, is dependent on φ_m and the work function of the semiconductor, φ_s. E_G is the semiconductor band gap, and E_C and E_V are the conduction and valence bands respectively. Adapted from [*107*].

As figure 2.6 above shows, when the Schottky contact is formed between the metal and the *n*-type semiconductor, a transfer of charge occurs so that the Fermi levels of the two materials align, resulting in an equilibrium state (if the Fermi levels are not aligned, the electrons on one side of the junction will have more energy than those on the other side, resulting in the more energetic electrons flowing to the lower energy side) [*108*]. This results in bending of the energy bands (both the conduction band and valence band). This also occurs in *p*-type semiconductor contacts, although the Fermi level in the semiconductor is closer to the valence band in this case, as can be seen in figure 2.7 below.

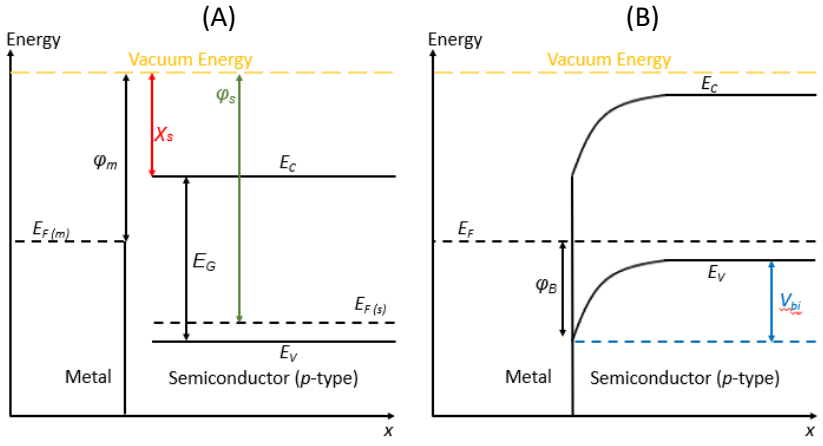

Fig. 2.7: Energy band diagrams of the Schottky emission conduction mechanism, for a *p*-type semiconductor Schottky barrier. Adapted from [*107*]. Notations are the same as in figure 2.5.

Comparing figures 2.6 and 2.7, it can be seen that V_{bi}, the magnitude of the band bending as a result of the alignment of the Fermi levels, is dependent on the work functions of the metal and the semiconductor.

For *n*-type semiconductors, $V_{bi} = \varphi_m - \varphi_s$, while for *p*-type semiconductors, $V_{bi} = \varphi_s - \varphi_m$. Unlike for *n*-type semiconductors, for *p*-type semiconductors the Schottky barrier height is given by

$$\varphi_B = E_G - (\varphi_M - \chi_S) \tag{16}$$

with notations as above [*108*].

Figure 2.8 shows the work functions (and the electron affinity for ZnO), and Schottky barrier height magnitudes of each material as a Schottky contact with ZnO, for a range of materials, the majority of which are relevant to this project specifically.

Metal work functions (Al, Ti, Zn, Cr, Ag, and Au) were taken from Kaye and Laby's *Tables of Physical and Chemical Constants* website [*109*]; the electron affinity for ZnO and the work function for ITO were taken from a paper by J. I. Sohn et al [*110*]. The approximated work function of PMMA was taken from *K. L. Mittal and H. R. Anderson Jr.'s Acid-Base Interactions: Relevance to Adhesion Science and Technology* [*111*].

Material	Work Function (eV) (electron affinity for ZnO)	Schottky Barrier Height (with ZnO) (eV)
Aluminium Al	4.28	N/A
Titanium Ti	4.33	0.03
Zinc Oxide ZnO	4.30	N/A
PMMA	~4	N/A
Zinc Zn	3.63	N/A
Indium Tin Oxide ITO	4.80	0.50
Chromium Cr	4.44	0.13
Silver Ag	4.26	N/A
Gold Au	5.10	0.80

Fig. 2.8: A table of the work functions of different materials, along with the electron affinity of zinc oxide, and the Schottky barrier heights for each material when used as a Schottky contact on ZnO. A Schottky contact is not formed between ZnO and materials with a work function below the electron affinity of ZnO.

2.3.5 The Poole-Frenkel Effect

The Poole-Frenkel effect is a bulk-controlled mechanism by which an insulator or a semiconductor can conduct an electric current as a result of the lowering of a trap barrier in the bulk of the insulator [*112*]. Traps, as mentioned in chapter 1, are locations within a solid in which the movement of electrons or holes is restricted [*15*]. Poole-Frenkel emission is experienced only if a trap is charged, such that the trap becomes uncharged when filled; a Coulombic barrier manifests due to the interaction between an electron and a positively-charged trap, or a hole and a negatively-charged trap. A donor or acceptor centre can manifest the Poole-Frenkel effect, but a neutral trap (a trap that is neutral when empty and charged when filled) will not manifest the Poole-Frenkel effect [*113*].

Figure 2.9 shows a band diagram demonstrating an electron being emitted from a positively-charged trap centre via Poole-Frenkel emission. When there is no applied electric field (referred to as “zero-field conditions”, or the “free-field state”), i.e. when $E = 0$, the barrier height for an electron (e^-) to escape from the positively-charged trap (t^+) is φ_t. When an electric field is applied, such that $E \neq 0$, the barrier is diminished by φ_{PF} compared with the free field state. Reversing the direction of the electric field increases the barrier in the same direction by roughly the same value [*114*]. The diagram shows an electron escaping from a positively-charged trap in the conduction band; however the same effect is observed for a hole escaping from a negatively-charged trap in the valence band.

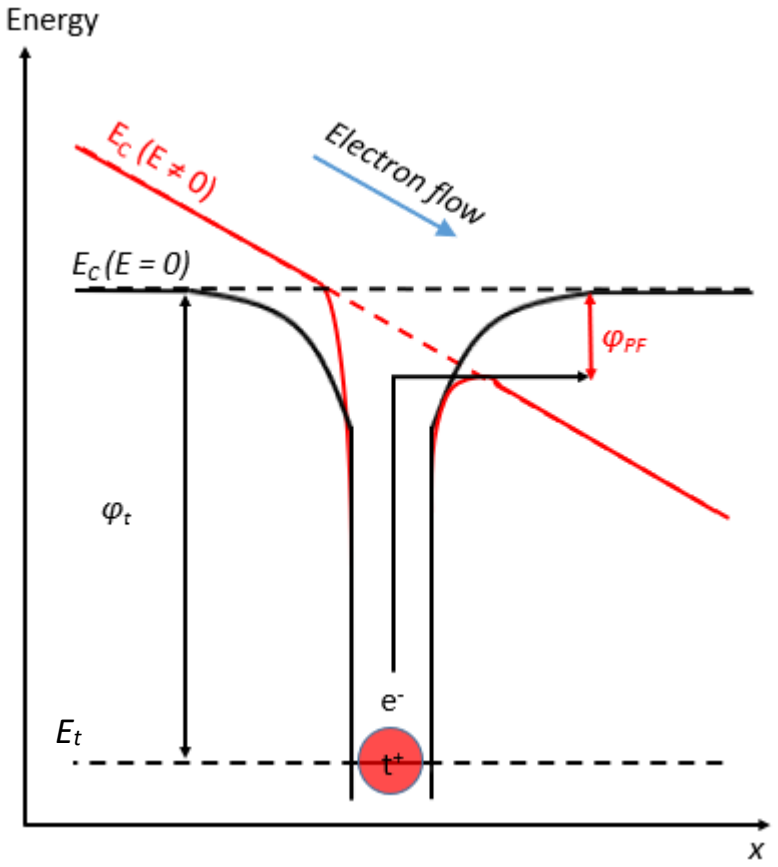

Fig. 2.9: A band diagram demonstrating Poole-Frenkel emission of an electron from a positively-charged trap centre in the conduction band. E_t is the trap energy level; other notations are as described above. Adapted from [*114*].

Poole-Frenkel emission is sometimes called an “internal Schottky emission”, as the mechanism is very similar to Schottky emission [*99*]. Thermal excitation may cause an electron to be emitted out of a trap and into the conduction band of the dielectric material. Application of an electric field across the dielectric film may reduce the Coulomb potential energy of the electron and thus increase the probability of the electron being emitted.

The current density due to the Poole-Frenkel effect for a Coulombic attraction potential between electrons and traps can be expressed as:

$$J = q\mu N_C E exp\left[\frac{-q\left(\varphi_t - \sqrt{qE/\pi\varepsilon_r\varepsilon_0}\right)}{kT}\right] \quad (17)$$

where μ is the electron drift mobility, N_C is the density of states in the conduction band, φ_t is the trap energy level, and the other notations are as defined above [*99*].

As with Schottky emission, it can be seen that the Poole-Frenkel effect is dependent on both the electric field (*E)* and on temperature (*T*). Poole-Frenkel emission is, therefore, often observed when a large electric field is present, or under high temperatures [*99*].

Taking the natural log of equation 15 gives the following [*103*]:

$$\ln\frac{J}{E} = \left[\frac{q\sqrt{q/\pi\varepsilon_r\varepsilon_0}}{kT}\right]\sqrt{E} - \frac{q\varphi_t}{kT} + \ln(qN_C\mu) \quad (18)$$

This can be expressed simply as:

$$\ln\frac{J}{E} \propto \sqrt{E} \quad (19)$$

Or, due to *J* being analogous to *I* and *E* being analogous to *V*:

$$\ln\frac{I}{V} \propto \sqrt{V} \quad (20)$$

Poole-Frenkel emission is also known to be dependent on the concentration of trap centres and donor centres (N_t and N_d, respectively), and this gives rise to two different forms of the Poole-Frenkel effect: if $N_t < N_d$, the conduction mechanism is referred to as the "normal Poole-Frenkel emission"; if $N_t \approx N_d$, the conduction mechanism is referred to as the "anomalous Poole-Frenkel effect", or the "modified Poole-Frenkel emission" [*99*]. This arises from the fact that, as proposed by Angle and Talley [*115*], the free electrons in Poole-Frenkel emission are emitted from the donor centres, and as a result, if there are other defect states (traps or acceptor states) in the dielectric film, the number of free electrons emitted from the donor states will be decreased [*99*]. As such, when comparing Poole-Frenkel plots (a plot of $\ln\frac{I}{V}$ vs. $\sqrt{V}$), the slope of an Anomalous Poole-Frenkel plot would be approximately half of the slope of a Normal Poole-Frenkel plot, and would equal the slope of a Schottky emission plot (a plot of $\ln I$ vs. $\sqrt{V}$) [*99*].

Schottky emission and Poole-Frenkel emission are similar in mechanism, however it is noted that Poole-Frenkel emission is a bulk-limited mechanism, while Schottky emission is an electrode-limited conduction mechanism. Electrode-limited mechanisms depend on the electrical properties at the contact between the electrode and the dielectric material; as such, they are dependent on parameters such as barrier height and the effective mass of the conduction carriers in dielectric films [*99*]. Bulk-limited mechanisms are dependent on the electrical properties of the dielectric material itself, and depend primarily on the trap energy levels in the film [*99*]. These differences allow differentiation between the Poole-Frenkel effect and Schottky emission (which may appear very similar, especially in the aforementioned

case of the anomalous Poole-Frenkel emission which exhibits a slope in the plot of $\ln\frac{I}{V}$ vs. $\sqrt{V}$ that is typically equal to that of Schottky emission) by observing the effect of different electrode materials. Figure 2.10 shows an energy band diagram of the Poole-Frenkel emission conduction mechanism.

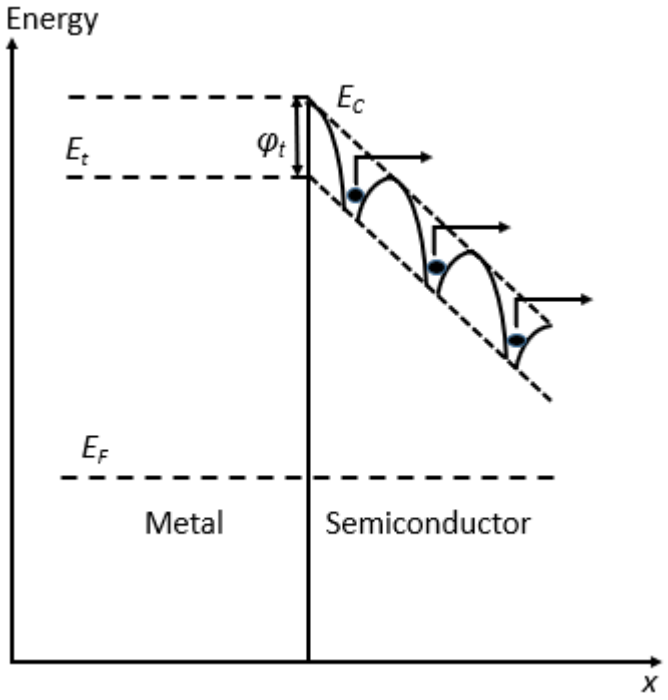

Fig. 2.10: An energy band diagram of the Poole-Frenkel emission conduction mechanism at a metal-semiconductor interface. When the number of traps is about equal to the number of donor centres, the behaviour is similar to that of Schottky emission. Adapted from [*99*] and [*114*].

As mentioned on page 45, Poole-Frenkel emission is dependent upon the electric field, *E*, and the temperature, *T*. With respect to figures 2.9 and 2.10, the barrier reduction φ_{PF} (shown in figure 2.9) will increase with *E* and with *T*, resulting in a further decreased barrier φ_t. Thus, the slope of the conduction band in figure 2.10 would steepen [*114*].

2.3.6 Ohmic Conduction

Ohmic conduction is the result of the movement of mobile electrons in the conduction band of a material, and/or the movement of holes in the valence band [*99*]. Ohmic conduction can be expressed in terms of the relationship between current density and electric field, as such:

$$J = \sigma E \tag{21}$$

where σ is the electrical conductivity, which is the reciprocal of the electrical resistivity of the material ($\sigma = \frac{1}{\rho}$, where ρ is the resistivity of the material, and $R = \rho \frac{d}{A}$, where d is the distance between two points in the field; E and J are electric field and current density respectively, as defined on page 38). Because of this, equation 21 is analogous to the relationship between current, voltage and resistance:

$$I = \frac{V}{R} \tag{22}$$

as given by Ohm's Law. It is noted [*59*, *99*, *116–119*] that memristors typically exhibit Ohmic conduction behaviour at a low bias (for our devices this is typically < 1 V in magnitude), displaying a linear relationship between current density and electric field with a slope very close to 1. This is prior to the resistive switching of the device, and can occur in both the low resistance state (LRS) and the high resistance state (HRS). This is because in each of the other conduction mechanisms described here, a high enough voltage (or electric field) is required to supply enough energy for the

mechanism to occur (for example, to supply enough energy to electrons in the metal to exceed the Schottky barrier level). This low-voltage Ohmic behaviour is a general feature of memristors, although the specific voltage(s) at which Ohmic behaviour stops is material- and configuration-specific.

Figure 2.11 shows an energy band diagram for the Ohmic conduction mechanism.

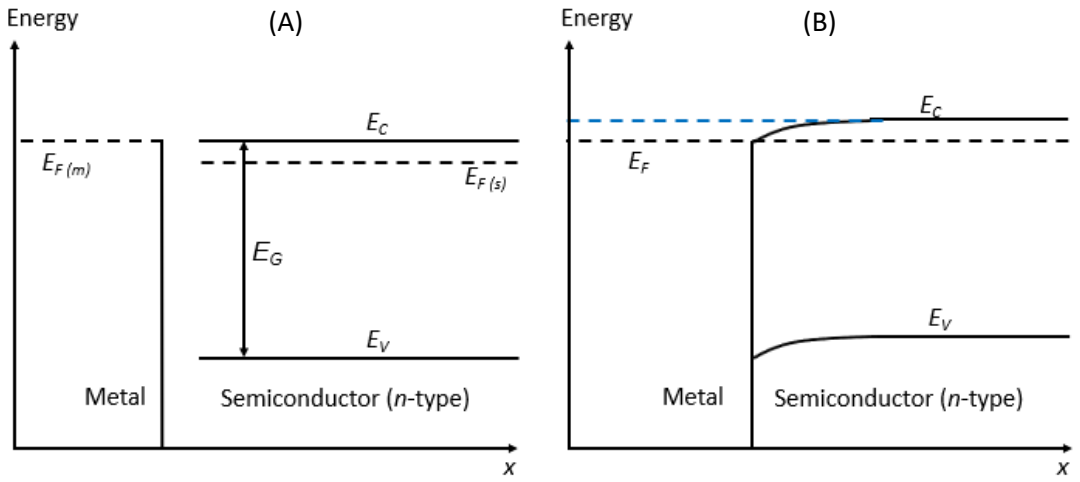

Fig. 2.11: An energy band diagram for an Ohmic contact formed at an interface between a metal and an *n*-type semiconductor; (A) shows the energy band diagram for the metal and semiconductor before contact, while (B) shows the band diagram for when the contact is formed. The magnitude of band bending for the conduction and valence bands at the contact is very small; as a result, there is virtually no potential barrier between the metal and the semiconductor and so electrons can flow freely through the contact. Adapted from [*120*].

2.3.7 Space Charge Limited Conduction

Space Charge Limited Conduction (SCLC) is another bulk-limited conduction mechanism. In a solid material, the injection of electrons at an Ohmic contact causes

a space charge limited current [*99*]. SCLC can occur in a device where at least one contact can inject more charge carriers than the material has under thermal equilibrium conditions without the injection of carriers [*121*]. SCLC can be observed by plotting the current density vs. voltage relationship of a cell using logarithmic scales on the axes for both; the curves can typically be divided into at least 3 distinct regions. The first is the Ohmic region, which has a relationship of $I \propto V$ and is governed by Ohmic conduction as described previously in section 2.3.6. This regime ends once a high enough voltage, known as the transition voltage (V_{tr}), is reached, at which point charge traps in the bulk of the material begin to fill. When $V > V_{tr}$, the cell enters a regime known as trap-controlled space charge limited current (TC-SCLC) region, where the current density is governed by the equation:

$$J = \frac{9\mu\varepsilon\theta V^2}{8d^3} \tag{23}$$

where θ is the ratio of the free carrier density to the total carrier density (including both free and trapped carriers), d is the insulator/dielectric layer thickness, and other notations are as defined above [*99*]. This occurs as traps are being filled, and as such is a transitional region. This can be seen in the typical logarithmic *I-V* curve for SCLC as a region where $I \propto V^2$.

As the voltage increases further, and specifically once a threshold voltage, known as the trap-filled limit voltage (V_{TFL}) has been exceeded, the current density resulting from space charge limited current is described by the Mott-Gurney Law [*122*], given as:

$$J = \frac{9\mu\varepsilon V^2}{8d^3} \tag{24}$$

This equation is almost identical to equation 23, except that there is no dependence on *θ*. This regime is also referred to as trap-filled space charge limited conduction (TF-SCLC); again, $I \propto V^2$ in this regime. This specific region is also known as the Langmuir-Child's Law region [*99*, *123*], as the equation governing this region is an adaptation of Child's Law (named after C. D. Child, who proposed the law in 1911 to describe the SCLC in vacuum diodes [*124*]; Child's Law itself states that $J \propto \frac{V^{3/2}}{d^2}$). Figure 2.12, below, shows the typical regimes that indicate SCLC behaviour.

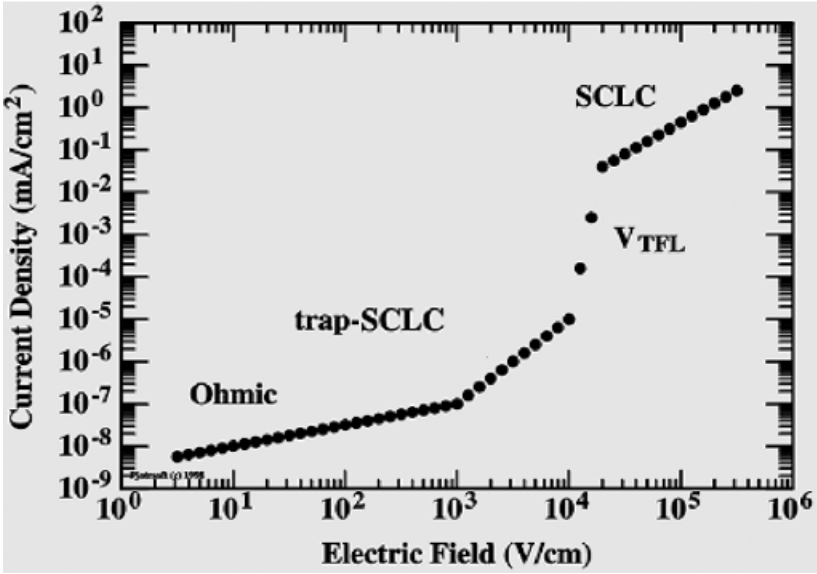

Fig. 2.12: A plot of current density vs. electric field, using logarithmic scale axes, demonstrating typical SCLC behaviour for a polymer semiconductor [*123*]. The plot can be broken up into four distinct regions, as labelled in the figure: the initial Ohmic region, where $I \propto V$; the TC-SCLC region (labelled here as "trap-SCLC"), where $I \propto V^2$; a trap charge limited conduction region, which is a transitional region where the current increases exponentially as the voltage

approaches the threshold V_{TFL}; and the TF-SCLC region (labelled as simply "SCLC" in the figure), where once again $I \propto V^2$.

As figure 2.12 shows above, other additional regimes can exist, typically when transitioning between the TC-SCLC and the TF-SCLC; in these regimes, typically referred to as trap charge limited conduction regions [*125*, *126*], the current increases exponentially, and $I \propto V^{\alpha}$, where $\alpha > 2$.

Figure 2.13 is a table summarising the transport mechanisms discussed in this chapter.

Mechanism	**Classification**	**Temperature Dependency**	**Plot Axes**
Fowler-Nordheim Tunnelling	Electrode-limited	No	$\ln(J/E^2)$ vs. $1/E$
Schottky Emission	Electrode-limited	Yes	$\ln(I)$ vs. $V^{1/2}$
Poole-Frenkel Emission	Bulk-limited	Yes	$\ln(I/V)$ vs. $V^{1/2}$
Ohmic Conduction	Bulk-limited	Yes	I vs. V
SCLC	Bulk-limited	Yes	I vs. V (logarithmic axes)

Fig. 2.13: A table summarising the different transport mechanisms, as discussed in this chapter.

2.4 Switching in ZnO Materials

Zinc oxide is currently of high interest to the scientific community because it can be easily produced in a variety of different nanostructures (examples include nanoflowers and nanoplates [*127*], nanowires [*31*], nanoparticles [*128*], and thin films [*50*]). Three commonly-used structures of ZnO are nanoparticles, thin films and nanorods. These different structures of ZnO typically present different switching mechanisms, based on the physical properties of the ZnO form.

Schottky contacts can be produced on *n*-type ZnO devices, using various different electrode materials. It is known that Al contacts with ZnO produce many dissociated cations (Zn) in the ZnO due to the strong reaction of Al with anions (O) in ZnO. As a result, such contacts have a low barrier height and leakage current [*66*]. Au can be used to create a Schottky contact, having a high work function that produces a barrier height of 0.8 eV as shown in figure 2.6. However, Au Schottky contacts with ZnO have been observed to result in poor *I-V* characteristics. In addition, devices degrade easily with thermal cycling of the samples [*66*, *129*], due to reactions between the Au electrode and the ZnO surface [*130*].

In thin films of ZnO, filamentary ECM switching can occur if the films are only a few tens of nm thick, as discussed in section 2.3.1. The ZnO semiconductor would kinetically hinder the diffusion and formation of metallic filaments through its bulk in thicker films [*87*, *89*]. Nanorods and nanowires allow thicker layers to be produced; conductive channels are produced by active electrode atoms moving along the

surface of the nanorod/wire instead of travelling through the bulk, doping the surface of the ZnO nanorod/wire with active adatoms rather than forming continuous filaments [*87*].

The switching behaviour of ZnO is very complex, as it combines several switching mechanisms. Both Schottky and Poole-Frenkel emission behaviour can be observed in thin films and nanorod/wire devices (attributed to the naturally-occurring traps and defects in ZnO, in the forms of zinc interstitials (Frenkel defects [*63*]) and oxygen vacancies (Schottky defects [*64*]) [*65*]), or in nanoparticle devices where the electrodes directly contact the semiconductor; however, it has been observed [*97*] that Schottky emission is the most dominant conduction mechanism in the high electric field region for all configurations of their devices. This is likely a result of the differences between Schottky emission and Poole-Frenkel emission; while the two are similar mechanisms, Schottky is electrode-limited, while Poole-Frenkel emission is bulk-limited [*99*]. As such, modification of the bulk material (in this case, the ZnO layer) may affect the Poole-Frenkel emission behaviour, while the Schottky emission will remain unaffected due to keeping the electrode configuration the same for all devices. Poole-Frenkel emission occurs in insulators and semiconductors only if the low-field conductivity is dominated by a donor state (meaning that the thermodynamic Fermi level contains the energy of the donor state) for an *n*-type material, which has a Coulomb-attractive centre [*131*]. As such, it is possible for materials to exhibit Schottky emission without being able to exhibit Poole-Frenkel emission, if the Fermi levels align in such a way that they do not contain the energy levels of the donor states. ZnO, typically occurring as an *n*-type semiconductor with

a very rich defect chemistry, is a material for which the Poole-Frenkel effect can have a strong contribution to the switching mechanism.

Space charge limited conduction (SCLC) also occurs in ZnO. Defects in the ZnO give rise to oxygen vacancies and traps, which are responsible for the effects of SCLC in the material. As mentioned in section 2.3.7, different resistance regimes can be observed as SCLC effects manifest due to the filling (or emptying) of traps in the material.

Another mechanism that has been observed in ZnO structures is associated with the adsorption of oxygen at the surface of ZnO nanocrystals, where oxygen vacancies may be present. The adsorbed oxygen acts as a trap for free electrons and creates a barrier to prevent electron injection [*128*]. When a forward bias is applied, oxygen ions near the interface between the ZnO and the electrode drift into the bulk, leaving oxygen vacancies at the interface that molecular oxygen can adsorb onto. A reverse bias moves the oxygen ions that had drifted into the bulk back to the interface, releasing the molecular oxygen that adsorbed there. If no molecular oxygen is present (such as in a vacuum), this mechanism cannot occur.

2.5 Current Memristor Technologies

Hewlett-Packard was the first company to construct a working memristor in 2008, based on titanium dioxide (TiO_2) as the switching material sandwiched between

platinum (Pt) electrodes. Researchers still use the basic model for HP memristors, though often with different materials for the switching layer and electrodes. Normal configurations are metal-oxide-metal based memristors. Typical results for "HP-type" memristors have given on/off resistance ratios of ~ 10^2 or 10^3 [*132*], which is apparent in the I-V sweep data as a difference between the LRS and HRS of two – three orders of magnitude. Endurance for memristors has developed and improved over the years since the initial HP memristor was announced, and memristors can currently endure beyond 10^{12} switching cycles, with switching times of ~10 ns [*133*]. Devices are also reported to have retention (the characteristic that describes how well a memristor is able to remain in a given resistance state once power is no longer supplied) of 10 years at 85°C [*133*].

HP are not the only group interested in the memristor, however. Researchers at Knowm, a small company based in Santa Fe, New Mexico, have also been developing their own brand of memristors, based on tungsten, and have managed to produce commercially-available memristors with bi-directional incremental learning capability [*134*]. These devices operate at low voltages (recommended operating voltages are <1 V), with high cycle endurances (typical devices can survive about 10^8 cycles) and typical on/off resistance ratios advertised at around 2 x 10^2 [*134*].

Figure 2.14 shows an image of the research die for Knowm's memristors. Knowm's memristors require a forming step in order to fully form the conductive pathways for

the device's operation. In addition, the devices are very sensitive to high applied voltages, and are designed to operate at less than 1 V magnitudes. Beyond this voltage, phase-changes can occur, or non-reversible damage can occur to the devices [*134*].

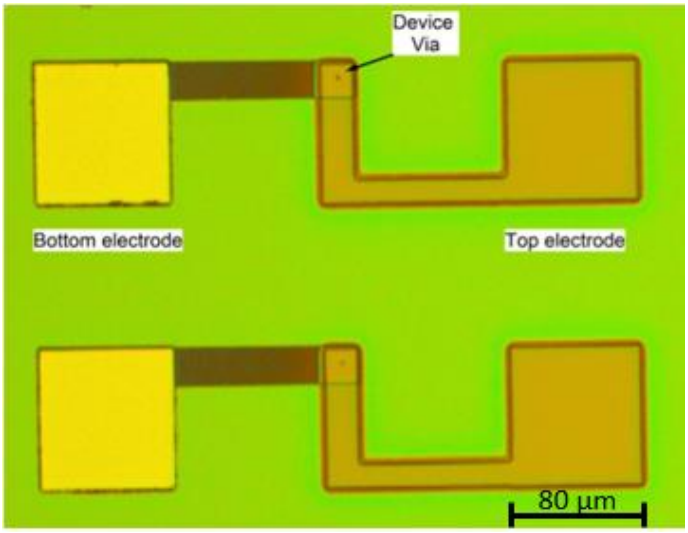

Fig. 2.14: An image of two Knowm memristors side by side; this is a close-up image of the research die taken through a microscope. Image taken from the Knowm website [*134*].

Kris Campbell, the developer of the Knowm memristor, explains that he chose to use chalcogenide materials instead of metal oxide materials as the switching material in his devices because oxides are "very difficult to design a stable device with. First, it is very difficult to control the concentration of oxygen within a film. Fabrication techniques become complicated every step of the way. Keeping oxygen out of the device after fabrication is also challenging" [*134*]. He also explains that device-to-

device variation occurs in the oxide-based memristors he fabricated, and that higher switching voltages were required, while the devices exhibited poor retention of their resistance states and showed erratic behaviour within the same device. He explains that, in his opinion, “it is difficult to fabricate devices with metal-oxides since it is difficult to control or regulate the concentration of oxygen in the device”, and that devices may give “different results due to any small change in the way the wafers were processed”, and that “different film deposition methods will produce devices with drastically different electrical characteristics” [*134*]. However, he also clarifies that he has not personally tested any of the devices produced by Hewlett Packard.

For a new memory technology to be viable in today’s market, it must achieve several key criteria, especially if it wishes to qualify as a universal memory:

- Read/write speeds need to be in the order of nanoseconds, ideally competing with DRAM for speed and surpassing Flash memory [*135*];
- Devices should have endurances that last for millions, if not billions, of cycles, ensuring that a device can continue to operate for several years (typically tens of years, to compete with and exceed Flash memory) [*136*];
- In addition, devices should be able to retain their states for very long periods (years, at least), demonstrating longevity of the device [*136*];
- Devices should be scalable, so as to optimise capacity for data storage [*136*];

- The different memory states must be distinguishable [*137*].

- Devices should have low susceptibility to physical damage. To ensure this, devices should ideally operate at low voltages, and particularly with low currents, as this keeps the power passing through the device low, using less energy and generating less heat, and lowering the potential for damaging the device in doing so [*136*].

Campbell's comments suggest that oxide-based memristors have difficulty meeting several of these criteria. High voltages would be needed to switch the devices, and with such variation from one device to the next (and also erratic behaviour in the same device), states could not clearly be said to be distinguishable in all instances. Retention is also reported by Campbell to be poor. He acknowledges that these characteristics are for devices based on oxygen vacancy migration, and that "the published literature for HP's devices claim it is comprised of a metal oxide material that relies on the migration of oxygen vacancies to alter the resistance of the device", and that the observed behaviour is related to the volume of the device, making the mechanism "a 'bulk' migration, not necessarily a filament through the device" [*134*]. It is noted, however, that several patents exist for metal-oxide based memristive systems that support development of devices using oxygen vacancies that also exhibit filament formation. It is possible that these devices do not have the same issues as were observed in "HP-type" bulk switching devices.

Currently, our memristor devices are still not optimised. The main focus of this research has been to identify the switching mechanisms in our devices, as well as to develop the fabrication method to allow for rapid mass-production of memristor devices at low cost. On/off ratios for our devices have been typically ~ 1 order of magnitude, which does not yet compete with cutting edge technologies that achieve magnitudes of 2 – 3 orders [*132*]. Understanding the underlying transport mechanisms responsible for hysteresis, however, will set a strong foundation for determining how best to improve the on/off ratios for our configuration.

2.6 Summary

This chapter has discussed memristor theory as developed by Leon Chua in 1971, and the development of the physical TiO_2-based memristor device by HP in 2008. Following this, the different transport mechanisms that have been typically observed and identified for memristive systems – Electrochemical migration, Fowler-Nordheim tunnelling, Schottky emission, Poole-Frenkel emission, Ohmic conduction and Space-charge-limited conduction – have been described and discussed, both in relation to how each mechanism typically works and in respect to how it has been observed in ZnO-based devices. Many of the mechanisms discussed are known to occur in ZnO-based systems, and it is explained that Schottky is often the most dominant of the mechanisms in ZnO-based devices, although several mechanisms could be involved at once. A brief description of cutting edge memristor technologies is given, discussing some of the known issues with oxide-based memristor

technologies, and briefly explaining how our current devices compare to the state-of-the-art.

Chapter 3

Review of ZnO Nanorod Growth Methods

This chapter reviews some of the commonly-used methods of depositing/growing ZnO nanorods. Each deposition method will be discussed in terms of a typical procedure for that method, the benefits of using that method, and the disadvantages of the method in question.

The methods discussed in this chapter are:

- Physical Vapour Deposition (PVD)
- Chemical Vapour Deposition (CVD)
- Electrochemical Deposition
- Chemical Bath Deposition (CBD)/Hydrothermal Growth

3.1 Physical Vapour Deposition (PVD)

Physical vapour deposition (PVD) methods are vacuum deposition methods that are typically used to deposit thin films of material. Common PVD methods include thermal evaporation of ZnO [*138–141*], sputtering [*142–144*] and evaporation by electron beam [*145*]. PVD methods deposit films using a source of the material to be deposited, and do not involve a chemical change of a material to form the desired deposit material; the source material simply undergoes a physical change of phase from solid to gas (vapour), and then condenses on the surface of the substrate, forming the desired thin film.

In a thermal evaporation method, a high current is applied to a crucible containing the material to be deposited. The high current heats the crucible (often made of tungsten or another metal with low resistivity and high melting temperature) which vaporises the material once it reaches sufficient temperature. The vaporised material then transports to the substrate that is suspended above it, where it condenses and is adsorbed onto the surface [*146*]. This is carried out under vacuum.

Figure 3.1 demonstrates a typical thermal evaporation method.

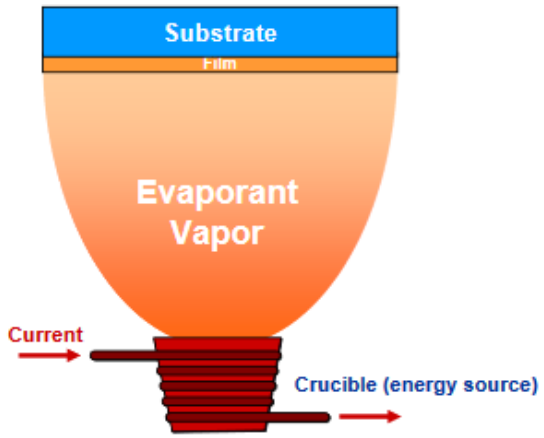

Fig. 3.1: A diagram showing how thermal evaporation typically works [*146*].

An electron beam (e-beam) evaporation method, which is a variation of thermal evaporation methods, involves passing a current through a tungsten filament, leading to joule heating and electron emission. A high voltage is applied between the filament and the hearth which accelerates the electrons towards the crucible containing the material to be deposited. The electrons are focused into a beam by a strong magnetic field [*147*]. The energy of the beam is transferred into the material, heating it and causing it to evaporate/sublimate, and the evaporated material is deposited onto the substrate that is suspended above the crucible.

Figure 3.2 shows the electron beam deposition process.

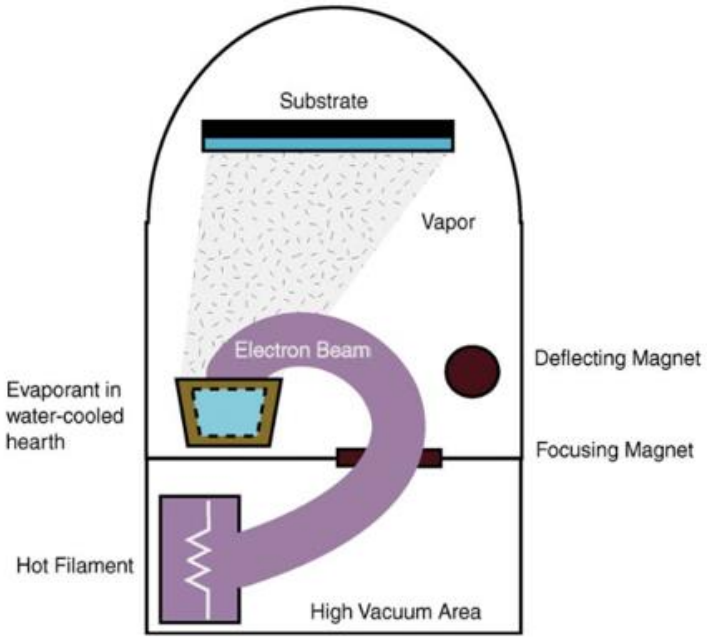

Fig. 3.2: A diagram showing the typical processes involved in the e-beam evaporation deposition method [*148*].

Both thermal evaporation and e-beam deposition require expensive chambers and systems to work (a benchtop dome-based evaporator system may cost thousands of pounds, while e-beam equipment can cost significantly more), and require very high operating temperatures for deposition of ZnO (800°C - 1200°C). Thermal evaporation can also have issues with impurities, as the container material can evaporate along with the desired source material; e-beam evaporation does not suffer this to the same extent [*146*].

Sputtering is a very different method of physical vapour deposition than thermal/e-beam evaporation. A source of the desired material is placed on a cathode, while the substrate is placed on an anode, both in a chamber containing an inert gas

(typically argon, Ar). A DC voltage is applied under high vacuum to generate an electrical field by accelerating free electrons in the chamber; these free electrons collide inelastically with the Ar atoms, ionising the atoms to form Ar^+ while also generating more electrons as a result of the ionisation. These electrons cause further collisions as above, and a plasma is generated as a result of the ionisation process. The positively charged ions accelerate toward the cathode, bombarding the target and removing the material, which is then transported to the substrate at the anode via transfer of momentum [*146*].

Compared with evaporation methods, sputtering produces a more uniform film but with poor directionality. In addition, atoms of the inert gas are often implanted into the film. Figure 3.3 compares evaporation techniques with sputtering techniques, showing a table with the advantages and disadvantages of each.

Evaporation	**Sputtering**
Low energy atoms (~ 0.1 eV)	High energy atoms / ions (1 – 10 eV) • denser film • smaller grain size • better adhesion
High Vacuum • directional, good for lift-off • lower impurity	Low Vacuum • poor directionality, better step coverage • gas atom implanted in the film
Point Source • poor uniformity	Parallel Plate Source • better uniformity
Component Evaporate at Different Rate • poor stoichiometry	All Component Sputtered with Similar Rate • maintain stoichiometry

Fig. 3.3: A table comparing the advantages and disadvantages of evaporation techniques vs. sputtering techniques [*146*].

3.2 Chemical Vapour Deposition (CVD)

Chemical vapour deposition (CVD) methods are often similar to PVD methods, except that they involve the chemical reactions of gaseous reactants on or near the vicinity of a heated substrate surface [*149*]. Typical CVD methods for depositing ZnO involve the use of a furnace, in which Zn vapour is generated by heating the source material to high temperature (typically 500°C or greater [*150*, *151*]) and is reacted with oxygen gas injected into the system. A seed layer can be used to generate more preferential and uniform nucleation sites for growth of the ZnO film [*150*, *151*].

The basic steps in a typical CVD process can be summarised as follows [*152*]:

- The precursor reagents are evaporated and transported via flow of an inert gas into the reactor;
- Gas phase reactions of precursors in the reaction zone produce reactive intermediates and gaseous by-products;
- Reactants are transported to and adsorbed onto the substrate surface;
- Surface chemical reactions and nucleation occurs via surface diffusion at growth sites, leading to formation of the thin film;
- Remaining fragments of the decomposition are desorbed and transported away from the reaction zone.

Figure 3.4 shows a basic schematic of a typical CVD reactor.

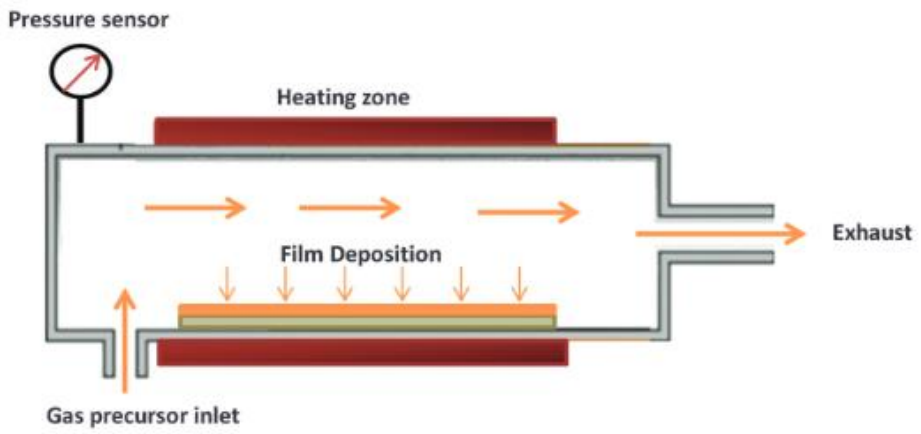

Fig. 3.4: A schematic of a typical CVD reactor system [*153*].

CVD has several disadvantages over other deposition methods. The substrate is heated to very high temperatures (usually between 300°C and 900°C), which can damage or destroy substrates that cannot handle such high temperatures [*154*]. This is in contrast to PVD methods, where the substrate itself is not heated at all. Much like PVD, CVD methods require expensive equipment (furnaces can cost tens of thousands of pounds). However, CVD does not require as high a vacuum as PVD techniques, and due to the relative ease with which impurities can be removed from precursor vapours using distillation techniques, CVD typically produces films of higher purity than PVD [*154*].

3.3 Electrochemical Deposition

Electrochemical deposition, or electroplating, is a process that deposits material onto a conducting surface from a solution that contains ionic species. For electrochemical deposition of ZnO, a zinc salt (for example, zinc nitrate [*155*, *156*]) is used in the electrolyte solution to provide Zn^{2+} ions and OH^{-} ions needed for the reaction (the

solvent in this case is water). A three-electrode system is used to apply electrical current through the solution: the “working electrode”, which is the electrode through which the desired electrical potential is applied, as well as the object that is to receive the coating; a “reference” electrode, which is used to act as a fixed reference point for a potentiostat, and through which no current should be passed; and a “counter electrode” which completes the circuit with the working electrode [*157*]. As electrical current is passed through the circuit, the working electrode donates electrons to the ions in the solution, resulting in the deposition of neutrally-charged material (ZnO) at the working electrode. Figure 3.5 shows the schematic for a three-electrode electrochemical deposition system.

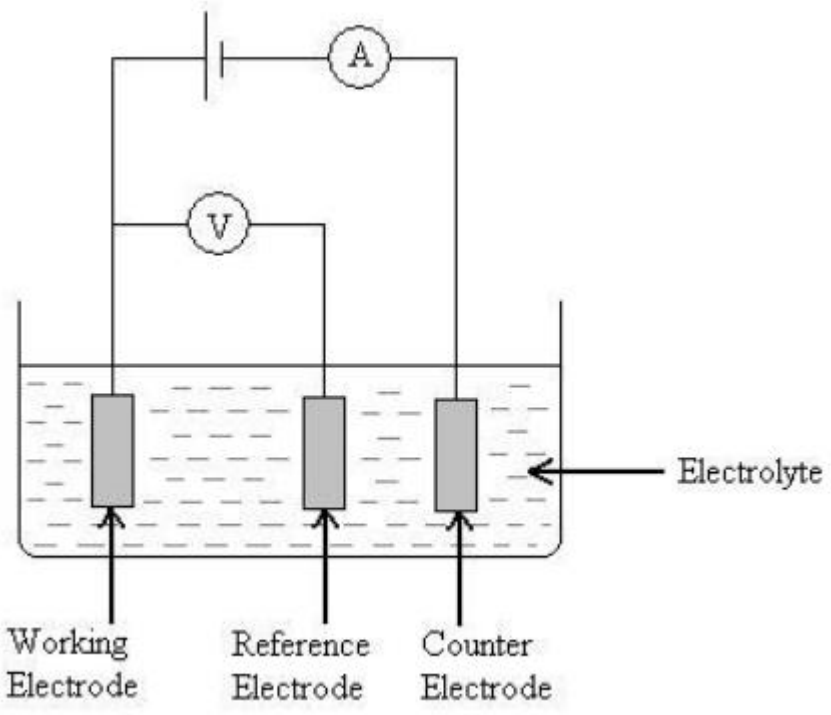

Fig. 3.5: A schematic diagram of the three-electrode electrochemical deposition system [*157*].

This method has advantages over PVD and CVD, in that it does not require high temperatures or expensive equipment for the procedure to be carried out. In addition, high quality thin films can be produced more easily than in physical deposition techniques, with electrodeposits being able to be produced under conditions equivalent to a vacuum deposition condition of 5 x 10^{-10} mbar [*158*]. However, films produced using electrochemical deposition methods may not be very uniform. In addition, as the ZnO is deposited onto the working electrode, it means that the films can only be deposited using this method onto very specific substrates (i.e. metallic, conducting substrates) [*159*].

3.4 Chemical Bath Deposition (CBD)/Hydrothermal Growth

Chemical bath deposition (CBD) involves the formation of a solid phase of material (typically crystalline) from a solution onto a substrate [*160*]. Hydrothermal growth is a form of CBD, using thermal energy provided by heating to stimulate the growth of the desired material. This often involves the use of an additional reducing agent, which provides ions that aid with the initiation of the chemical reactions. For ZnO, the most commonly used reducing agent is hexamethylenetetramine (HMTA), as it ensures crystalline and morphological properties in the ZnO that are superior to those provided by other reducing agents. This is due to the double role of HMTA as a supplier of OH^- ions and as a capping agent that attaches to the non-polar facets of the ZnO nanorods, promoting anisotropic growth [*161*]. This is discussed in more detail in section 4.1.2 of chapter 4.

Using a CBD method, ZnO is formed as a result of a series of chemical reactions in the bath, which are as follows [*31*]:

- HMTA decomposition reaction:

$$(CH_2)_6N_4 + 6H_2O \rightarrow 6HCHO + 4NH_3 \quad (25)$$

- Hydroxyl supply reaction:

$$NH_3 + H_2O \leftrightarrow NH_4^+ + OH^- \quad (26)$$

- Supersaturation reaction:

$$2OH^- + Zn^{2+} \rightarrow Zn(OH)_2 \quad (27)$$

- ZnO nanorod growth reaction:

$$Zn(OH)_2 \rightarrow ZnO + H_2O \quad (28)$$

A pre-formed seed layer (pre-formed using another deposition technique, or spin-coated onto the substrate) or a suitably rough substrate allows for vertically oriented ZnO nanorods to be grown. A well-formed seed layer is typically the better option, giving more control over the morphology and crystallinity of the nanorods produced. This will be discussed in more detail in chapter 4.

Historically, ZnO nanorod growth through CBD has had the drawback of lack of good control over growth kinetics, and reproducible growth has been difficult to achieve, compared with vacuum techniques such as PVD [*161*]. CBD methods also produce more waste in general, as the bulk of the reacted material remains in the solution after growth. On the other hand, CBD methods can be used for growth of ZnO nanorods on a larger variety of substrate materials using simple techniques, without the need for high temperatures, vacuum systems, and costly materials.

3.5 Summary

In this chapter, several of the commonly-used methods for depositing ZnO nanoscale structures have been discussed. The advantages and disadvantages of each method have been examined, with CBD methods, including hydrothermal growth, having key advantages in the simplicity of the techniques, low-temperature operation, and cost-effective procedures that do not require expensive systems.

Chapter 4

Experimental Methodology

In this chapter, the methods used to fabricate and test the devices shall be detailed. Fabrication of devices is a multi-stage process comprised of the following:

- Deposition of the bottom electrode contact by thermal evaporation,
- Deposition (and proper formation) of the seed layer used to guide nanorod growth, by spin-coating and annealing of the zinc salt precursor material (zinc acetate dihydrate) to decompose this material into ZnO seeds,
- Growth of the nanorods themselves via microwave stimulation of zinc salt (specifically zinc nitrate hexahydrate), and
- The deposition of the top electrode.

An additional step can also be added, whereby an insulating polymer layer can be introduced prior to deposition of the top electrode. Section 4.1 describes these procedures in detail.

Section 4.2 details the methods used for investigating the samples produced. Scanning Electron Microscopy (SEM) is used to investigate the surfaces of the samples, showing the morphologies of nanoscale particles.

Section 4.3 explains the methods used for electrical measurements of the memristor devices. This includes details on the methods for I-V sweeps (in ambient conditions in air, and in a pure nitrogen environment), and retention and endurance measurements.

4.1 Fabrication of Devices

There are four key steps to the fabrication process for producing the memristors used in this project: initially, bottom electrode contacts need to be deposited; our switching material must then be formed and deposited onto the substrate; an insulating layer may then be spin coated onto the sample (this is not always necessary for production of the memristor but it does provide advantages as will be explained later in this chapter); finally, a top electrode contact is deposited onto the sample.

Figure 4.1 shows the basic configuration for a device produced with an ITO bottom electrode.

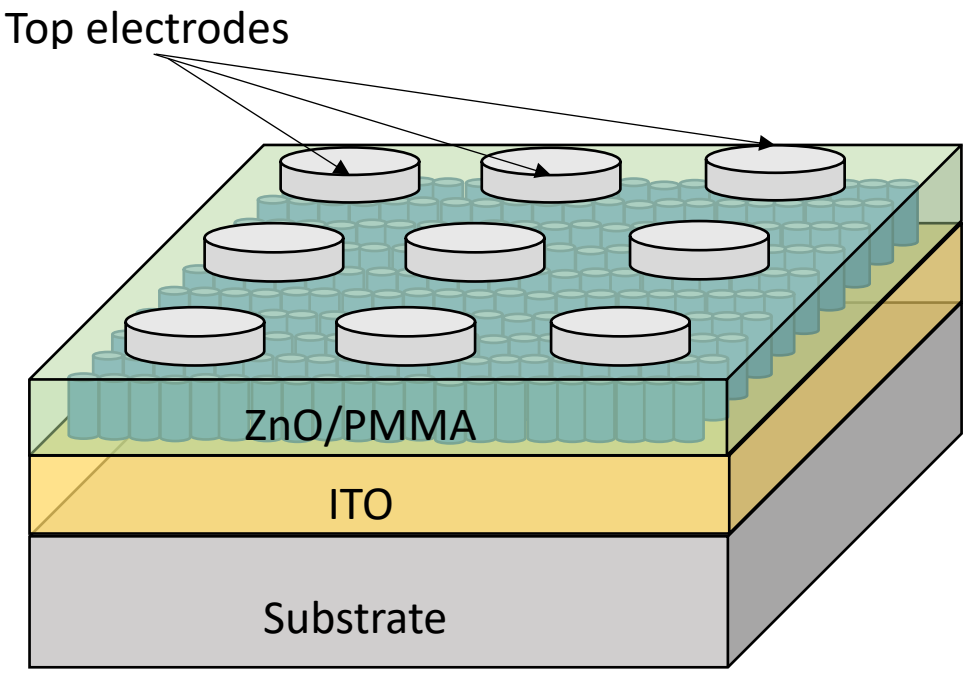

Fig. 4.1: A diagram of the basic configuration for a device made with an ITO bottom electrode. Top electrode sizes are 100 nm, 200 nm or 400 nm diameters.

Fig. 4.2 shows the schematic for a “crossbar” arrangement using two metal electrodes. Separate shadow masks, purchased from Tecan Ltd., were used to produce the bottom electrodes and top electrodes, to ensure alignment was correct so that each bottom electrode could be used for up to 10 top electrodes, creating 10 active device areas. For simplicity of explanation, the figure shows only small active regions of switching material between the electrodes; in reality, the switching material (ZnO either alone or embedded in PMMA) covers the entire surface of the substrate, including all bottom electrodes. The complete device exists where the two electrodes cross, with only the switching material between the two electrodes being part of the device. As the top electrodes are isolated to only one bottom electrode, there are no cross-paths available in this configuration that would cause current leakage.

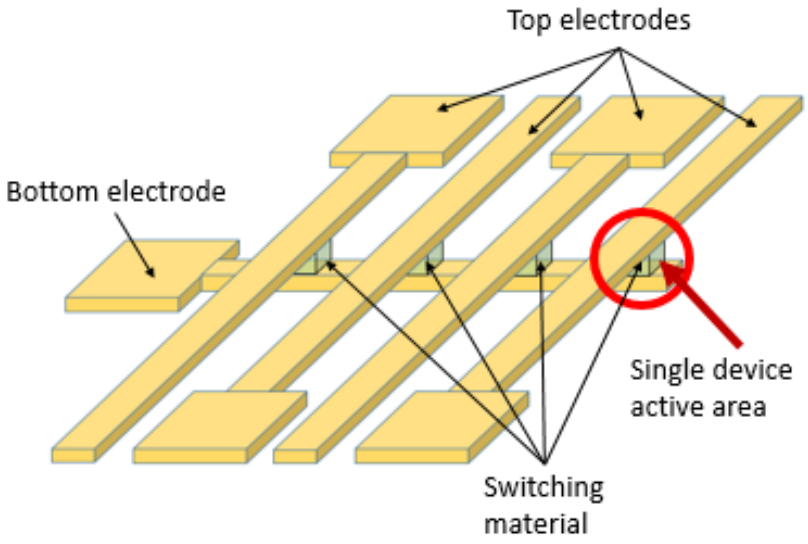

Fig. 4.2: A schematic of the “crossbar” arrangement for memristors produced using our method. The electrode pads are 400 nm x 400nm area, while the device “active area” is either 100 nm x 100 nm, 200 nm x 200 nm, or 400 nm x 400nm.

The rest of this section will discuss in more detail the four key steps in the fabrication process.

4.1.1 Electrode Deposition

Two electrodes, representing the two terminals of the memristor device, are required for the memristor to operate as a complete device. In this project, three different electrode materials were used: aluminium (Al), gold (Au) and indium tin oxide (ITO), a transparent conductive film. In the case of ITO, polished float (soda lime) glass substrates were purchased from Delta Technologies Ltd. with a 120 – 160 nm coating of ITO on one side. The sheet resistance of the ITO-coated substrates was 15 – 30 Ω/sq. These substrates are cleaned by ultrasonication in acetone, propan-1-ol, and 16 MΩ deionized water for 5 minutes each, and are then dried with nitrogen gas.

For the metal electrodes, a vapour deposition method is used. Glass substrates with no ITO coating are used for these samples and are cleaned using the above ultrasonication method prior to electrode deposition. An Edwards E306A dome chamber thermal evaporator system with a rotary pump and a diffusion pump is used to bring the pressure inside the dome to a vacuum of ~4 x 10^{-6} mbar, at which point pellets of Al or Au are evaporated (using a tungsten basket microelectronic source for evaporation of Al, and a tungsten thermal evaporation boat source for evaporation of Au) by increasing the current passing through the evaporation sources until the source is hot enough to melt and evaporate the material. A shadow

mask, obtained from Tecan Ltd. and specially designed by Dr. Emanuele Verrelli from the University of Hull for our use, is used to create the electrodes in the appropriate shapes and sizes; where ITO is used as the bottom electrode, circular electrodes of diameters 100 µm, 200 µm and 400 µm are used, while two sets of masks are used to create crossbar configurations for the paired metal electrodes, with cross sections of widths 100 µm, 200 µm and 400 µm.

Prior to evaporation of Au as a bottom electrode, a thin layer of chromium (Cr) is evaporated as an aid to adhesion. Only a thin layer of approximately 20 nm is used, for an Au bottom electrode of thickness ~120 nm. All electrode thicknesses are kept to ~120 nm. To investigate the significance of electrode material regarding the switching properties of the nanorod devices, separate devices were fabricated with different combinations of electrode material configurations: ITO + Al, ITO + Au, Au + Al, and Au + Au. Al was not used as a bottom electrode, as the growth method is hydrothermal, and the procedure oxidizes the Al bottom electrode rapidly but not uniformly.

4.1.2 ZnO Nanorod Growth Procedure

The microwave synthesis method used in this project was adapted from previously published methods [*59*, *162*].

- A 10 mM solution of zinc acetate dihydrate (99%, Sigma-Aldrich) in propan-1-ol was spin coated onto the sample at 2000 rpm for 30 seconds, followed

by annealing on a hot plate at 350°C for 30 minutes. This aligns the crystalline structure of the seeds so that vertical nanorods grow. The spin coating and annealing steps are repeated 3 times to ensure a uniform coating.

- The samples are then placed into vials containing 25 ml each of a 25 mM (equimolar) solution of zinc nitrate hexahydrate (99%, Sigma-Aldrich) and hexamethylene tetramine (99.5%, Sigma-Aldrich) dissolved in deionized water. The solution itself is prepared as a single batch, using 200 ml of deionized water to dissolve 1.5 g of zinc nitrate hexahydrate and 0.71 g hexamethylene tetramine.

- This solution is then heated using a MARS 5 (CEM) scientific microwave, using a ramp to temperature method that brings the bath to 80°C and then holds the bath at that temperature for the desired heating duration. The vials are sealed with caps that allow for pressure control (which is carried out by the microwave itself; maximum allowed pressure is set to <50 PSI, but in testing the vial pressure never exceeded 10 PSI), with a temperature probe in one vial acting as a control sample for temperature control. The effect of different microwave power and heating times has been investigated and will be discussed in chapter 5.

The hexamethylene tetramine (HMTA) serves three main roles: it provides the OH^- ions needed to initiate the hydroxyl reaction; it acts as a pH buffer within the solution, as the hydrolysis rate of HMTA is decreased by an increase in pH and vice versa; it

also attaches to the non-polar facets of the nanorods during growth, preventing the access of Zn^{2+} ions to these facets and thereby leaving only the polar (001) face for epitaxial growth [*31*, *163*]. It is believed that high supersaturation levels favour nucleation while low supersaturation levels favour crystal growth [*31*, *164*], and as such HMTA's role as a pH buffer is key. The alignment, crystallinity and size of the seed layer are known to govern the alignment and morphology of the nanorods grown through this procedure [*31*, *164*, *165*].

A procedure for using a domestic microwave instead of the Mars 5 scientific microwave was also used. In this procedure, post-seeding using the procedure above, the samples are submerged in a small crystallizing dish containing 50 ml of growth solution. For rapid heating, the dish containing the substrate and the solution is then heated by itself in the microwave; reducing the rate of heating can be achieved by submerging the dish in a larger bath containing water. The heating profile of the commercial microwave can be adjusted in this way to replicate that of the Mars 5, although there is no pressure control in the commercial microwave and maintaining the temperature post-ramping is more difficult.

Figure 4.3 on the following page shows the heating profiles of the different settings for each microwave. The figure shows that the heating profiles for both high-power and low-power heating using the Mars 5 scientific microwave are linear until the very last stages of heating (where heating is reduced to limit the overshooting effect, ensuring that the temperature remains within ~1°C of the target temperature); The heating profiles for heating via domestic microwave are less linear (which can be

seen more clearly in the inset), although they do match the profiles from the Mars 5 quite closely.

The Mars 5 can maintain the temperature (within 1°C of the desired temperature of 80°C) throughout the duration of the experiment, as shown in figure 4.3. As the domestic microwave lacks the control to do this, it must be done manually and separately to avoid deviating too greatly from the desired temperature. As such, there is no post-ramp data for the domestic microwave curves.

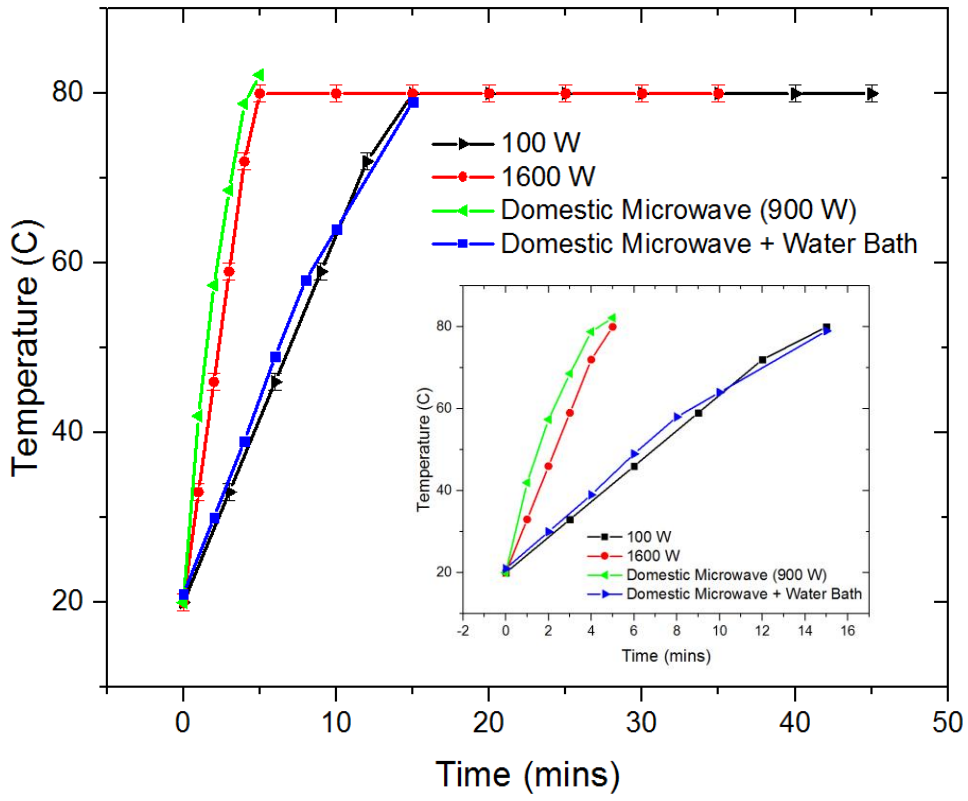

Fig. 4.3: Temperature profiles for the two methods of heating using the Mars 5 microwave: the 100 W heating method, which takes 15 minutes, and the 1600 W heating method that takes 5 minutes. Temperature remains steady after ramp. Inset shows the temperature profile for only the ramping step. For the work in this thesis, the 100 W and 1600 W Mars 5 heating methods

were used, as they allowed greater control over the temperature and pressure, especially post-ramp; the domestic microwave settings are included as a domestic microwave is considerably cheaper to purchase than a scientific-grade microwave, and this data demonstrates that the ramping stage for the Mars 5 can be approximated using a domestic microwave.

After any of our growth procedures is carried out, the solution in the vials turns a milky-white. This is because of the zinc oxide precipitating into the solution, producing nanostructures.

4.1.3 Deposition of Insulating Layer

Prior to deposition of the top electrode, a layer of polymethyl methacrylate (PMMA, weight average molecular weight of ~120,000 by GPC, ordered from Sigma Aldrich) is typically deposited, by spin-coating a single coat of PMMA solution (either 5% or 10%, by weight, dissolved in toluene) for 30 s at different spin speeds (1000 rpm, 2000 rpm, or 3000 rpm) onto the sample surface, and then annealing at 100°C for 30 minutes. Varying the spin speed and the PMMA concentration in this way can be used to vary the thickness of the PMMA layer produced (this is discussed further in chapter 5): spin coating a 10% concentration PMMA solution at 1000 rpm will produce a layer of ~350 nm thickness; using a 2000 rpm spin speed with the same concentration produces a layer of ~220 nm thickness, while 3000 rpm at the same concentration produces a ~150 nm layer. Using a 5% concentration, 1000 rpm produces a layer of ~ 250 nm; 2000 rpm produces a ~180 nm layer, and 3000 rpm produces a layer of ~100 nm (all thicknesses were measured using a Dektak XTL Stylus Profilometer).

While it is not strictly necessary for the memristor device to function, the addition of this layer (when deposited uniformly) was found to significantly improve device stability and switching behaviour. The PMMA layer also helps to reduce surface roughness of the nanorod-coated substrate prior to electrode deposition.

4.2 Investigation

4.2.1 SEM

To investigate the morphology, uniformity and alignment of the nanorods, a scanning electron microscope (SEM) was used. Specifically, the SEM used was a Zeiss Evo 60 EP model SEM with an Oxford Instruments X-Max SDD 80 mm^2 area EDX spectrometer.

SEM uses a focused beam of high-energy electrons targeted at a solid substance to generate a variety of signals. A 2-dimensional image is generated from the signal received from the interactions between the electrons and the sample, displaying spatial variations in the data collected over a selected area of the sample surface. Standard SEM imaging is derived from the signals from secondary electrons produced when the incident electrons from the electron beam are decelerated upon contact with the surface of the sample, and show the morphology and topography of samples [*166*]. Raised areas on the sample surface, such as particles or nanorods,

give a stronger signal as they are closer to the detector, making those areas appear brighter in the image.

X-ray generation is produced by inelastic collisions of the incident electrons with electrons in discrete orbitals of atoms in the sample; the x-rays are emitted as the excited electrons in the sample return to lower energy states, and the fixed wavelengths of the x-rays emitted (related to the difference in energy levels of electrons in different orbitals for a given element) can be used to determine which elements are present in the material being imaged [*166*]. This technique, known as "Energy-dispersive X-Ray spectroscopy" (EDX), is an analytical technique that can be used to determine the chemical characteristics of a sample.

4.2.2 AFM

To investigate the seed layer, atomic force microscopy (AFM) was used. AFM uses an ultra-small probe tip at the end of a cantilever [*167*], using a laser-based light-lever detection method: a laser beam is directed at the cantilever and reflects to the detector; as the probe tip scans the sample surface, it is affected by the atomic forces of atoms in the scanned material, and the cantilever bends when the atomic forces change, indicating a change in the height of the material being scanned. This causes the laser beam to be deflected, and the variation in beam deflection allows a 3D image to be produced, using data collected in x, y, and z co-ordinates. The forces that cause the cantilever movement can be repulsive (when the cantilever tip is very close to the sample surface, a few angstroms' distance – this is known as "contact

mode") or attractive (due to Van der Waals' forces, when the tip is not as close to the sample surface – this is known as "non-contact mode) [*168*].

Tapping mode AFM (a technique that is in between contact and non-contact AFM) is used to obtain high resolution imaging while limiting damage to the sample. Tapping mode is a "low-contact" technique in AFM, obtaining images by alternately placing the cantilever tip in contact with the surface (providing high resolution) and then lifting the tip to prevent dragging the tip across the surface; this minimizes damage to the sample in cases where the material being investigated is soft, or otherwise easily damaged, as well as in cases where the material on the sample is poorly-adhered to the substrate and can be removed by dragging. Tapping mode "maps topography by lightly tapping the surface with an oscillating probe tip. The cantilever's oscillation amplitude changes with sample surface topography, and the topography image is obtained by monitoring these changes and closing the z feedback loop to minimize them" [*169*]. For this project, a Bruker Dimension Edge Large Sample AFM was used, alongside Bruker's NanoScope Analysis software for analysing the data.

4.3 Measurement

4.3.1 I-V Sweeps and Hysteresis

The current-voltage (I-V) characteristics of devices can give a lot of valuable information about the behaviour and mechanisms of a device's function. A standard

resistor has a linear, Ohmic response; a memristor, however, has non-linear regions, exhibiting a pinched hysteresis effect as the device switches through different behavioural regimes.

Typically, there are two regions of the “loop” that can be observed to follow Ohm’s law, where I ∝ V, and exhibit the Ohmic conduction mechanism described in section 2.3.6; these are when the memristor device has settled into either the high resistance state (HRS) or the low resistance state (LRS), and tends to occur in our devices at low voltage magnitudes of <1 V (this does not apply to all device geometries and material configurations).

In the non-linear regions, several observations can be made, depending on which switching mechanisms are most dominant. A sharp switch from LRS to HRS (or vice versa) typically occurs where a filament is formed or ruptured [*170*]. Other mechanisms can be investigated through analysis of the non-linear region: a plot of ln(*I*) vs $\sqrt{V}$ would indicate whether the non-linear region is consistent with Schottky emission, as a linear relationship between the two is expected; similarly, a linear relationship between ln(*I*/*V*) vs $\sqrt{V}$ would indicate that the Poole-Frenkel effect may be present [*97*]. In addition, by plotting *I* vs *V* on a logarithmic scale along the axes, SCLC regimes can be identified if present, as well as Ohmic conduction regimes.

I-V characteristics were measured using a Keysight HP Agilent 4140B pA meter/DC voltage source. This is used to apply a voltage to the samples from the V Output terminal, and to measure the current using the I Input terminal. The pA meter can

measure currents with a 10^{-15} A maximum resolution with a basic accuracy of 0.5% over wide measurement ranges.

4.3.2 Data Retention

Data retention measurements are also carried out using the Keysight HP Agilent 4140B pA meter/DC voltage source. To carry out retention measurements, the device must be put into either the “ON” state or the “OFF” state, by applying a voltage large enough to initiate the switch. This can either be achieved by a short pulse (for example, a 0.1 s pules of +3 V to switch to the “ON” state, or -3 V to switch “OFF”), or by carrying out a “single staircase” I-V sweep (i.e. the voltage may sweep from -3 V to +3 V to enter the “ON” state, but the reverse is not applied). Following this, a small voltage, referred to as a “READ” voltage, is applied for a long duration, and the current is plotted against time (*I* vs. *t*, referred to in this document as a “retention plot”), to analyse whether or not the state decays.

The device then needs to be switched to the opposite state (if the initial pulse put the device into the “ON” state, then you must apply a voltage pulse to switch it into the “OFF” state), so that both states are analysed. This can give insight as to what is occurring in the system; a decay in the state (observed in the retention plot as a gradual change in the current with increasing time, back towards its initial reading from before the voltage pulse was applied) could be caused by a range of effects, and if one state does not decay while the other does, this could have significant meaning.

Ideal memristor devices have an indefinite retention time; neither the “ON” nor the “OFF” state should decay, so that the device is able to store data indefinitely without an external power supply. As mentioned in chapter 2, current memristor technologies can have retention times in years, but oxide-based memristors are not renowned for having reliable retention times, with some reasons cited as being due to the difficulty in controlling or regulating the amount of oxygen in the devices [*171*]; retention failure is also more common at elevated temperatures (those above 100°C), cited as being a result of oxygen vacancies inside filaments being spontaneously diffused away via thermally-activated processes [*67*].

Chapter 5

Nanorod Growth – Results

In this chapter, the results of our study into the growth of the zinc oxide nanorod layer are reported. Section 5.1 investigates the initial seed layer produced under different conditions, as detailed in Chapter 2 section 2.1.2. AFM images show the profile of the silicon substrate used, and the seed layer produced by the spin-coating method. Nanorods were grown on both glass and silicon substrates, and it was found that seed-assisted nanorod growth is independent of substrate material, which agrees with literature findings [*165*, *172*].

Section 5.2 reports the results of the microwave growth investigation. Low power heating (using 100 W microwave power with a longer duration for ramping to temperature) and high-power heating (1600 W microwave power with a shorter duration of ramping to temperature) are compared. In addition, partial growth of the nanorods is investigated using SEM, showing the gradual formation of nanorods and also larger crystallites.

Section 5.3 shows x-ray diffraction (XRD) crystallography of nanorods and large crystallites.

5.1 Investigating the Role of the Seed Layer

The seed layer is used to control the growth of zinc oxide nanorods. Seeds act as nucleation sites for the growth of nanorods; the morphology of the seed layer can have a considerable impact on the growth of the nanorods, affecting the alignment, diameter and crystallinity of the nanorods themselves. As such, a good quality seed layer is important for producing a well-aligned and uniform nanorod layer.

To produce high quality ZnO nanorod structures, a seed layer is required as a foundation. Using the procedure laid out in Chapter 2 section 2.1.2, a seed layer of ZnO nanoparticles were rapidly produced.

Ideally an atomically flat substrate should be used when trying to obtain a good AFM image of the seed layer; the Si wafer is found to have an average surface roughness of ~0.33 nm, which agrees with the specifications from Ted Pella Inc. who supplied the substrate. While using Si wafers improves the quality of the seed layer by providing a uniform surface to reduce potential nucleation sites for undesired crystallite formation, such a substrate is less cost-effective than glass slides.

Figure 5.1, below, shows AFM images of a clean silicon wafer cutting as a control, and figure 5.2 shows a seed layer produced by the spin coating method described in section 2.1.2, with three coats at 2000 rpm and an anneal at 350°C after each coat.

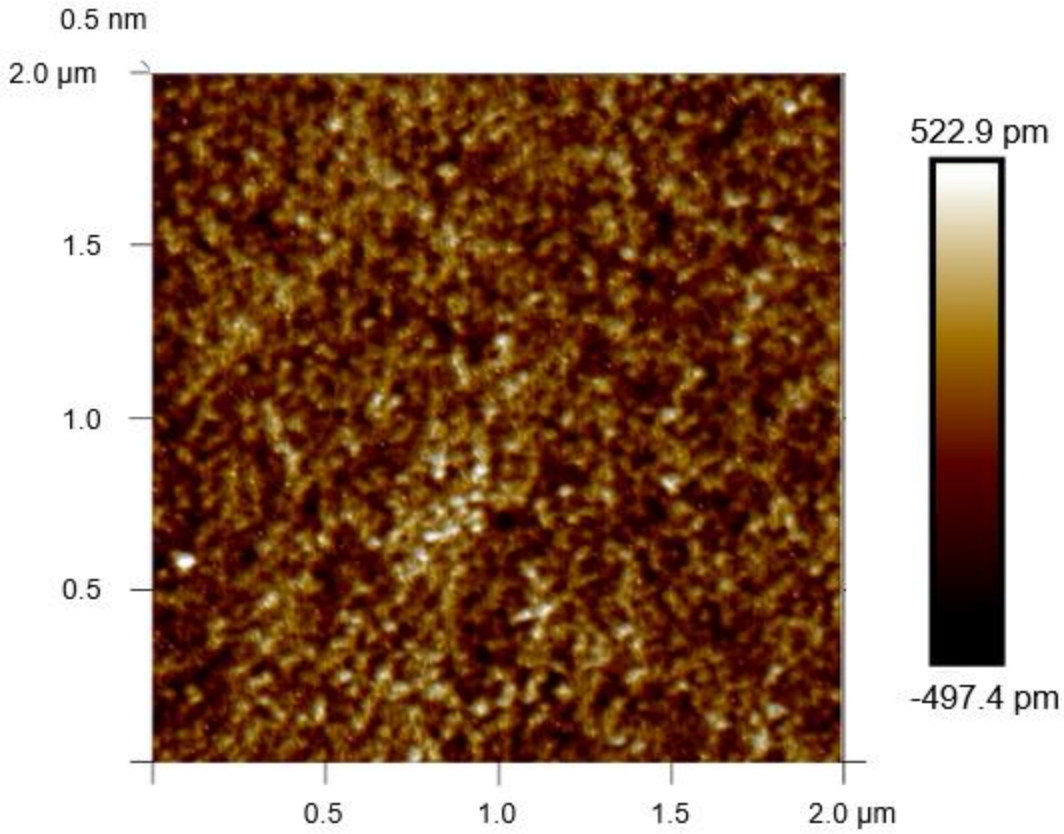

Figure 5.1: AFM image showing unseeded silicon substrate, taken over a 2 µm x 2 µm scanning area at 0.5 Hz with 256 lines per scan. Maximum particle heights are ~1 nm, and average particle height is ~0.33 nm. This agrees with the specifications sent by the supplier, Ted Pella Inc, who suggest a typical surface roughness of ~3 Å (or ~0.3 nm).

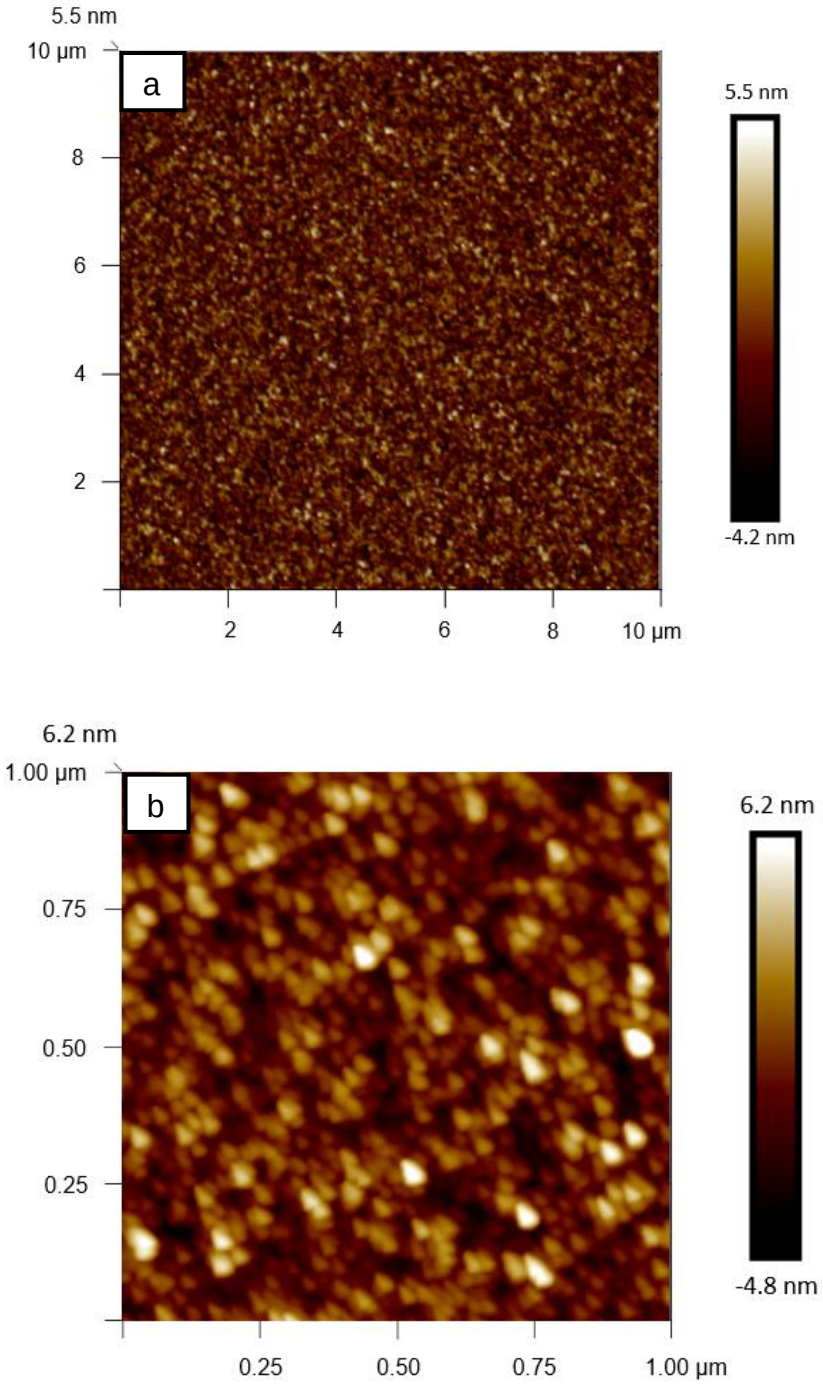

Fig. 5.2: AFM images showing seeded silicon substrate, coated and annealed at 350°C three times: a) scanned over a 10 µm x 10 µm area at 0.5 Hz with 512 lines per scan; b) scanned over a 1 µm x 1 µm area with other conditions as above. Mean particle heights are ~4.15 nm, with maximum particle heights being ~7.80 nm. Average diameter of seeds is ~50 nm, with a 16 nm standard deviation.

The above figure 5.2 demonstrates that a layer produced by spin coating three times with the seed solution, described in Chapter 4, annealed at 350°C after each spin coat, provides a uniform layer of seeds. Annealing is a heat treatment that alters the physical (and, in some cases, chemical) properties of a material; in this case, annealing is important for decomposing the zinc salt, zinc acetate dihydrate, to form a layer of ZnO seeds [*34*, *165*].

Seeds produced via the spin coating method we have used are small, with diameters of ~50 nm (calculated using the Particle Analysis function in Bruker's NanoScope Analysis software, analysing the AFM images in figure 5.2), and have heights of only a few nm. This is consistent with results from Greene et al [*165*], who observed that their seeds were unresolvable at the base of the nanorods due to their small size, and that they instead used STM and TEM techniques to analyse the seed layer.

It is observed that three coats are sufficient to produce a uniform layer of densely packed seeds.

5.1.1 The Effect of Altering Annealing Temperature

Different annealing temperatures can also affect the formation of the seed layer. Annealing the sample improves ZnO particle adhesion to the substrate [*164*], as well as decomposing the zinc acetate to form the ZnO seeds; Greene et al. found that annealing also vertically aligns the seed layer, with higher temperatures improving the crystallinity of the seeds and nanorods grown from them (150°C is required for aligning the seeds, and 350°C or higher improves the seed crystallinity) [*165*].

Figures 5.3 and 5.4 show the effect of annealing the seed layer at different temperatures (5.3 has no annealing, and 5.4 was annealed at 150°C). These figures indicate that lower annealing temperatures do not produce a seed layer of the same uniformity or crystallinity; not annealing the seeds at all produces a very poor seed layer that appears to have several gaps, and low annealing temperatures produce seeds that have a larger standard deviation from the mean diameter size. This is likely to be because the seeds are not fully decomposed to form ZnO; the material initially dissolved in the seed solution is zinc acetate dihydrate, which is dissolved in propan-1-ol. As such, due to the lack of annealing, the deposited material is still soluble and is likely to re-dissolve as the next coat is added. This, combined with the fact that the zinc acetate is not properly decomposed and has both poor alignment and crystallinity, would result in a poor seed layer that does not produce well-aligned nanorod structures.

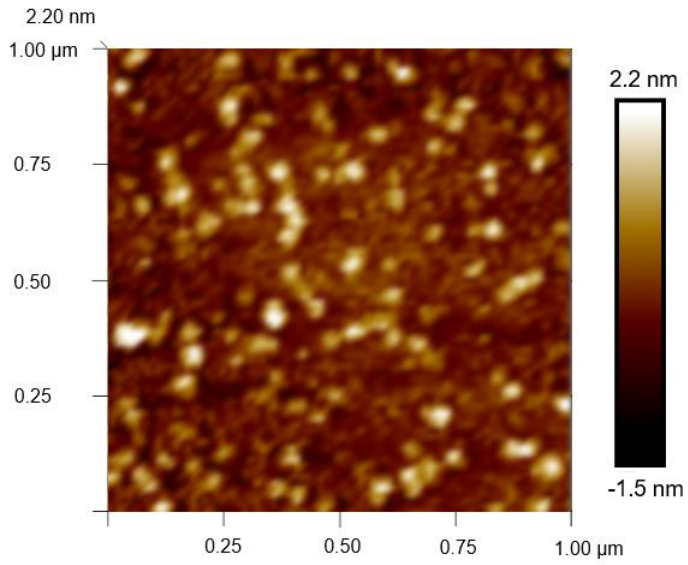

Fig. 5.3: AFM image showing seed layer that has not been annealed. The seed layer was produced by coating 3 times at 2000 rpm for 30 s but without annealing the substrate. Mean particle heights are ~2.68 nm, with some rare particle heights reaching ~10 nm. Mean particle diameters are ~60 nm, with a standard deviation of 26.6 nm. Image is zoomed to a 1 μm^2 area to show particle sizes more clearly.

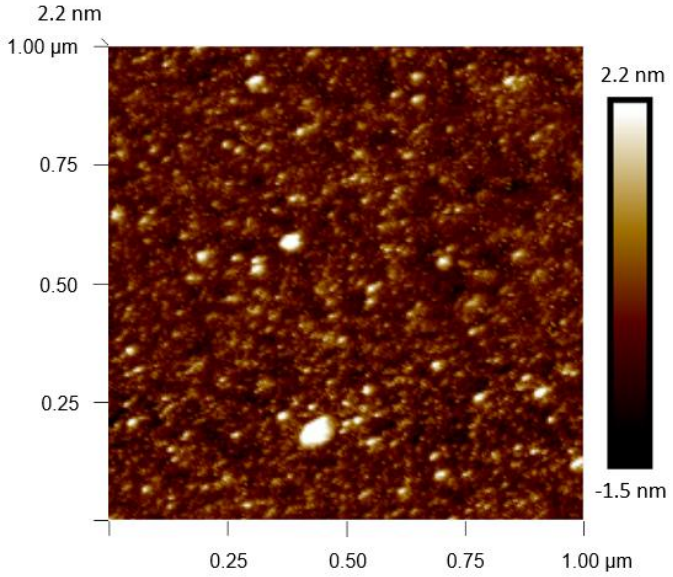

Fig. 5.4: AFM image showing seed layer that was produced by coating 3 times at 2000 rpm for 30 s following each coat with a 30 minute anneal at 150°C. Mean particle heights are ~2 nm, with some rare particle heights reaching ~6 nm. Particles have a mean

diameter of 76.6 nm, with a standard deviation of 36.5 nm. The large standard deviation is a result of the low annealing temperature.

5.2 Growth of Nanorods via Microwave Stimulation

Using the method laid out in chapter 2.1.2, ZnO nanorods were grown via microwave stimulation of the growth solution. The results of the microwave growth depend on several factors, including the quality of the deposited seed layer and the speed of heating, as well as the microwave output power selected for heating the growth solution.

Figure 5.5 shows the results of microwave heating on a glass substrate with no seed layer. Nanorods are not seen to have formed; instead, the surface of the substrate is dominated by non-uniform ZnO crystallites of various aspect ratios and sizes ranging from ~50 nm to ~600 nm. These crystallites have poor alignment (i.e. they are not aligned vertically, there is no uniform directionality to their growth) and are not uniformly distributed across the surface of the substrate, with large gaps between crystallites and no continuous film.

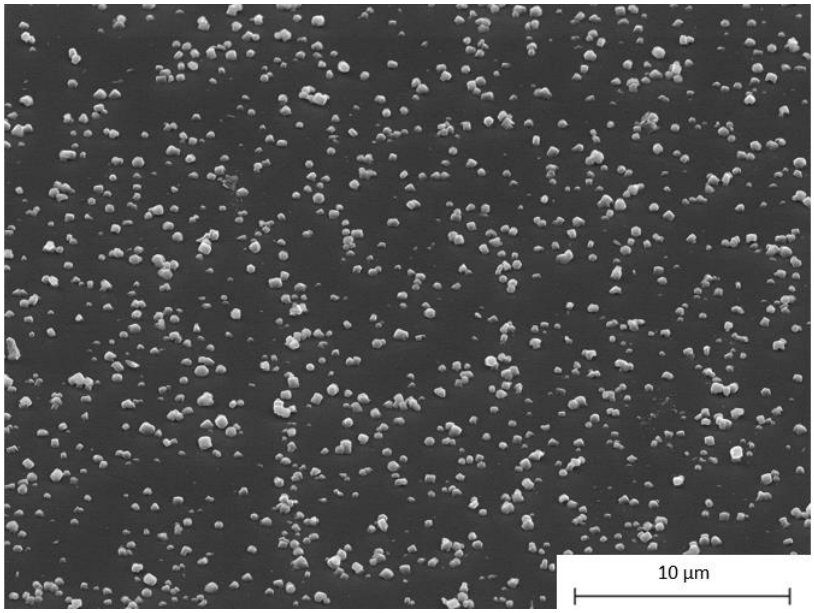

Figure 5.5: SEM image of crystallites grown on a glass substrate without a seed layer. Sample was heated to 80°C in 10 minutes with 100 W microwave output power and was held at this temperature for 10 minutes.

Figures 5.6 – 5.10 show the growth of nanorods on seed layers annealed at different temperatures. For each figure, the main image is taken at a magnification of 10,000 times; the insets featured with each figure are magnified by 120,000 times. Figure 5.6 shows nanorods grown onto a seed layer that was not annealed after each spin coat. The nanorods are primarily aligned vertically, although gaps appear between the nanorods, and still many nanorods deviate from the vertical in their alignment. In addition, large amorphous particles have settled on the sample that are not easy to remove.

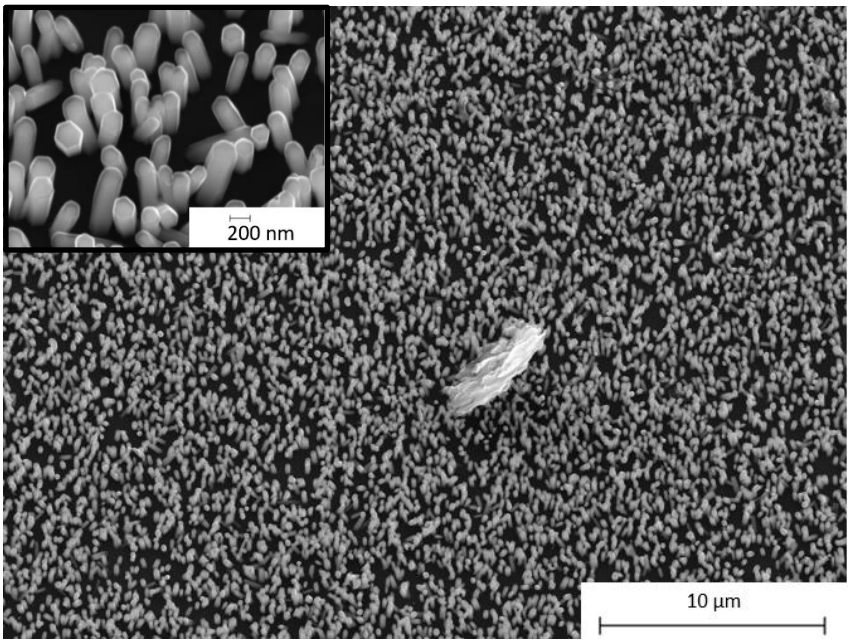

Fig. 5.6: An SEM image showing the growth of nanorods on a seed layer produced by spin coating the substrate 3 times with no annealing step. Nanorods are observed to have hexagonal topography, as can be seen most clearly in the inset image.

The addition of a seed layer immediately results in nanorod formation, but as seen in figure 5.6, seeds that have not been annealed at all will produce poorly-aligned nanorods that are not densely or homogeneously distributed across the surface of the substrate.

Figure 5.7 shows SEM of nanorods grown on a seed layer that had been annealed at only 50°C after each spin coat. We see few differences between the sample with no annealing of the seeds, and the sample with a 50°C anneal.

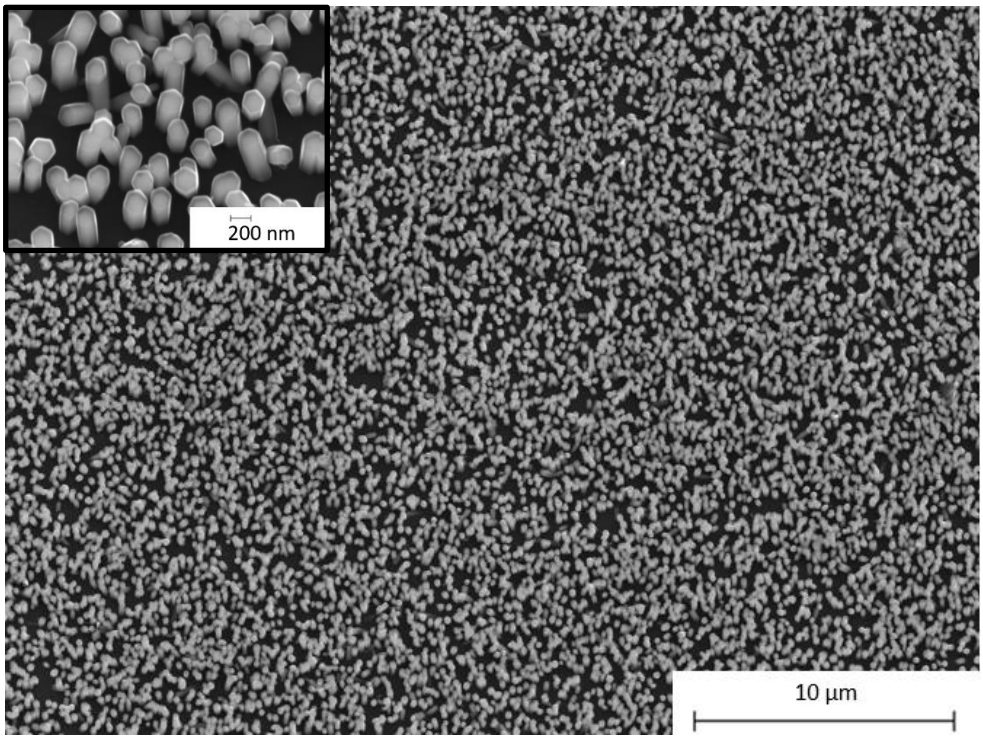

Fig. 5.7: An SEM image showing nanorods grown from a seed layer that was annealed at 50°C. While larger crystallite particles were much sparser, the gaps between nanorods and the weak alignment can still be observed.

Figure 5.7 indicates that annealing at only 50°C will also produce a nanorod layer with poor alignment. It should be noted that, as zinc acetate dihydrate has been used, rather than pure zinc acetate, there may be a lot of water present in the material; at only 50°C, this water will not necessarily have been evaporated, and this may affect the growth of the nanorods as well. 50°C may also simply not be a high enough annealing temperature to properly align the seeds. Nanorods formed on both this sample and the sample from figure 5.6 tend to be packed into densities of only approximately 10 nanorods per square µm.

Figure 5.8 shows SEM of nanorods grown from a seed layer annealed at 150°C. At this temperature, the nanorods become very densely packed and well aligned.

Large particles do appear on the surface, but typically appear to have settled on the nanorods.

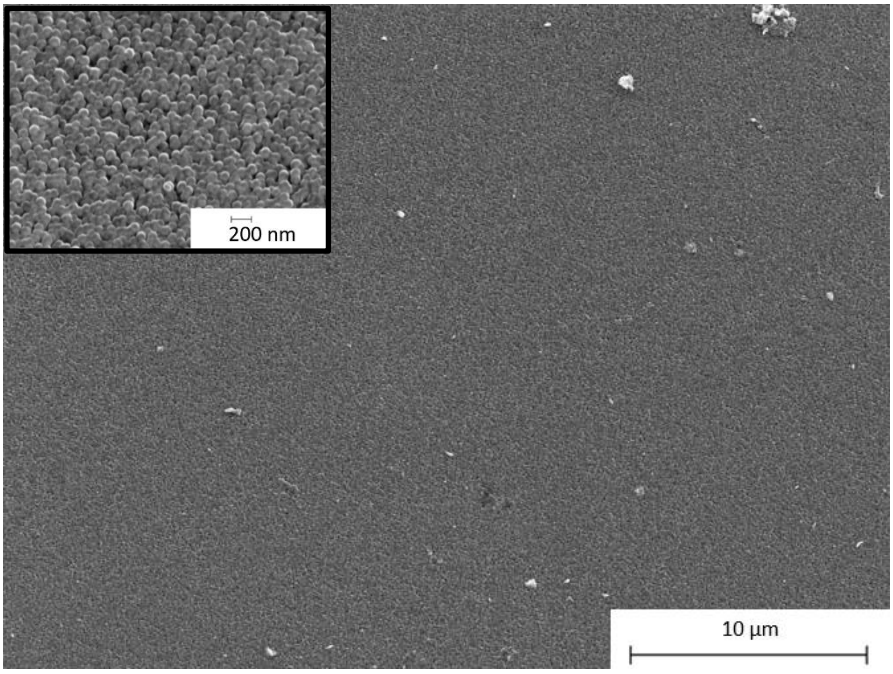

Fig. 5.8: An SEM image of nanorods grown on a seed layer annealed at 150°C.

Figure 5.8 shows that, by annealing at 150°C, a homogeneous nanorod layer can be produced. Nanorods are now densely arranged and well-aligned. Figures 5.9 and 5.10 show that further increases of annealing temperature up to 350°C continue to produce well-aligned and crystallized nanorods.

Figure 5.9 shows an SEM image of nanorods grown on a seed layer annealed at 250°C. There is little difference between the images in figures 5.8 and 5.9; the nanorods seem to be well aligned, and crystallites or amorphous particles seem more likely to settle on the surface of the sample.

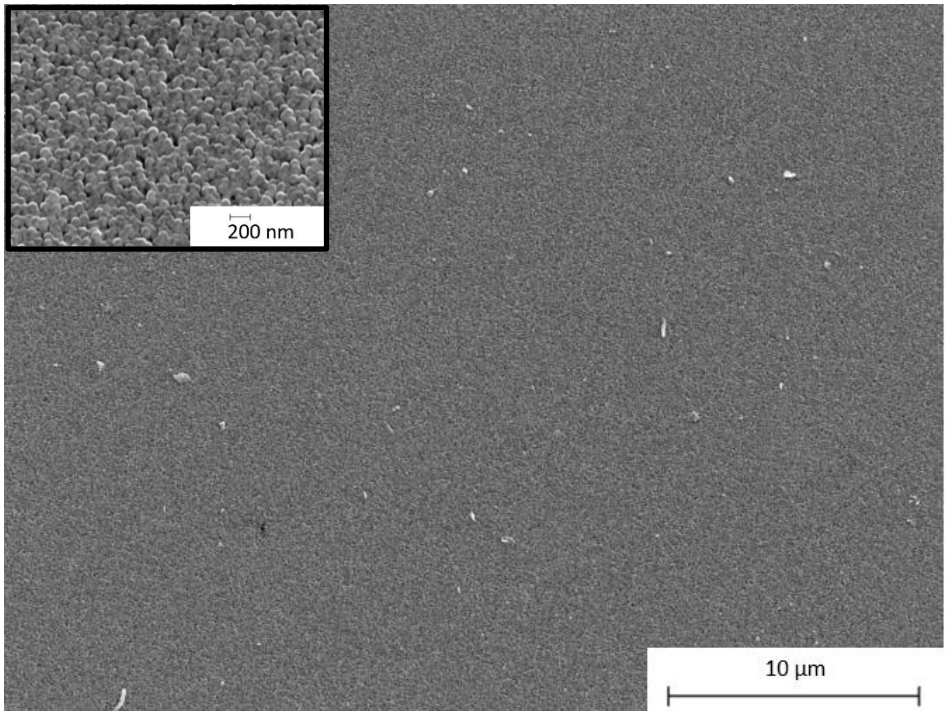

Fig. 5.9: An SEM image of nanorods grown from a seed layer annealed at 250°C.

Figure 5.10 shows nanorods grown from a seed layer that had been annealed at 350°C. This is the typical temperature used for annealing, as it is known to be able to improve crystallinity and alignment compared to other annealing temperatures [*162*]. From these results, however, very little difference can be observed for the sample annealed at 350°C compared with the 150°C and 250°C anneals.

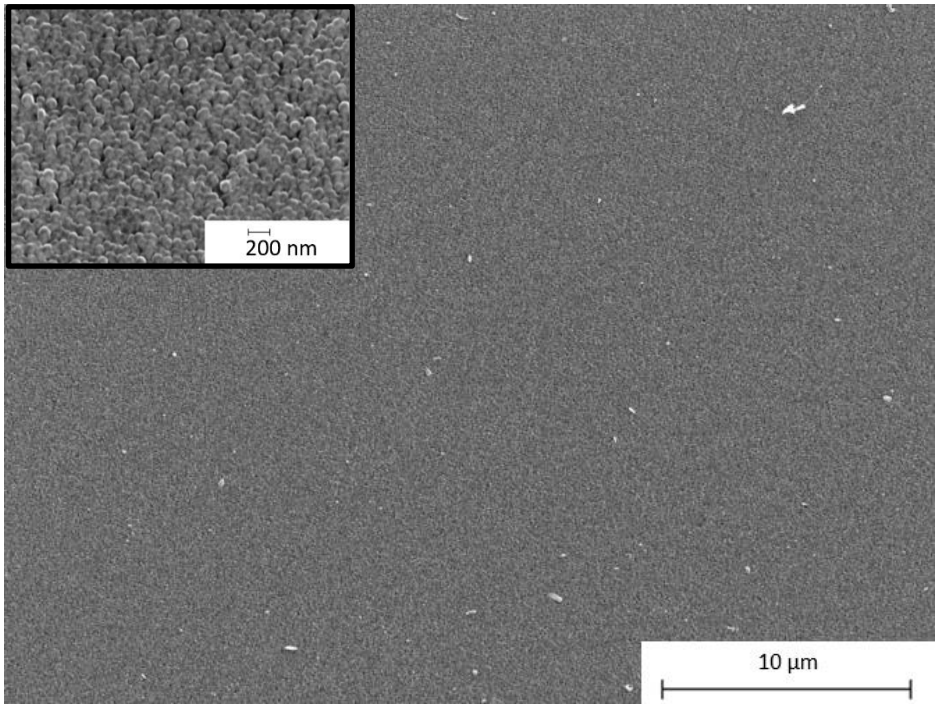

Fig. 5.10: An SEM image of nanorods grown from a seed layer annealed at 350°C.

The result of this investigation is that it is clear that annealing the seed layer is a vital step that has a great influence on the structure, alignment and morphology of the nanorods. It is noted that all nanorods produced (even at low annealing temperatures) appear to exhibit the hexagonal topography, as seen in the above SEM images, that is indicative of a wurtzite structure (this is confirmed by our XRD in section 5.3); the main differences appear to be alignment, density, and nanorod diameter (between the nanorods with annealing at 50°C or less, and those with annealing at 150°C or above; the former produce unaligned nanorods with diameters of ~ 200 nm, while the latter produced nanorod diameters of > 100 nm). The densities of nanorod packing on these samples are greater than 100 nanorods per square µm, more than ten times as densely packed as the samples annealed at 50°C or less. This seems to agree with observations by Greene et al. [*165*], who found that annealing temperatures below 100°C cause seeding to fail, because the zinc acetate

does not decompose to form ZnO and instead can dissolve into the nanorod growth bath.

5.2.1 The Effect of Altering the Rate of Heating

As mentioned previously, the rate of heating is an important factor in determining the quality of the nanorods grown via microwave heating.

Figure 5.11 shows the effect of altering the microwave power used to ramp to temperature. In both cases, the solution was heated to 80°C and then held for 20 minutes at that temperature. However, as a condition of altering the ramping power, the duration of heating required to reach the desired temperature was also altered.

As can be seen in figure 5.11, a longer ramping time at lower microwave power produces fewer large crystallites than a more rapid heating at high power.

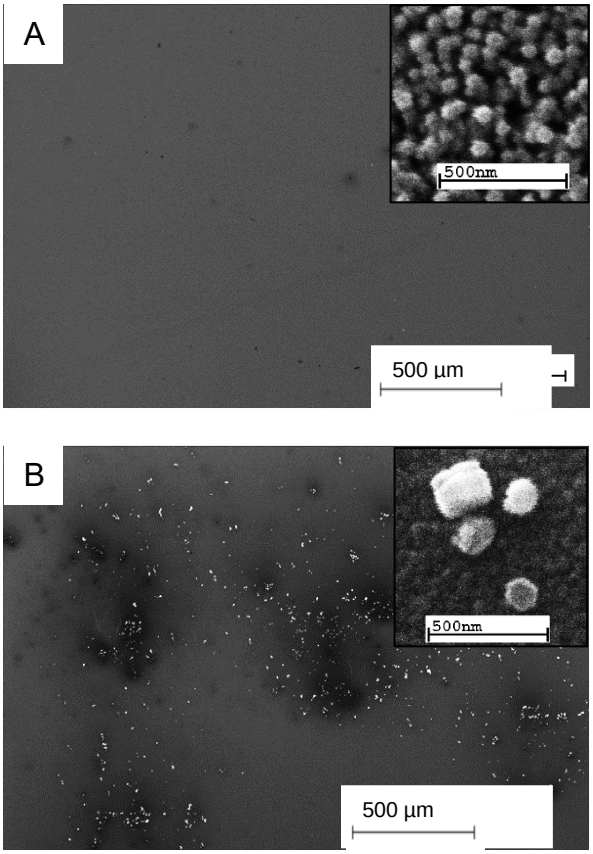

Figure 5.11: SEM images of nanorods grown with different ramping times and with different microwave power. (A) was heated to 80°C in 30 minutes at 100 W; (B) was heated to 80°C in 5 minutes with a microwave power of 1600 W.

The rate of temperature increase (controlled in the Mars 5 microwave by altering the microwave power and the duration of the temperature ramping process) affects the amount of larger, undesirable crystallites formed and deposited on the sample surface. These are typically very difficult to remove post-growth, and thus careful control of the rate of heating is necessary. Figure 5.12 shows the average number of large, undesirable crystallites per square mm area measured on four samples grown at 1600 W and four grown at 100 W.

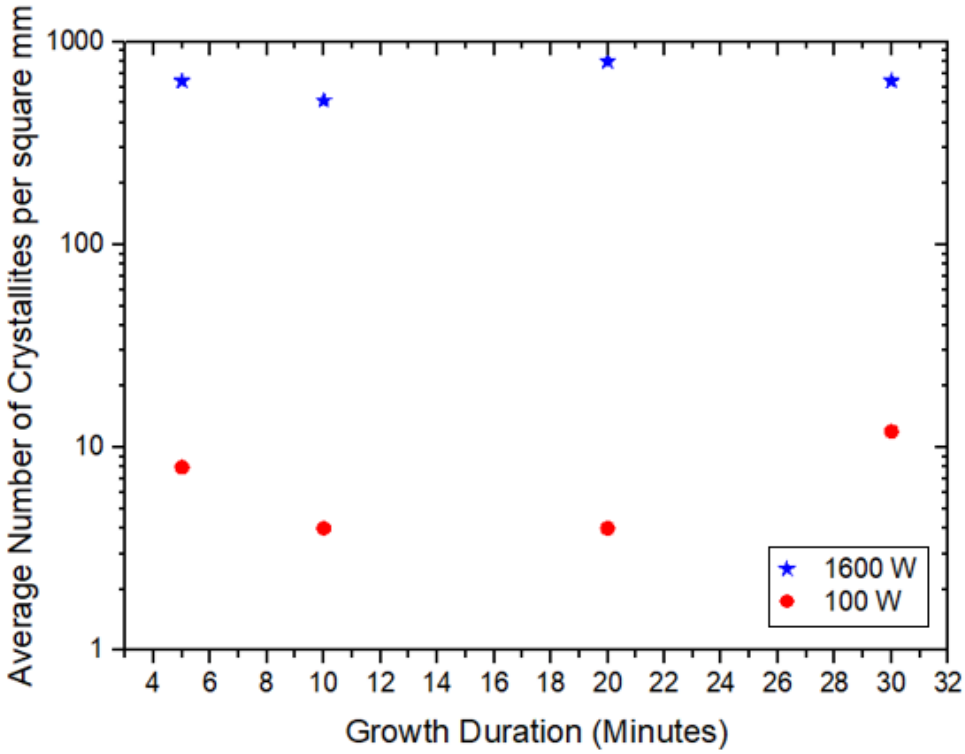

Fig. 5.12: A graph of the average number of crystallites per square mm measured from four samples grown at 1600 W and grown at 100 W. The ramping durations are as above, 5 minutes for the 1600 W samples and 30 minutes at 100 W. After the ramp stage the samples were then held at 80°C for different durations of 5, 10, 20 and 30 minutes respectively. As can be seen in this graph the number of crystallites formed is independent on the growth duration indicating that crystallite formation occurs in the very early stages of growth.

While using a high power ramp allows for growth of nanorods at a faster rate than the low power ramp, figures 5.11 and 5.12 demonstrate that larger crystallites are much more likely to be deposited with such a rapid ramping method. The faster ramp rate may affect the rate of reaction of the growth solution; rapid production of OH^- ions within a short period causes Zn^{2+} ions to precipitate out quickly due to the high pH environment. This minimizes the contribution of the Zn^{2+} ions to the nanorod growth and rapidly consumes the nutrient, resulting in the eventual prohibition of

further growth of the nanorods [*173*]. The use of HMTA in the growth solution contributes to maintaining a low supersaturation level by controlling the concentration of OH^- ions in the solution. It is this characteristic behaviour that appears to govern the formation and deposition of the large crystallites. It is observed that neither crystallites nor nanorods grow at very low temperatures. However, rapid temperature ramping at high power causes significantly more crystallites to be formed on substrates than slow ramping at much lower power, keeping the post-ramping duration the same in each case.

From figure 5.12 it is observed that the high power, rapid ramp method has more than 400 crystallites per mm^2, where the low power, slower ramp method produces typically fewer than 10 crystallites per mm^2. Nanorod morphologies are typically the same as for the low power ramp method, although dark, patchy regions appear throughout the surface of the substrate indicating regions of poor growth.

This difference could be the result of a ripening mechanism, such as Ostwald ripening [*174*]. Ostwald ripening is a diffusion process that occurs in the last stage of a first-order phase transformation, and is a mechanism by which matter from small particles diffuse to larger particles, causing the larger particles to grow at the expense of the smaller particles, which gradually shrink to nothing [*174*]. R. Viswantha et al [*175*] showed that the presence of a capping agent, such as HMTA, reduces the rate of growth of nanocrystals and crystallites to a rate that is less than predicted by Ostwald ripening. As mentioned in section 4.1.2 of this thesis, HMTA attaches to the non-polar facets of nanorods during growth, limiting growth except

for in the (001) vertical direction [*31*, *164*]. It is possible that a faster ramp at high power results in high supersaturation levels, as HMTA rapidly decomposes to produce OH^- ions. This would favour the early nucleation of large crystallite material, as we observe in the next section, which would then be expected to grow steadily along with nanorod growth. Our results do not conclusively prove this to be the case; further study into the rate of production of OH^- ions for each ramp method would be required to ascertain this.

5.2.2 Investigation of the Formation of Nanorods and Crystallites

Using a domestic microwave (Russell-Hobbs, RHM3002 900 W combination microwave), a rapid ramp method was used to identify at what point crystallites begin to form. Using 100% power setting (900 W) for intervals of 20 s, 40 s and 60 s, samples were heated in the growth solution in the centre of the microwave, revolving at 6 rotations per minute. Samples were later removed and analyzed under SEM.

The results are shown in figure 5.13 below. In each case, the early stages of large crystallite growth appear to be visible (these are the larger, white “dots” appearing on the samples’ surfaces). Due to the low time each sample spends in the growth solution, there is little to no nanorod growth; early signs of nanorod growth are only obvious in 5.13b and 5.13c. This is because the solution only exceeds the minimum ideal growth temperature (~70°C) at around 40 s in the commercial microwave (the 20 s sample reached only ~40°C).

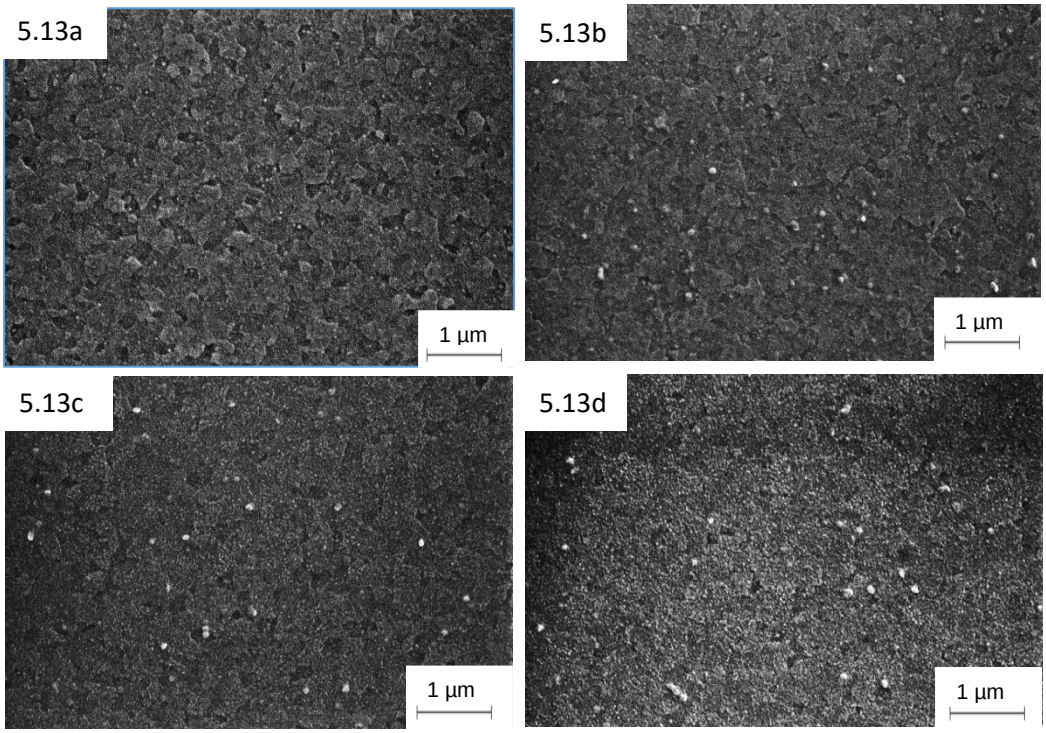

Fig. 5.13: A control sample that has received a seed layer and has been dipped into growth solution for one minute before cleaning (5.13a); compared with samples that were heated in a Russell-Hobbs RHM3002 900 W microwave at 100% power (5.13b: heated for 20 s; 5.13c: heated for 40 s; 5.13d: heated for 60 s), all at 50,000x magnification. In each case we see the background ITO in the image, with 5.13c and 5.13d showing very early stages of nanorod growth. Early stages of crystallite growth also appear as white protrusions.

Figure 5.14 shows AFM images on Si substrates demonstrating the early stages of nanorod growth. A gradual increase in nanorod length is observed, but also small, clustered groupings of brightly coloured, longer nanoparticles which seem to be early stages of large, undesirable crystallite formations.

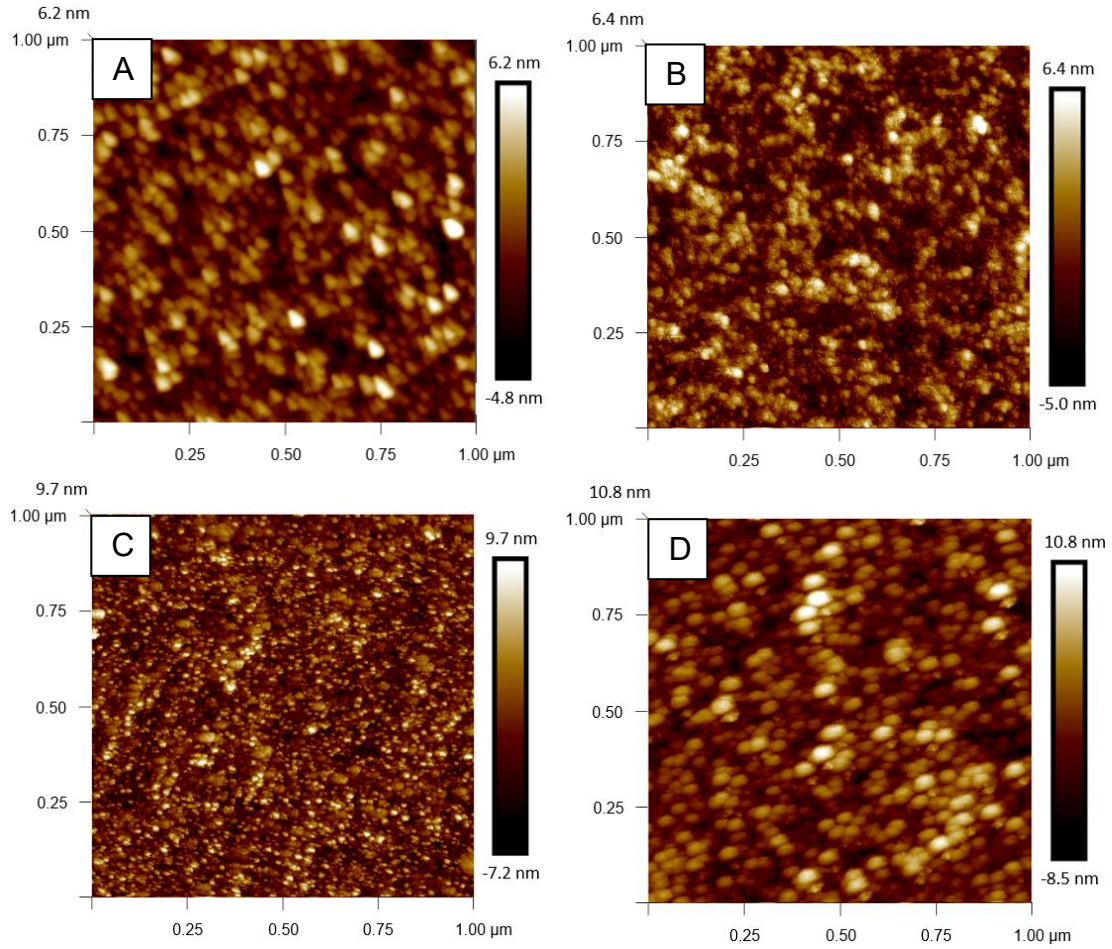

Fig. 5.14: AFM images of silicon substrates: a) substrate coated using standard seed layer procedure (3 coats, 3 anneals as explained in chapter 3; b) is a substrate that has undergone a 20 s growth process using the domestic microwave; c) has undergone a 40 s growth process using the same microwave procedure; d) has undergone a 60 s growth process using the same microwave procedure. Average particle heights in a) are ~3 nm, and b) has similar average particle heights of ~4 nm, while c) average particle heights are ~7 nm, and ~10 nm in d). The tallest particles in a) were ~4 nm, compared with 10 nm in b), 15 nm in c), and 19 nm in d).

5.3 XRD of Nanorods and Crystallites

X-ray diffraction (XRD) crystallography can be used to give much information about the structure and alignment of crystalline structures and materials in films.

Figure 5.16 shows the XRD crystallography of four different samples:

1. A sample that was coated with crystallites that had been pre-formed in a growth solution using the standard microwave heating method (spin coated onto a clean slide with no annealing);

2. A sample that was produced with a standard seed layer and at high microwave power (1600 W), in this case a rapid ramp-to-temperature growth step produced nanorods with many crystallites (so that the film was predominantly covered with crystallites);

3. A sample with a lower-power (400 W), slower ramp-to-temperature heating method (to reduce the number of crystallites while providing a good nanorod layer);

4. A final sample produced using the lowest power (100 W) with very slow ramp-to-temperature heating (to predominantly feature nanorods with no crystallites).

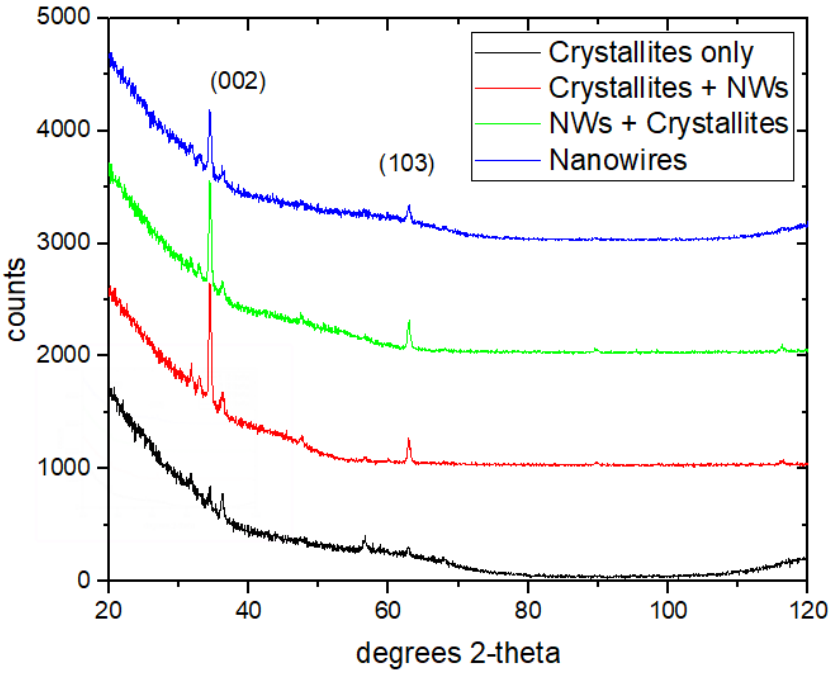

Fig. 5.15: XRD crystallography of a range of different ZnO structures produced by our microwave method: a sample with only large crystallites, produced by spin-coating large crystallites, that had been pre-formed in a growth solution using the standard microwave heating method, onto a clean glass slide with no seed layer; a sample with many crystallites that dominate the sample surface, produced by carrying out our 1600 W growth procedure with a short ramp; a sample with few crystallites and a dominant nanorod presence, produced using our complete growth procedure at lower power (400 W) with a longer ramp time; and a sample that is virtually free of large crystallites, produced using our 100 W growth procedure. The (002) peak is clear in all samples that feature nanorods, showing strong alignment in that plane.

The (002) and (103) diffraction peaks are clear in all of the curves except for the crystallites only sample. The sharp, intense (002) diffraction peak in the 2θ range for all samples with nanorods indicates that the nanorods have the wurtzite ZnO structure [*176*, *177*] and strong vertical alignment, while the (103) peak is representative of nanorod structures of ZnO [*177*]. This coincides with the visual

information from figures 5.6 – 5.10 in section 5.2, which showed SEM images of vertically-aligned nanorods with hexagonal topography.

The intensity (counts) for the crystallites-only sample is very low, and no major peaks can be seen; this could represent poor crystallinity in the structure of the ZnO material, but is most likely due to the lack of alignment of the crystallites and the sparsity of the crystallite distribution over the sample surface.

Figure 5.16 shows the XRD crystallography in terms of counts vs. degrees chi (χ, a rotation angle in the General Area Detector Diffraction System (GADDS) convention representing a left-hand rotation about a horizontal axis [*178*]), representing a one-dimensional scan. This tells us the degrees of crystallinity of the ZnO nanorods. As with figure 5.15, three of the curves look very similar: the curves representing the nanorods only, nanorods with large crystallites, and large crystallites with nanorods (the latter indicating a higher concentration of crystallites than the “nanorods with crystallites” sample).

This is because the majority of ZnO material on the surface of all of these samples is in nanorod form, and so the major peaks observed are the same, with only the overall intensity (counts) being lower with increasing concentration of large crystallites.

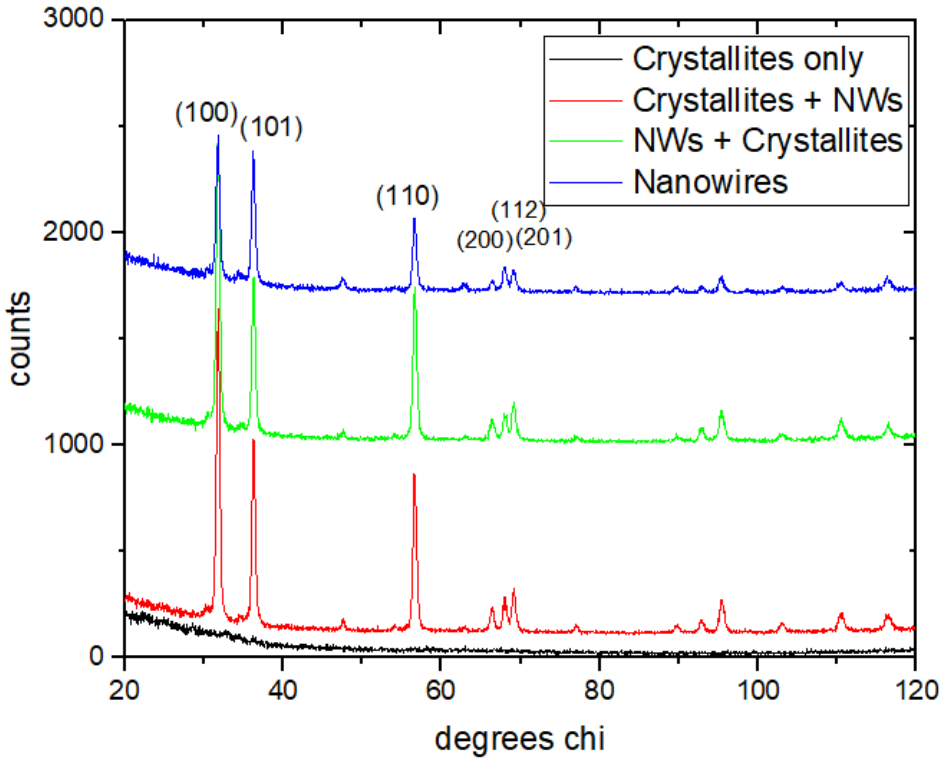

Fig: 5.16: XRD crystallography of ZnO nanorods and crystallites in different configurations on a substrate.

Figure 5.16 highlights orientations that correspond to Miller Indices representing combinations of either in-plane or out-of-plane components [*179*]. Of particular interest are the (100) and (101) peaks, both of which are well-known peaks for ZnO nanorods and indicate that the nanorods have the hexagonal morphology typical of a wurtzite blende structure, further reinforcing our conclusions from the SEM data in figures 5.6 – 5.10 and the XRD data in figure 5.15.

The crystallites-only sample does not have any notable peaks, and the count rate is very low. As with figure 5.15, this could indicate that the crystallites have reduced crystallinity as a result of not being formed with a seed layer (or that the “crystallites”

are in fact not crystalline at all, but are amorphous ZnO material – this is, however, unlikely). The most probable cause for the lack of intensity, however, is that the crystallites are both unaligned and very sparsely distributed across the substrate surface, compared with the nanorods which are densely packed, well-aligned and completely cover the sample surface. As such, there are likely too few of the large crystallites on a typical sample to give a meaningful result using this XRD method.

Chapter 6

Electrical Measurements - Results

Memristors can be identified by the observation of a “pinched hysteresis loop” in the current-voltage (I-V) plot for the device, as discussed in chapter 2. More information can be extracted from this data, however; analysing the data with respect to variations in the materials used to make the devices can give important information about the mechanisms. In addition, more detailed analysis of the hysteresis itself can unveil further information about the mechanisms that govern the resistive switching effect.

This chapter presents data from electrical measurements taken using a range of different configurations of memristor devices. I-V data is presented for metal-oxide-metal devices made using combinations of gold (Au) and aluminium (Al) electrodes, with and without the addition of a PMMA layer. I-V data is also presented for devices using ITO as a bottom electrode, with top electrodes of either Au or Al, and with or without a PMMA layer. The I-V sweeps are analysed in the non-linear region to identify the mechanisms that are likely responsible for the resistive switching behaviour. Further, to confirm that the ZnO is a key factor in producing the resistive switching behaviour, the results of a brief investigation into switching without the ZnO layer will also be presented.

6.1 Current-Voltage (I-V) Sweeps

As detailed in chapter 4, memristors based on ZnO were fabricated using a variety of different electrode materials. Metal electrodes were deposited via thermal evaporation under vacuum (~4 x 10^{-7} mbar) as detailed in section 4.1.1. In cases where ITO was used as a bottom electrode, pre-coated float glass slides (polished) were used that had been purchased from Delta Technologies, Ltd. The bottom electrodes were then coated with a layer of ZnO nanorods via the method described in section 4.1.2. A metal top electrode was then deposited, again using the method described in 4.1.1.

For some device batches, a layer of PMMA was spin-coated onto the sample after the nanorod layer was deposited, using the procedure laid out in section 4.1.3, followed by the deposition of the top electrode as above. Without the PMMA layer, the metal top electrode may disperse into the nanorods; this can cause some devices to fail, as the top electrode short circuits with the bottom electrode and no hysteresis occurs.

Simple I-V characteristics were taken for devices from each batch of samples at room temperature and plotted using Origin software. The V Output probe from the HP 4140 B pA meter was placed in contact with the bottom electrode unless specified, and sweeps were applied from negative voltage to positive voltage, and then from positive back to negative, in a double-staircase voltammetry configuration.

6.1.1 Investigation of the Impact of Using Different Electrodes

Figure 6.1 shows the memristance characteristics for a single device with Au bottom and top electrodes (no PMMA), of 100 µm x 100 µm device active surface area, and with ZnO nanorods as the memristive material.

Hysteresis is very small, showing a difference in the absolute current (the current magnitude) of less than one order of magnitude between the two resistance states. This may be a result of diffusion of Au into the ZnO at the interface, creating Zn vacancies in the material that are responsible for changing the Schottky barrier [*47*, *180*].

The sweeps can be seen to be slightly asymmetric, although the electrical behaviour on both the positive and negative sides of the sweep seems to be consistent at this stage in the switching (up to sweeps between -3.5 V and +3.5 V). While the switching magnitude does seem to increase slightly as the magnitude of the sweeping voltage increases, it is not by a significant amount. The asymmetry in the hysteresis between the positive and negative voltage regions may be attributed to a migration of ions/defects at the interface between the metal electrode and the semiconductor material [*50*, *181*], or the diffusion of Au into the ZnO nanorods as described above; this would affect the Schottky barrier height.

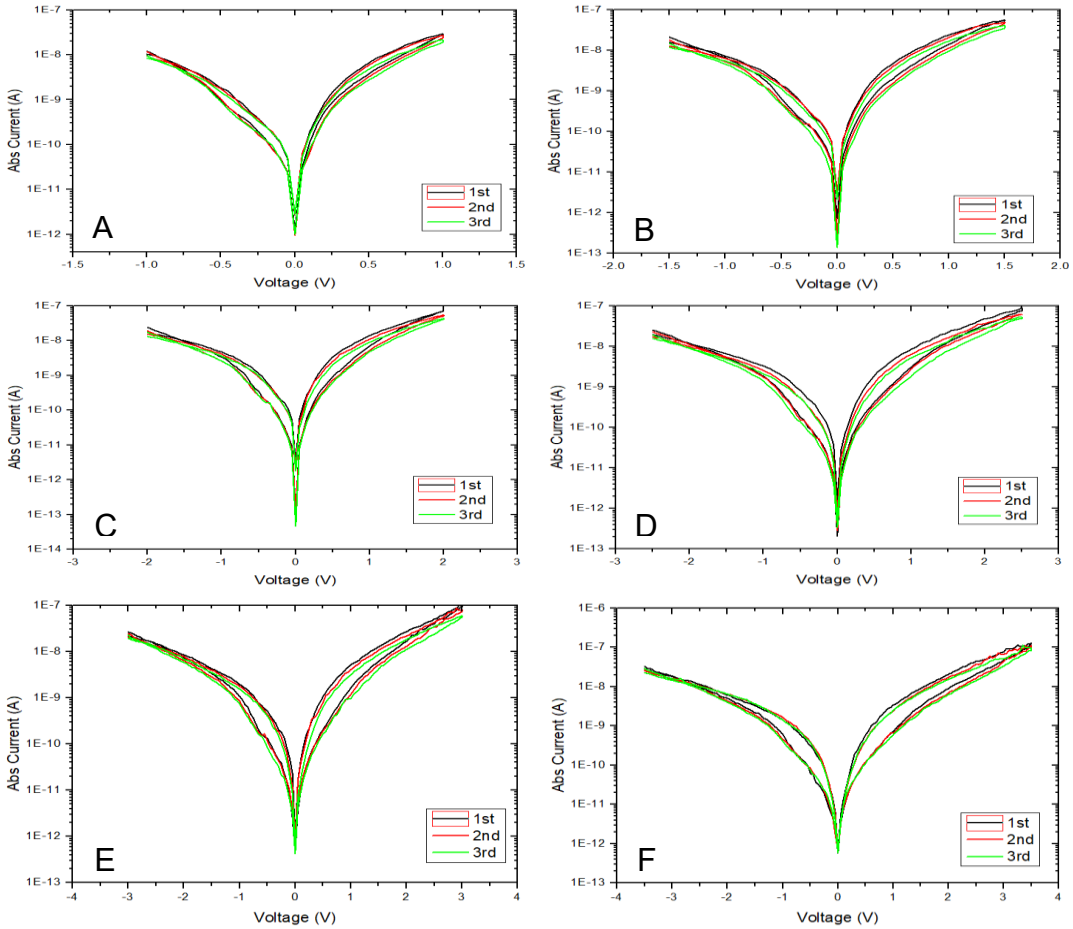

Fig. 6.1: I-V characteristics of a single memristor device with an Au/ZnO/Au configuration and showing greater resistance on/off ratios with sweeps to larger voltage. Sweeps were carried out between: A) -1 V and +1 V; B) -1.5 V and +1.5 V; C) -2 V and +2 V; D) -2.5 V and +2.5 V; E) -3 V and +3 V; and F) -3.5 V and +3.5 V. The graph indicates that memristive behavious occurs at the lower voltages, and the resistance on/off ratio slightly increases as the voltage increases.

It is notable that the device did not require a forming step; this is also true of all the devices tested in this project and appears to be a general case for this configuration with ZnO. This is likely due to defects in the ZnO material that are likely to have been formed during the microwave-assisted growth process, as rapid hydrothermal growth methods are known to produce large quantities of defects in ZnO nanorods

[*182*]. This is not a unique feature of ZnO-based memristors but seems to be reasonably common in oxide-based memristors, including TiO_2 [*183–186*].

Figure 6.2 shows the hysteresis behaviour of the same device as the applied voltage is increased beyond magnitudes of 3.5 V. At 4 V magnitude, the device still seems to function reasonably at positive voltages but are not consistent at negative voltages. Additional current paths begin to be derived at 4.5 V magnitudes.

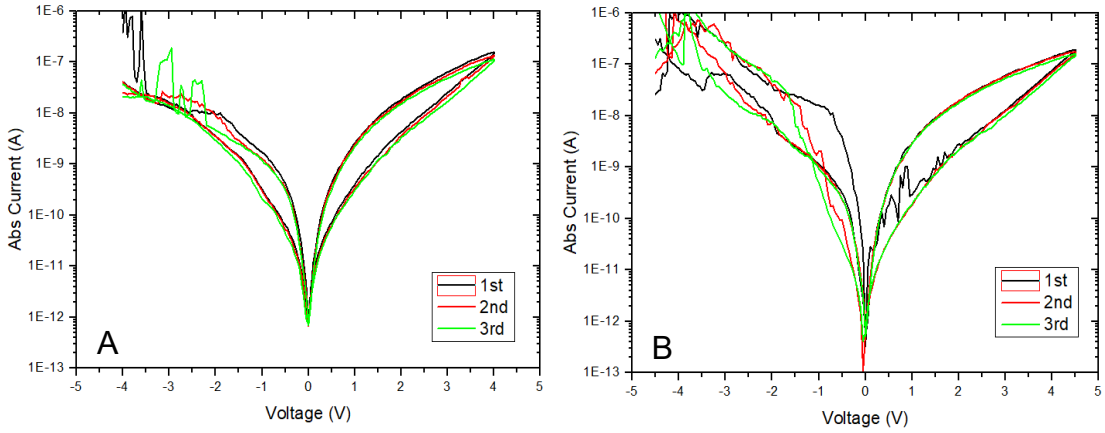

Fig. 6.2: I-V characteristics for the same Au/ZnO/Au device as characterized in figure 6.1. Sweeps were carried out between: A) -4 V and +4 V; and B) -4.5 V and +4 V.

Figure 6.3 shows the I-V characteristics of the device after additional current paths have been derived. From this point, the switching is no longer reliable or reproducible.

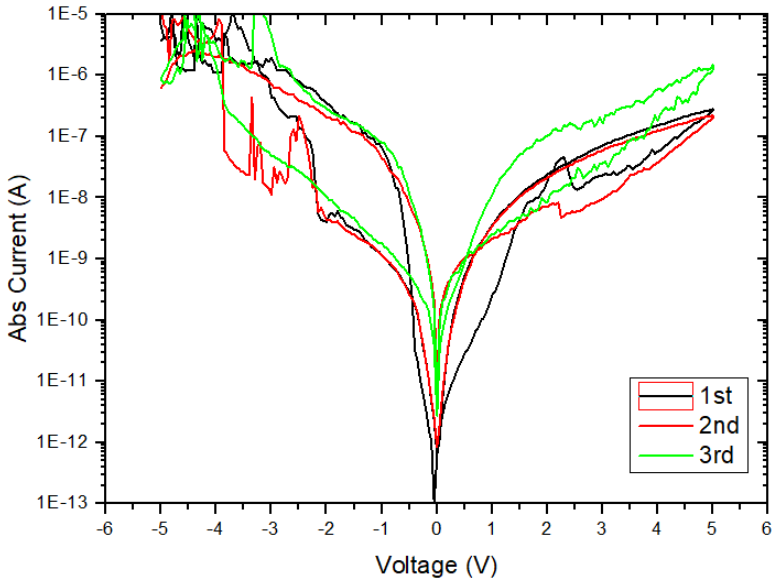

Fig. 6.3: I-V characteristics of the Au/ZnO/Au device, showing sweeps between -5 V and +5 V. The device no longer behaves consistently.

Figure 6.4 shows I-V comparisons between the device from the previous figures, and a second device on the same sample, this time of 400 µm x 400 µm device active surface area. At low voltages, the two devices exhibit similar behaviour. However, the 400 µm x 400 µm device exhibits more symmetrical switching at low voltages (<2 V magnitude), and additional current paths are derived at a lower voltage (~3V magnitude) This may indicate a dependence on device area, which would rule out electrochemical migration (filament formation), which is an area-independent mechanism.

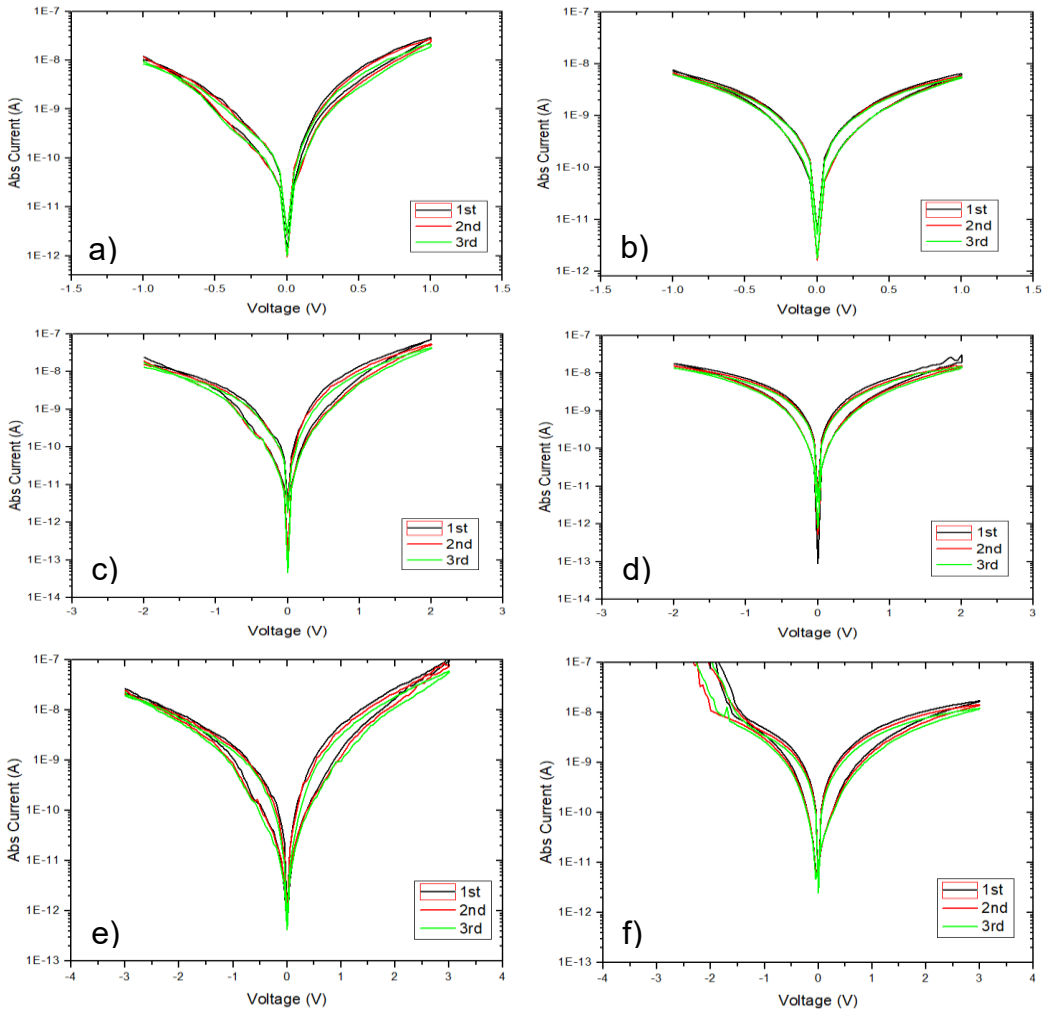

Fig. 6.4: Side-by-side I-V characteristics of two Au/ZnO/Au devices from the same sample. Images a, c, and e, are all from the initial 100 µm x 100 µm device as detailed in figures 6.1 – 6.3, at voltage magnitudes of 1 V, 2 V and 3 V; b, d, and f, are all from a second, 400 µm x 400 µm device on the same sample.

Figure 6.5 shows a comparison of devices from a different sample fabricated in the same configuration (Au/ZnO/Au, with the ZnO in the form of nanorods), with an active surface area of 100 µm x 100 µm for both devices.

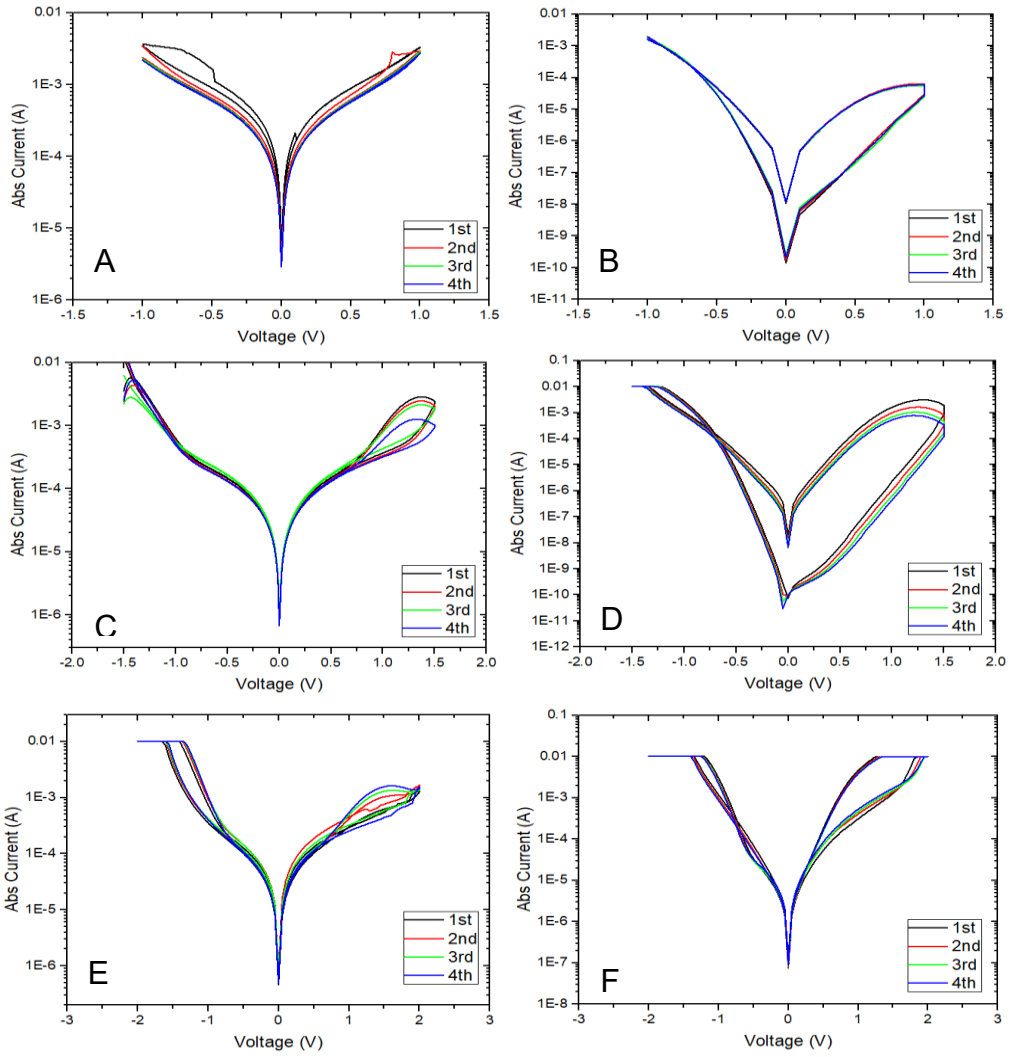

Fig. 6.5: I-V characteristics of two separate devices on a second Au/ZnO/Au sample. Images A, C, and E, show sweeps for one device at voltage magnitudes of 1 V, 1.5 V, and 2 V respectively; B, D, and F, show the corresponding switching behaviour for a second device. At around 1.5 V magnitudes (as seen in C – F), the current flowing through the device exceeds the current limit of the HP 4140 B setup.

The above figures seem to indicate that, while the configuration of Au/ZnO/Au can exhibit reasonable switching behaviour, this is not necessarily consistent from device to device, or from sample to sample.

Figure 6.6 shows an energy band for the Au/ZnO/Au configuration.

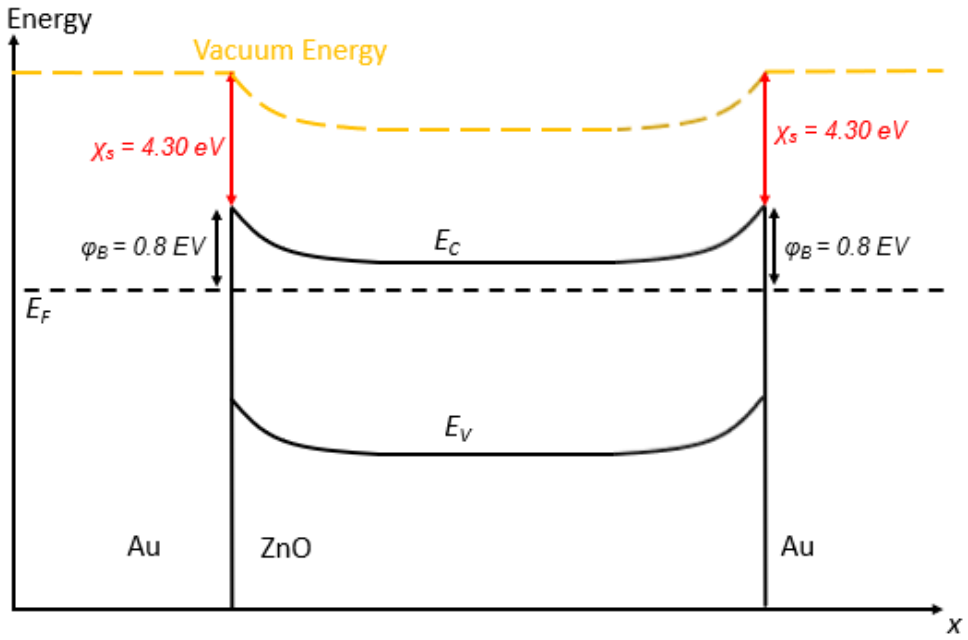

Fig. 6.6: An energy band diagram for the Au/ZnO/Au configuration. This diagram shows the barrier height, φ_B, as calculated in figure 2.7 in chapter 2, as well as the electron affinity for ZnO, χ_s.

Working device yields (the number of devices per sample that work properly) are also typically low; this could be due to short circuiting as a result of electrode material being deposited between the nanorods and contacting the bottom electrode. The working device yield varies widely between samples, often with as many as half of the devices on a sample failing to show hysteresis. Figure 6.7 shows I-V sweeps of a device with configuration Au/ZnO/Al, with a 100 µm x 100 µm device area.

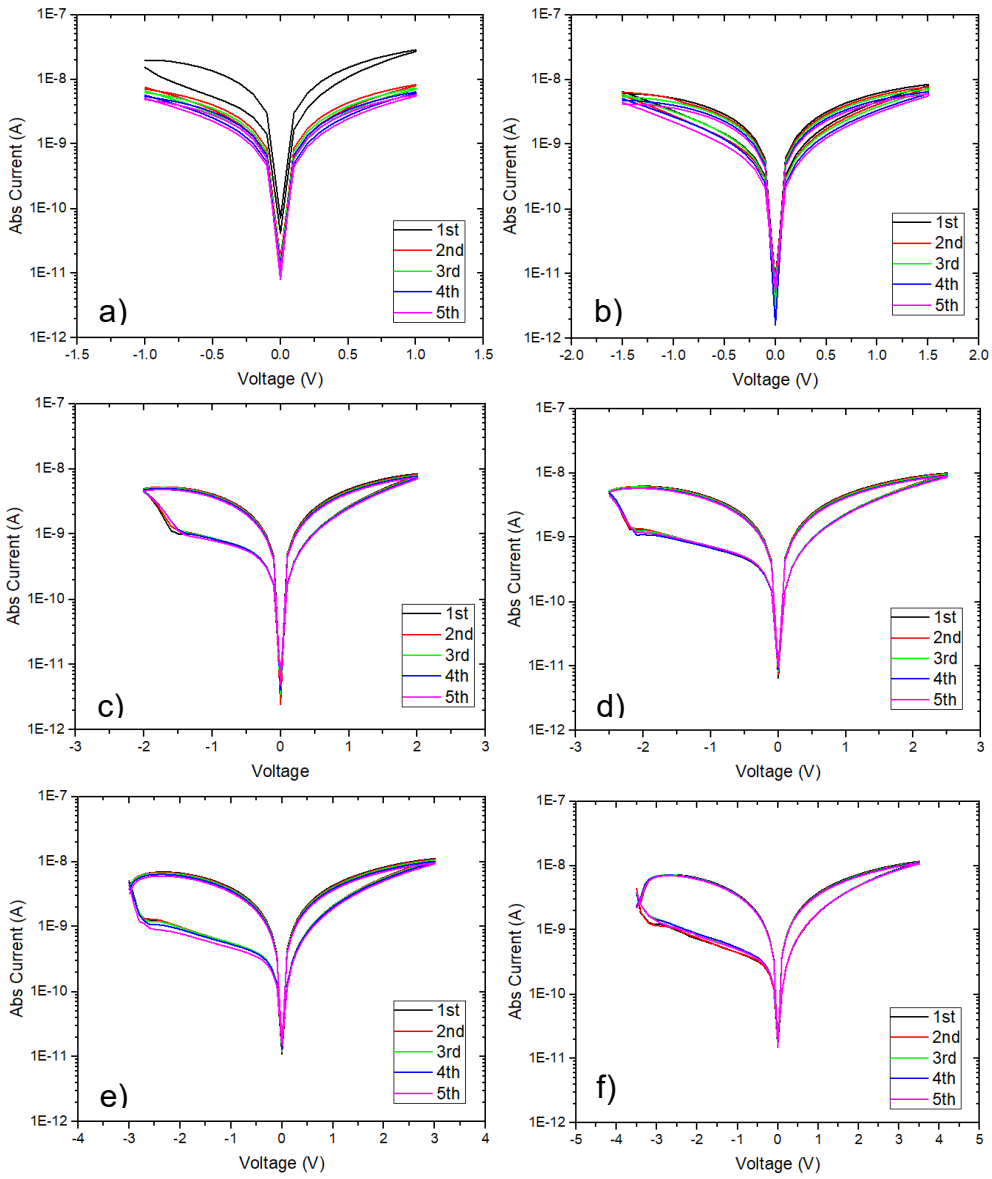

Fig. 6.7: Switching characteristics of a device with the Au/ZnO/Al configuration. Voltage sweep ranges: a) -1 V to +1 V; b) -1.5V to +1.5 V; c) -2 V to +2 V; d) -2.5 V to +2.5 V; e) -3 V to +3 V; f) -3.5 V to +3.5 V.

Switching is observed immediately at 1 V magnitude applied bias, although the first sweep is at a higher operating current. The cause for this initial sweep having a higher operating current than subsequent sweeps is unclear, as the sweep itself returns to its initial current level at -1 V on the return sweep; this typically is not the

case during a filament forming step, as the initial state before filament formation is never returned to once the device first enters the SET and RESET states. It is therefore likely that this is the result of poor probe contact from the HP 4140 B probes contacting the electrodes.

Early switching is largely symmetrical, although after applying sweeps between -2 V and +2 V, the switching becomes asymmetrical with a larger visible switching magnitude in the negative voltage region. The asymmetry can most likely be attributed to the different mechanisms occurring at the top and bottom electrodes, as a result of using Al (top) and Au (bottom). Au forms a Schottky barrier with ZnO (with a theoretical barrier height of 0.8 eV), while Al typically forms an Ohmic contact.

The V Output probe from the HP 4140 B pA meter is in contact with the Au electrode, and sweeps from negative to positive voltages and then back to negative voltages are applied (this is using “conventional current” terminology [*187*]; as electrons flow from negative to positive, this means that the electrons in this case flow from the power supply to the bottom electrode when a negative voltage is applied). With this in mind, when considering the hysteretic behaviour of the device in figure 6.7, the switching appears to take place primarily at the bottom electrode, where the Au forms the Schottky barrier with the ZnO.

Switching for this device is very reliable; devices of this configuration that exhibited hysteresis behaviour did so repeatably, with very little variation in hysteresis

observed over 5 sweeps at each voltage magnitude. It should be noted, however, that this configuration, not having a layer of PMMA, suffers the same general issues as observed in the Au/ZnO/Au configuration; namely, that functioning device yield per sample is low. Again, this can be attributed to the deposited Al layer partially depositing between the ZnO nanorods; as in the case with the Au/ZnO/Au configuration, this can be alleviated by addition of a PMMA layer between the ZnO and top electrode, as will be shown later.

Figure 6.8 shows an energy band diagram for the Au/ZnO/Al configuration. The Al/ZnO interface forms an Ohmic contact as Al has a lower work function than the electron affinity of ZnO. However, Al is more reactive than Zn, and as a result, oxygen vacancies at or near the interface may migrate to the Al contact, resulting in the formation of thin ZnO_{1-x} and AlO_{0+x} layers at the interface. This may modify the work functions enough to produce a Schottky barrier [*180*]. Further investigation is needed to confirm this.

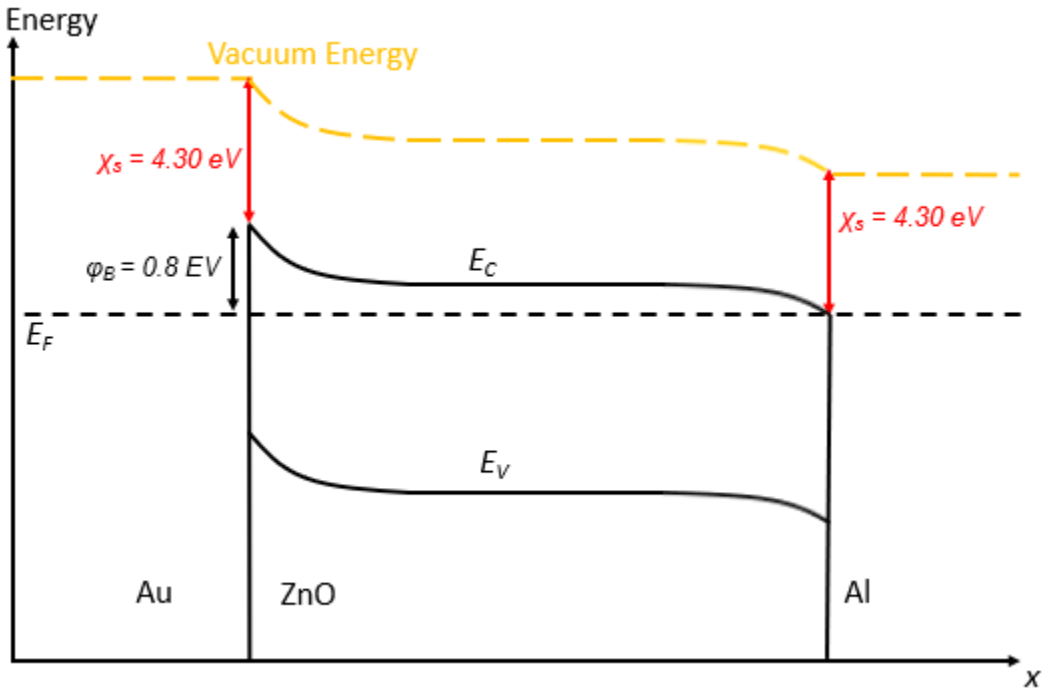

Fig. 6.8: An energy band diagram for the Au/ZnO/Al configuration. As Al has a slightly lower work function than the electron affinity of ZnO, an Ohmic contact is formed instead of a Schottky contact.

Figure 6.9 shows an energy band diagram for the ITO/ZnO/Al configuration. This is very similar to the Au/ZnO/Al configuration, as shown in figure 6.8 above; however the work function of ITO is different from Au, giving a barrier height of 0.5 eV for ITO instead of 0.8 eV for Au.

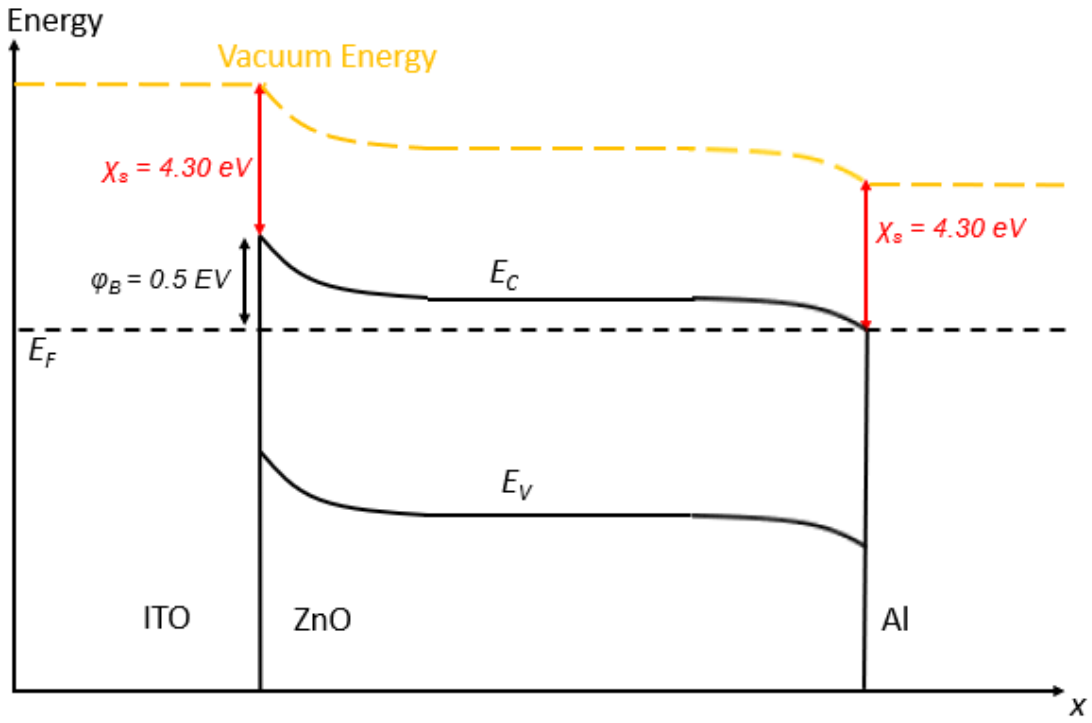

Fig. 6.9: An energy band diagram for the ITO/ZnO/Al configuration.

Figure 10 shows the I-V sweep data for a device made using ITO as a bottom electrode, with an ITO/ZnO/Al configuration, with 100 μm x 100 μm device area. At low voltages, the switching magnitude is quite small; this improves beyond voltage magnitudes of ~2 V. However, the devices start to form new current paths quite quickly, with voltage magnitudes of only ~4 V causing erratic behaviour in the device.

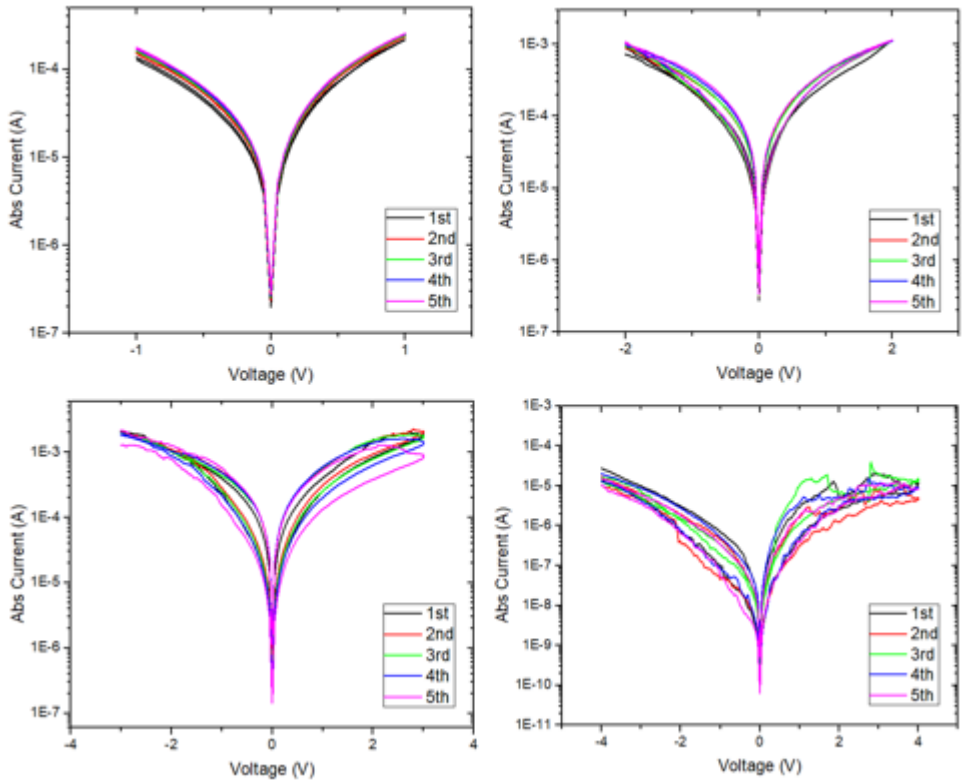

Fig. 6.10: I-V sweep data for a memristor device with ITO/ZnO/Al configuration. On/off resistance ratio is below 10 (1 order of magnitude).

6.1.1.1 Comparison with PMMA

The addition of a PMMA layer, spin coated onto the sample using the method detailed in section 4.1.3, is expected to improve working device yields by forming a barrier film between the top electrode and the bottom electrode, coating the nanorods to “seal” the gaps between them.

Figure 6.11 shows I-V sweep characteristics for a device of Au/ZnO/PMMA/Au configuration with 100 μm x 100 μm device area, where the PMMA layer was spin

coated at 3000 rpm. It can be seen from the image that the device exhibits greater on/off ratios than many of the Au/ZnO/Au devices, with switching being apparent even at low voltages. Currents remain low as the voltage increases, with no major observable changes in the behaviour as the bias is increased.

This is a significant change compared with devices of Au/ZnO/Au configuration that typically derive new current paths at comparable voltages (-5 V to +5 V sweeps, as shown in figure 6.3), and are non-repetitive and unreliable in their hysteresis behaviour prior to such voltages. The PMMA may be reducing these undesirable traits from the Au/ZnO/Au configuration as a result of the PMMA preventing the diffusion of Au atoms into the ZnO bulk, which is known to potentially affect the Schottky barrier height at the interface of the two materials [*47*, *180*].

A 5% weight-to-volume PMMA solution (in toluene) spin coated at 3000 rpm onto the sample produces a layer of ~ 100 nm on top of the nanorods. Thicknesses were measured using a Dektak XTL stylus profilometer.

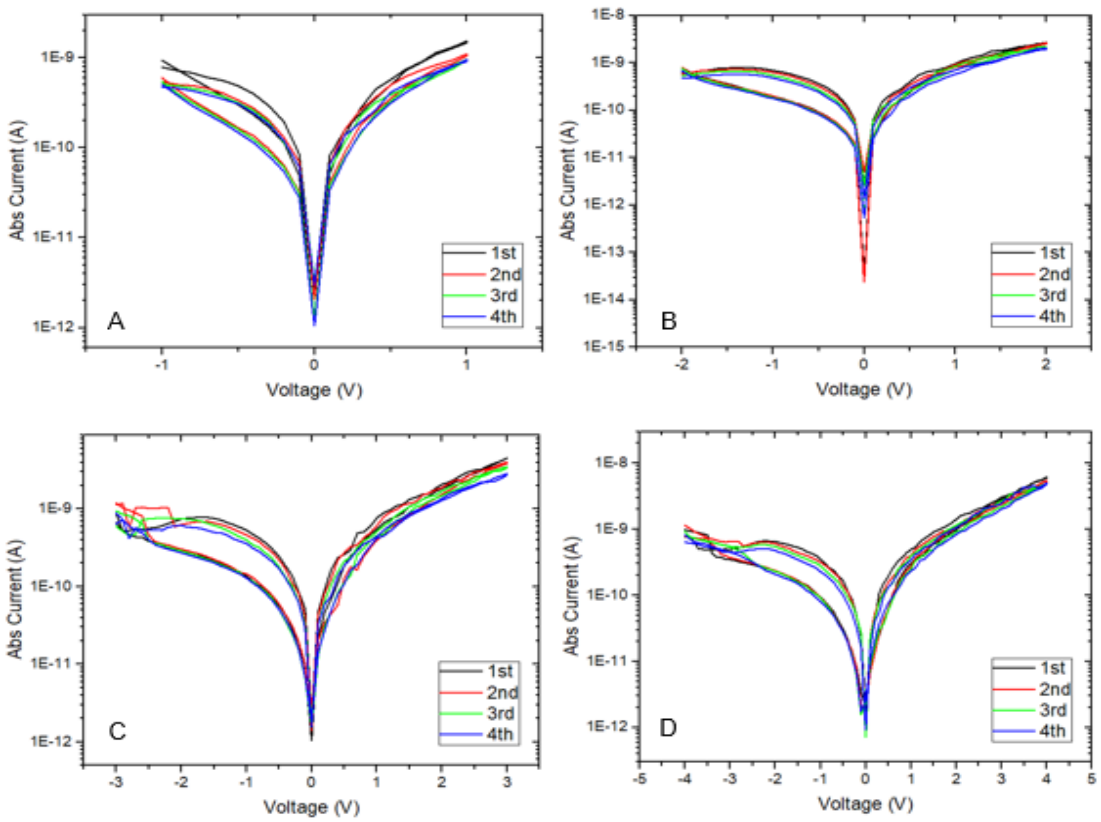

Fig: 6.11: I-V sweep characteristics of a 100 µm x 100 µm Au/ZnO/PMMA/Au device. The state separation at positive voltage is very small; this may be attributed to the change in barrier height at the interface between the top electrode and the PMMA.

Figure 6.12 shows I-V sweeps for a device of Au/ZnO/PMMA/Al configuration. On/off ratios at negative voltage polarity are larger even at lower voltages (~1 order of magnitude by 2 V sweeps), compared with the Au/ZnO/PMMA/Au configuration in figure 6.11 (~ half an order for the same voltage range). This is the same as was observed in figure 6.7 for Au/ZnO/Al compared with hysteresis observed in Au/ZnO/Au configurations.

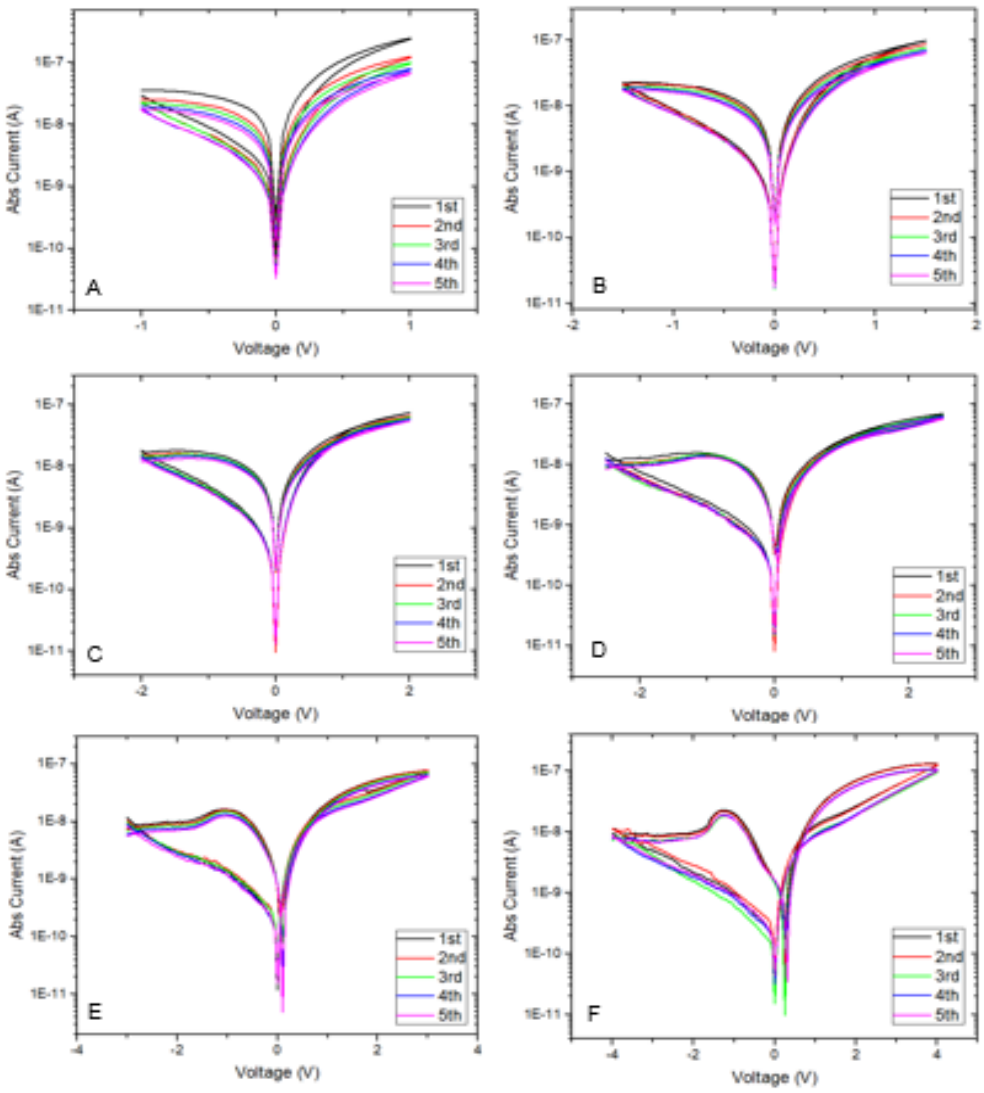

Fig. 6.12: I-V sweeps for a 100 µm x 100 µm Au/ZnO/PMMA/Al device. Voltage sweep ranges: A) -1 V to +1 V; B) -1.5V to +1.5 V; C) -2 V to +2 V; D) -2.5 V to +2.5 V; E) -3 V to +3 V; F) -4 V to +4 V. As the applied voltage increases, a charging effect begins to be observed.

In figure 6.12, a negative differential resistance (NDR) is observed in the negative polarity sweep. NDR is a phenomenon by which the current decreases while the voltage increases, at some specific point on an I-V curve [*188*]. In figure 6.12 this occurs at approximately -1.8 V. This behaviour has been observed in literature [*189*]

and it is explained that NDR can result from any conduction mechanism that is dependent on temperature and electric field such that thermal runaway occurs at sustainable fields and temperatures; the NDR itself is a result of Joule heating (heating caused by a transfer of energy due to electrical current flow, which is dependent on the resistivity of the material [*190*]).

In all of the cases discussed previously, the probe attached to the V Output terminal of the Agilent pA meter/DC voltage source was placed on the bottom (Au) electrode, while the I Input terminal probe was placed on the top (Al) electrode. By switching the probes to the opposite electrodes (V Output probe on Au, I Input probe to Al), we apply the voltage in the opposite direction and see the switching in “reverse”, with the asymmetry favouring higher switching magnitudes on the left, mirroring that shown in figure 6.12.

Figure 6.13 demonstrates this. In both figures 6.12 and 6.13, we see that the current on the return sweep does not drop back to its minimum at 0 V, but instead that a shift has occurred in the direction attributed to the Al electrode (positive polarity in figure 6.12, and negative polarity in figure 6.13). This may be due to capacitive charging effects at the top electrode, as the PMMA is an insulator.

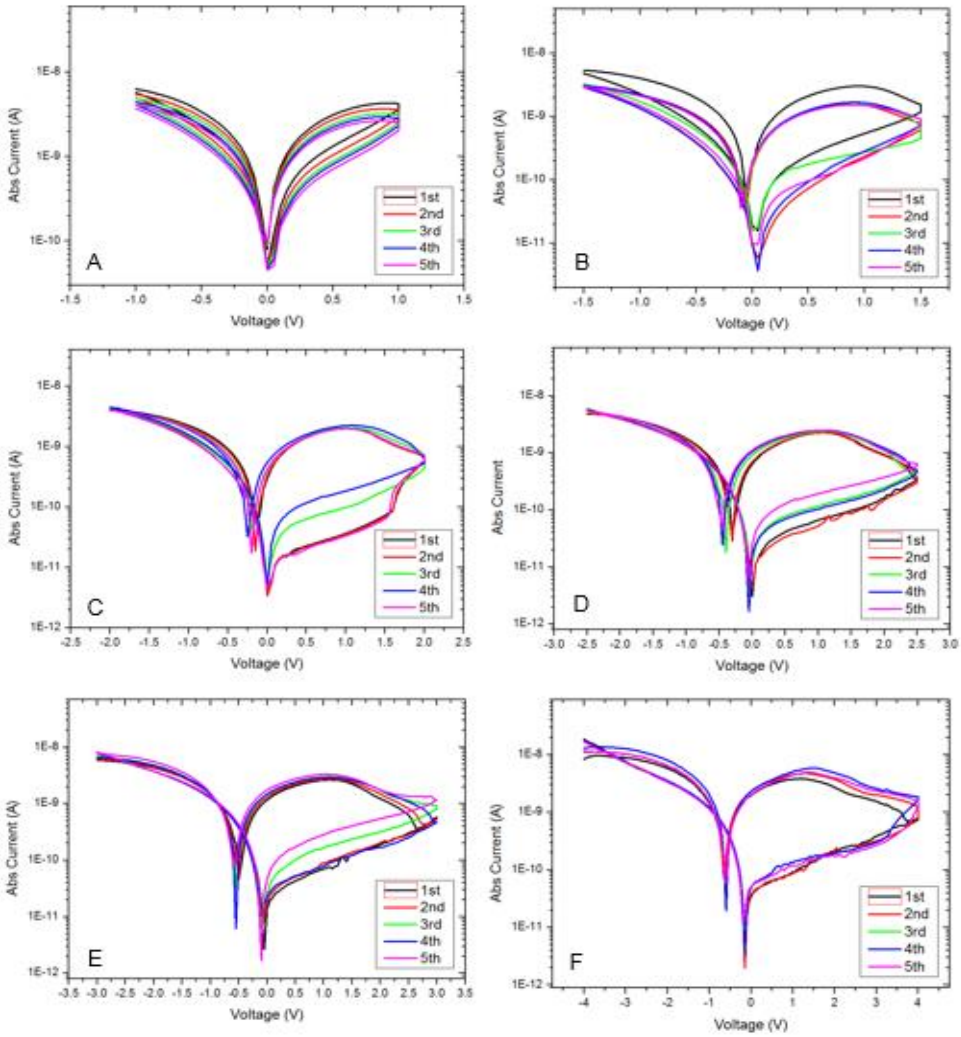

Fig. 6.13: I-V sweeps carried out on a 100 μm x 100 μm Au/ZnO/PMMA/Al memristor, with voltage applied to the top electrode (Al) instead of the bottom electrode (Au).

Figure 6.14 shows the I-V sweep characteristics of a device with ITO/ZnO/PMMA/Al configuration.

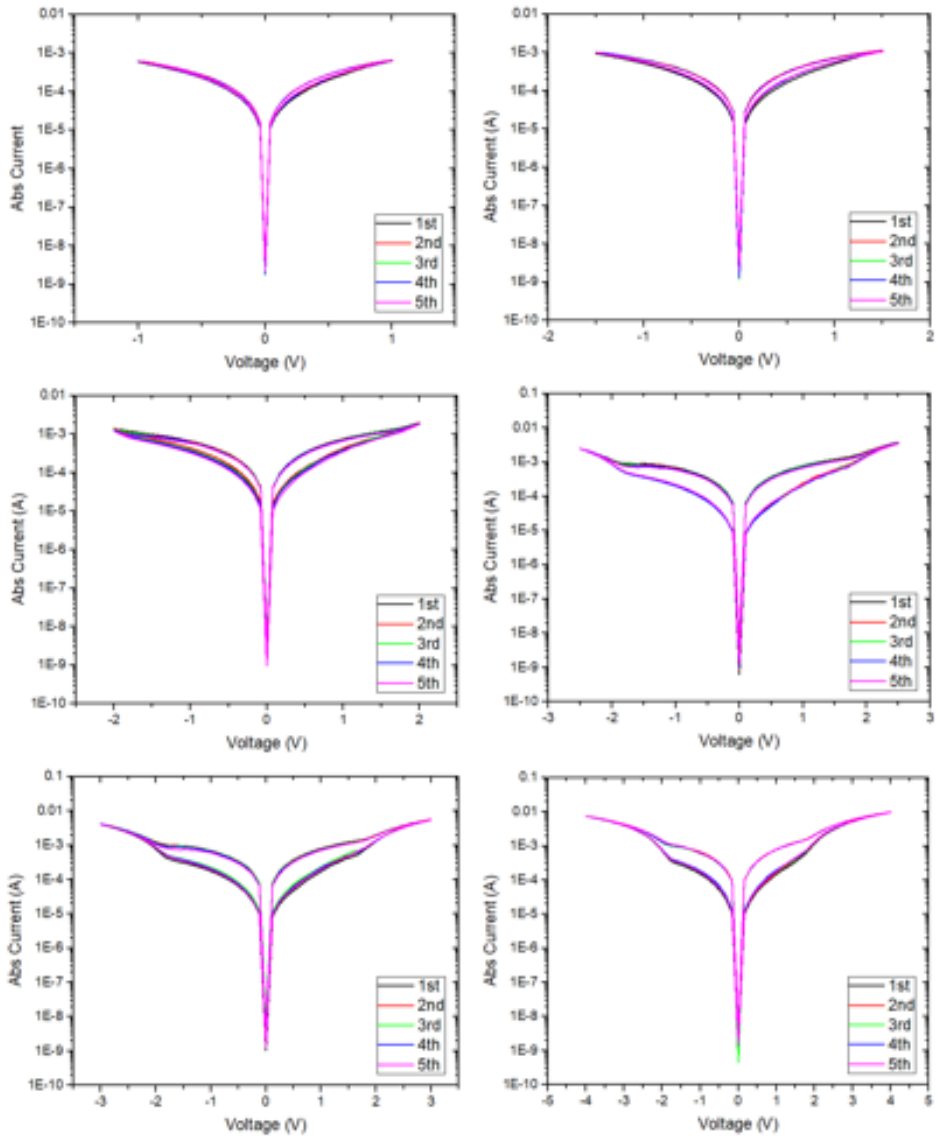

Fig. 6.14: I-V sweeps of an ITO/ZnO/PMMA/Al device.

The current is surprisingly high (starting at 10^{-3} A) given the presence of the insulating PMMA layer, even at low voltage, although switching occurs early and with reasonable separation between resistance states. The reason for this high current is unclear, although high currents have been observed in literature for configurations using ITO as a bottom electrode [*191*].

As can be seen from figures 6.1 – 6.14, different electrode materials affect the switching phenomenon in different ways. All samples are capable of switching at low voltages (state separation can be observed at voltages of < 1 V, and for all configurations a sweep between -1 V and +1 V shows hysteresis), but samples do not reproducibly demonstrate on/off ratios greater than 10 (one order of magnitude). Samples with Au for both the top and bottom electrodes typically exhibit the smallest on/off ratios (~ 5, rarely achieving on/off ratios of 10), while samples that use Al as a top electrode with Au as the bottom electrode typically exhibit on/off ratios closer to 10.

It is notable that, when Al is used as a top electrode while Au is the bottom electrode, the hysteresis is very asymmetrical. This is most likely due to the conduction mechanisms involved, as Au forms a Schottky barrier height of 0.8 eV with ZnO, while Al is typically expected to form an Ohmic contact due to its lower work function. This is supported by the fact that the additional PMMA layer in the Au/ZnO/PMMA/Au configuration produces an asymmetry in the I-V characteristics (which may be attributed to modification of the barrier height, as the top electrode interface is now PMMA/Au instead of ZnO/Au, and the ZnO interface is now with the PMMA), and is also supported by the fact that, as can be seen in figures 6.12 and 6.13, when the sweep was carried out in reverse (with the V Output probe from the HP 4140 B pA meter on the Al electrode and the I Input probe on the Au electrode), the asymmetry is reversed. This suggests a Schottky emission transport mechanism is involved.

ITO was also tested as a bottom electrode with Al, however the on/off ratios without the addition of the PMMA layer are not as large (typically ~ 5).

6.1.2 Investigation of the Role of the PMMA Layer

This sub-chapter presents the results of a brief investigation to ascertain the full effect of adding the PMMA layer, and the effect of altering the thickness of the PMMA layer.

Figure 6.15 shows I-V sweeps for a device of Au/ZnO/PMMA/Au configuration, with a thin PMMA layer produced by spin-coating a 5% solution of PMMA dissolved in toluene, at a spin speed of 2000 rpm, which produces a ~ 180 nm PMMA layer. The on/off ratios in this case are smaller compared to those of many of the Au/ZnO/Au devices (on/off ratio of ~ 2 – 3, compared with 5 or higher for Au/ZnO/Au), as seen by comparing with figure 6.4; however, the operating current is still quite low, even when a larger bias is applied to the device. While the device does not switch well until a higher magnitude of voltage is applied, it is also true that the device does not appear to degrade even when a voltage of 10 V magnitude is applied.

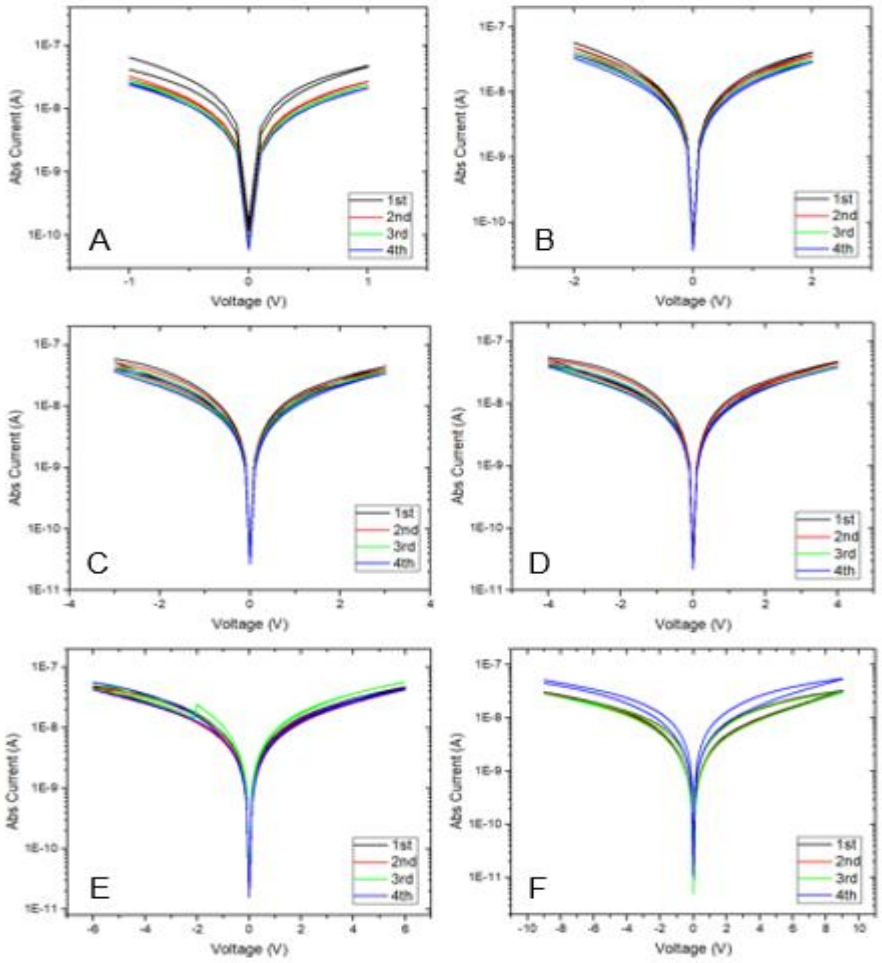

Fig. 6.15: I-V characteristics for a 100 μm x 100 μm device with Au/ZnO/PMMA/Au configuration. Sweeps between: A) -1 V to +1 V; B) -2 V to +2 V; C) -3 V to +3 V; D) -4 V to +4 V; E) -6 V to +6 V; F) -10 V to +10 V.

Figure 6.16 shows I-V sweeps for a device with a ~ 350 nm layer of PMMA, spin coated as a 10% solution in toluene at 1000 rpm. At this increased thickness, the resistive switching is not observed at low voltages initially but does occur at higher voltages (magnitudes of 6 V or higher).

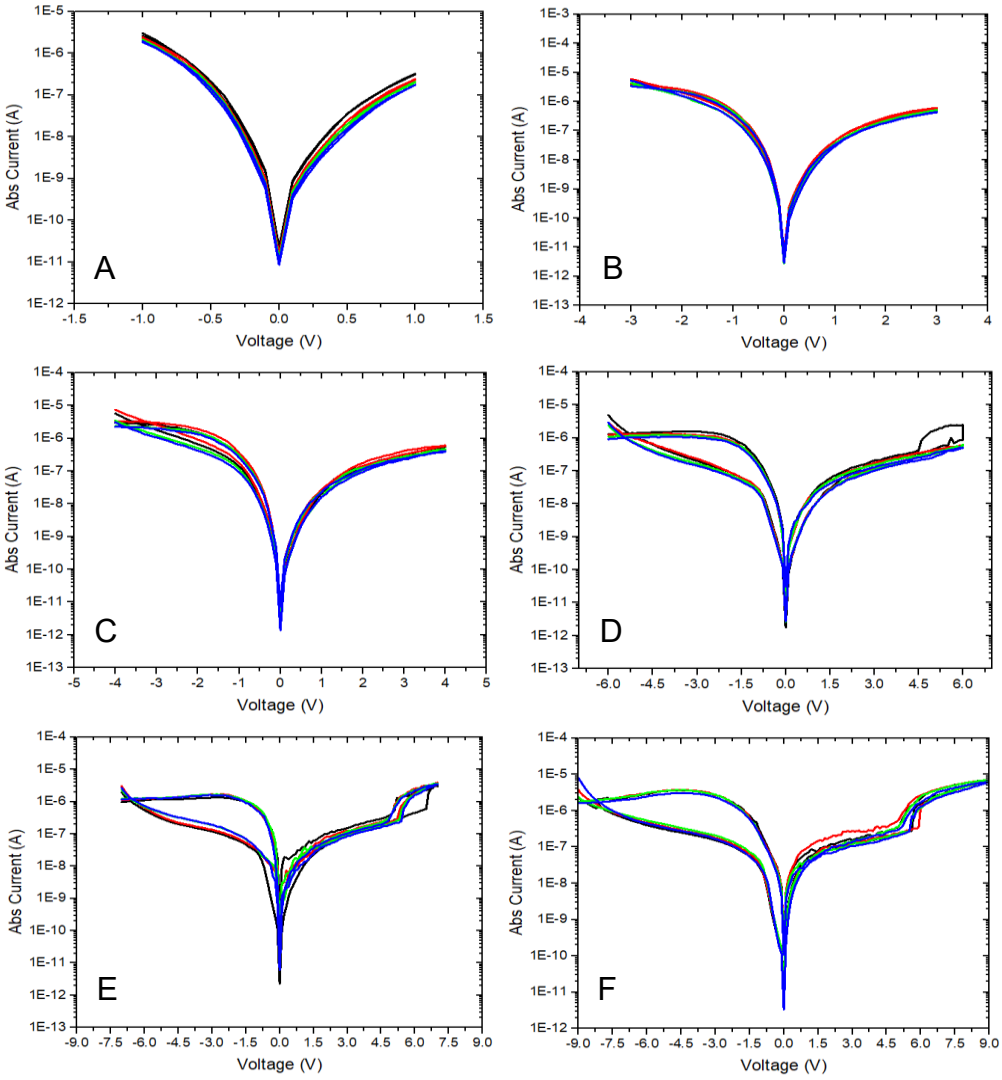

Fig. 6.16: I-V characteristics for a 100 μm x 100 μm device with Au/ZnO/PMMA/Au configuration, with a thicker PMMA film. Sweeps between: A) -1 V to +1 V; B) -3 V to +3 V; C) -4 V to +4 V; D) -6 V to +6 V; E) -7 V to +7 V; and F) -9 V to +9 V.

The asymmetry can again be attributed to the differences in interface transport mechanics at the bottom and top electrodes, with the PMMA/Au interface forming a different Schottky barrier compared with the Au/ZnO interface at the bottom electrode. As the PMMA layer is now much thicker (~350 nm, instead of the ~100 nm of our typical procedure), a much higher voltage (~6 V magnitude) is required for

transport mechanisms across the PMMA layer to occur. In addition, a sudden and abrupt increase in current can be observed at about +5 V in E), and about +6 V in F). The cause of this behaviour is uncertain but may be a result of diffusion of oxygen vacancies or Au atoms through the PMMA layer.

6.1.3 Endurance and Retention

Endurance characteristics were taken for a device with ITO/ZnO/PMMA/Al configuration (PMMA layer is ~ 200 nm thick), up to 10,000 cycles. After each “SET” operation, a “RESET” was performed to bring the device back to its “OFF” state before applying another “SET” operation.

Endurance data shows the absolute current density of the device at an initial “READ” voltage of +0.4 V for 1 s, followed by a pulsed “SET” (+3 V) or “RESET” (-3 V) voltage applied to the device for 0.1 s, and then continuing with a “READ” voltage.

Data was taken after a threshold number of cycles had been reached. Figure 6.18 shows the endurance characteristics of the “ON” state, after each key “SET” operation.

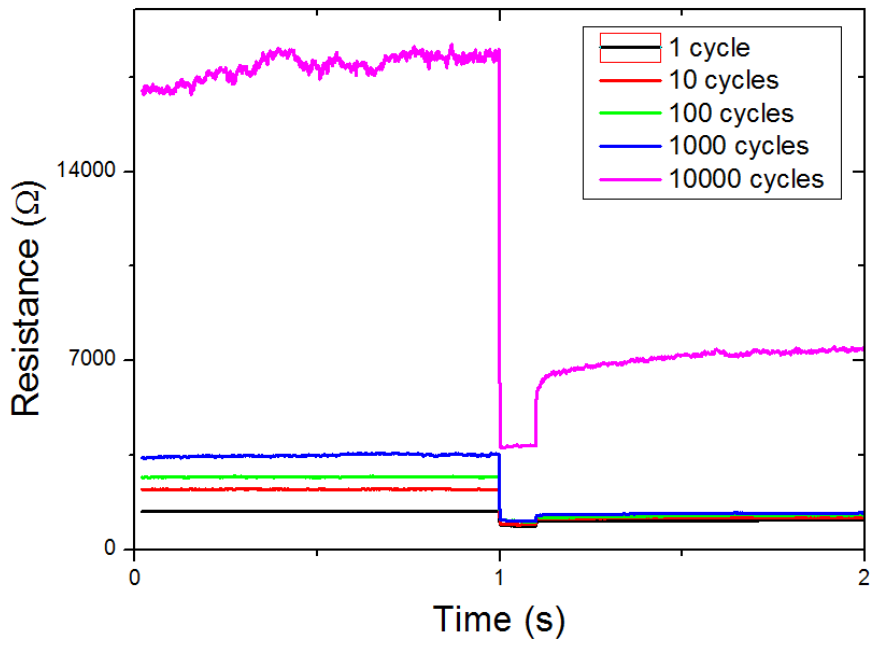

Fig. 6.18: Endurance data for an ITO/ZnO/PMMA/Al device, showing the resistance of the device after a set number of cycles. A “read” voltage of +0.4 V was applied for 1 s, followed by a “SET” pulse at 3 V for 0.1 s, and then the “read” voltage was applied again for 0.9 s. Data presented is for the “ON” state.

Figure 6.19 shows the endurance characteristics of the “OFF” state, after each key “SET” operation.

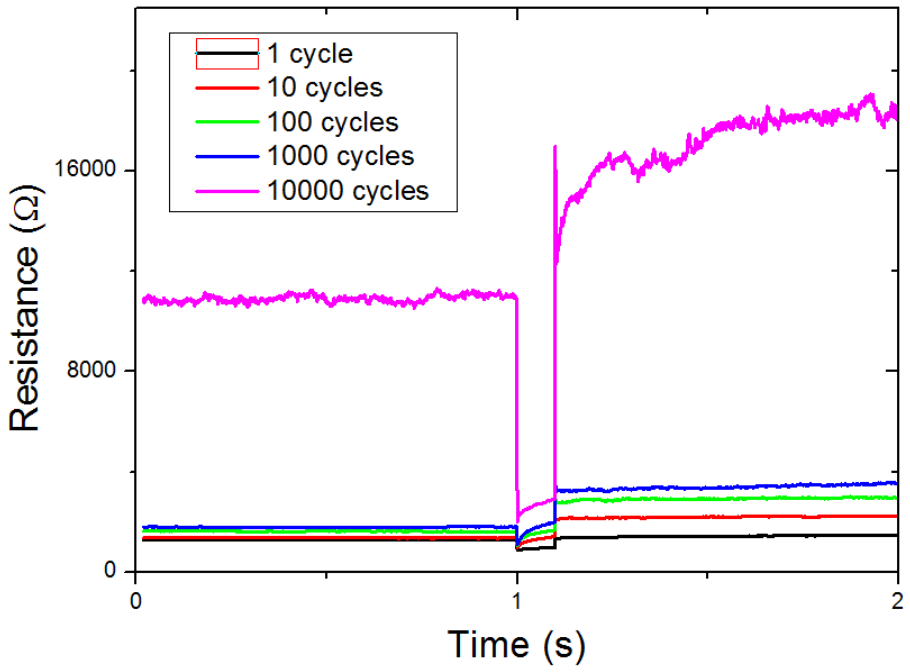

Fig. 6.19: Endurance data for an ITO/ZnO/PMMA/Al device, showing the resistance of the device at each key pulse. A “read” voltage of +0.4 V was applied for 1 s, followed by a “RESET” pulse at -3 V for 0.1 s, and then the “read” voltage was applied again for 0.9 s. Data presented is for the “OFF” state.

Figure 6.20 shows the resistances for both the “ON” and “OFF” states as they progress through multiple SET and RESET cycles, up to 10,000 cycles. The resistances for both states gradually increase as the number of cycles increase, showing a potential degradation of the device; however the two states remain separated.

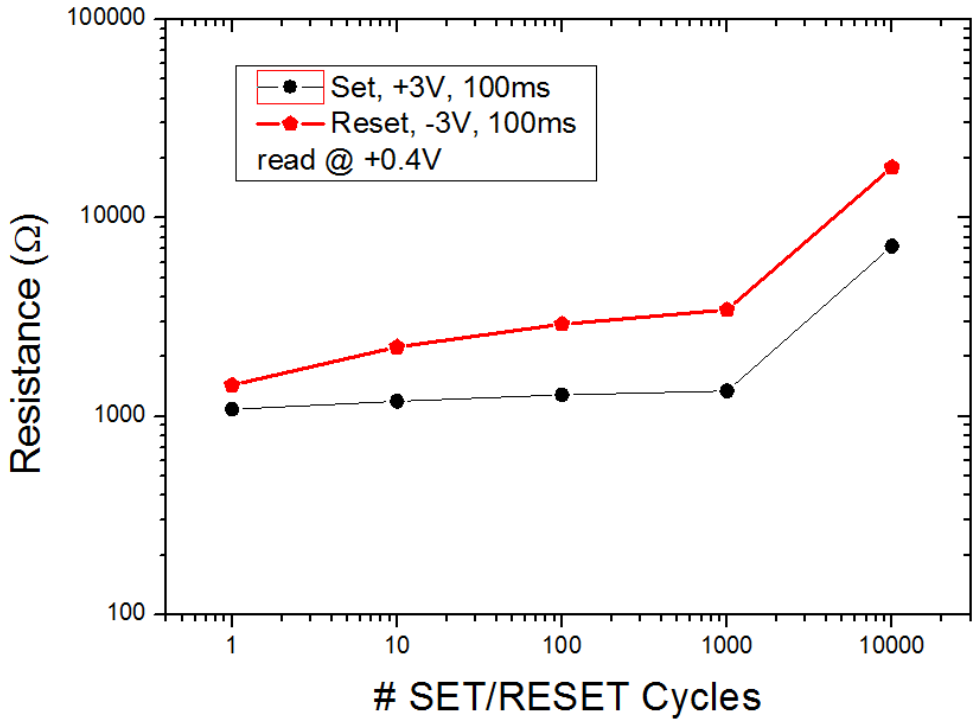

Fig. 6.20: A plot of the resistances for the "ON" ("SET") and "OFF" ("RESET") states after application of multiple SET/RESET cycles. The On/off ratio gradually increases with more cycles.

As can be seen from figures 6.18 – 6.20, the samples continue to switch between the "ON" and "OFF" state after 10,000 cycles; however, the resistance of the device significantly increases, and the on/off ratio increases with the number of cycles as well, indicating low endurance stability. The reason for this is unclear, as the change in resistance over 10,000 cycles is large (the resistance at the first sweep is ~1 kΩ for the initial "read" voltage, and drops only a little below that for the second "read" after the "SET" pulse is applied; after 10,000 sweep cycles, resistance has increased to ~17.5 kΩ for the first "read", and ~7 kΩ for the second "read" after the "SET" pulse; similar changes are observed in the "RESET" case). This could be the result of an alteration of the Al electrode at the PMMA/Al interface, due to migration

of oxygen vacancies from the ZnO nanorods through the PMMA layer; this would form a thin layer of aluminium oxide (Al_2O_3) at the PMMA/Al interface, which is insulating. As the “SET” and “RESET” pulses are very short (0.1 s) compared with the stepped I-V sweeps carried out earlier in the chapter (in which voltage is increased or decreased by 0.01 V increments in a 0.1 s interval between voltage pulses, up to the maximum applied voltage), the transferred energy may not be sufficient to entirely migrate the oxygen vacancies back across the barrier to the ZnO nanorods during the “RESET” process, as Al is more reactive than Zn. A more detailed investigation is required to identify whether this is the case, as this endurance instability is an issue with oxide-based memristors [*134*] that must be addressed in order for them to be viable for commercialization, and a more thorough understanding of the cause of this instability is paramount to resolving the issue.

Retention data was taken for a similar device, with the same configuration and from the same sample. A +0.4 V “READ” bias was applied to the device, and then a +3 V pulse was applied for 0.1 s to switch the device into the “ON” state. The “READ” voltage was then applied for 600 s. This was then repeated for the “OFF” state, switching the pulse bias to -3 V for the “RESET” operation. Figure 6.21 shows the retention data for the “ON” state.

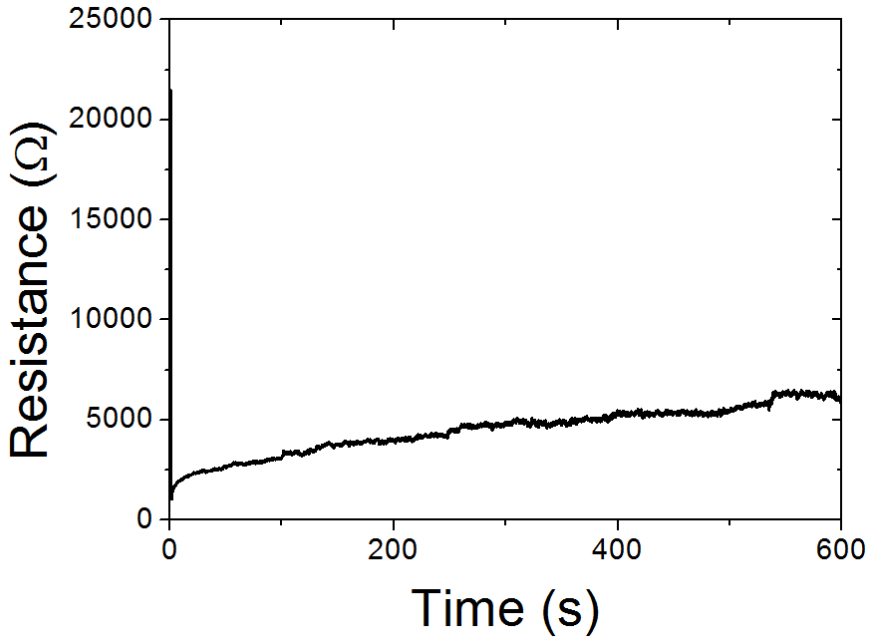

Fig: 6.21: Retention data for the “ON” state of a device with ITO/ZnO/PMMA/Al configuration. The initial vertical line on the graph shows the change from the initial state to the “ON” state, representing the 0.1 s pulse of voltage that instigated the switch.

Figure 6.22 shows the retention data for the “OFF” state. For both processes, the state seems to be maintained over the course of the 600 s period. The data does not indicate any favouring of either state; both states are equally well maintained by the device after the switching operation has been carried out.

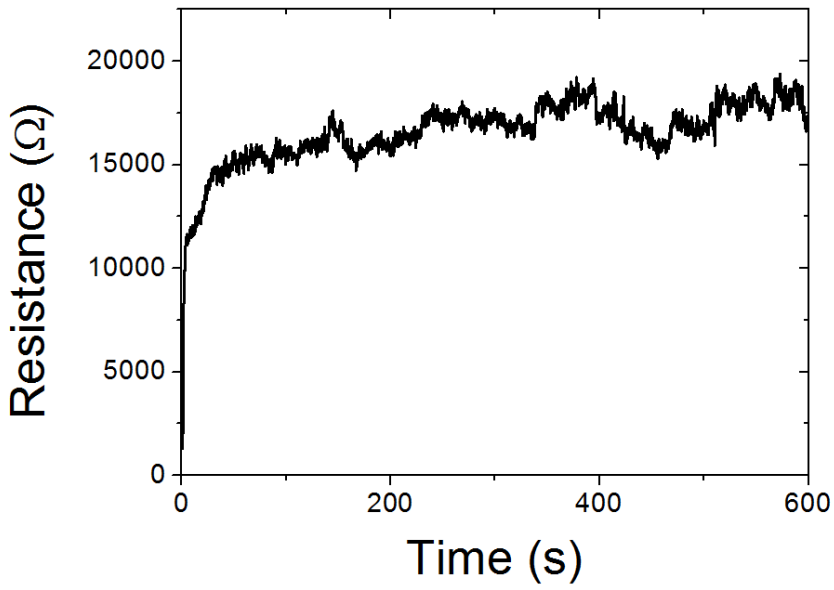

Fig. 6.22: Retention data for the “OFF” state of a device with ITO/ZnO/PMMA/Al configuration.

Our retention data is quite limited. Only data for an ITO/ZnO/PMMA/Al device was collected, and the data does not paint a very clear picture as to how well the devices function. This is in part due to the sensitivity of the system used for measuring the retention, in particular; the I-V measurement system is situated on a bench top in a working laboratory, and due to the long run times required for obtaining good retention data (hours or days, ideally, in order to provide enough data to accurately extrapolate the lifespan of each resistance state), the system is prone to producing erratic or anomalous data as a result of physical vibrations (caused by doors opening and closing nearby, use of the desks nearby etc.) affecting the electrical signal.

The retention data in figures 6.21 and 6.22 only covers 600 s, which is 10 minutes. The “SET” (6.21) and “RESET” (6.22) pulses can be observed at the start of data collection; the image is scaled to highlight the “READ” activity, and as such the “SET” and “RESET” pulses continue out of the graph. While the retention data is taken over too short of a duration to draw any firm conclusions about the longevity of the resistance states, there does not appear to be any significant decay in the state over this duration. However, more data needs to be collected before a true understanding of the endurance and retention characteristics of the devices can be developed. Further, the effect of using different electrode materials, and the absence, presence and variation of the PMMA layer, on the endurance and retention characteristics should be investigated as well.

6.2 Resistive Switching in Nitrogen

This sub-chapter presents the I-V sweep data of a device with Au/ZnO/PMMA/Al configuration, in a nitrogen environment (~100 ppm oxygen and water vapour) in which the oxygen has been evacuated.

Figure 6.23 shows the I-V sweeps of the device in nitrogen conditions. Compared with the I-V sweeps taken in air (see figure 6.11) from the same sample, there is no switching occurring even at high voltages (> 10 V). Ten separate devices were tested, and these results are representative of those devices’ behaviour.

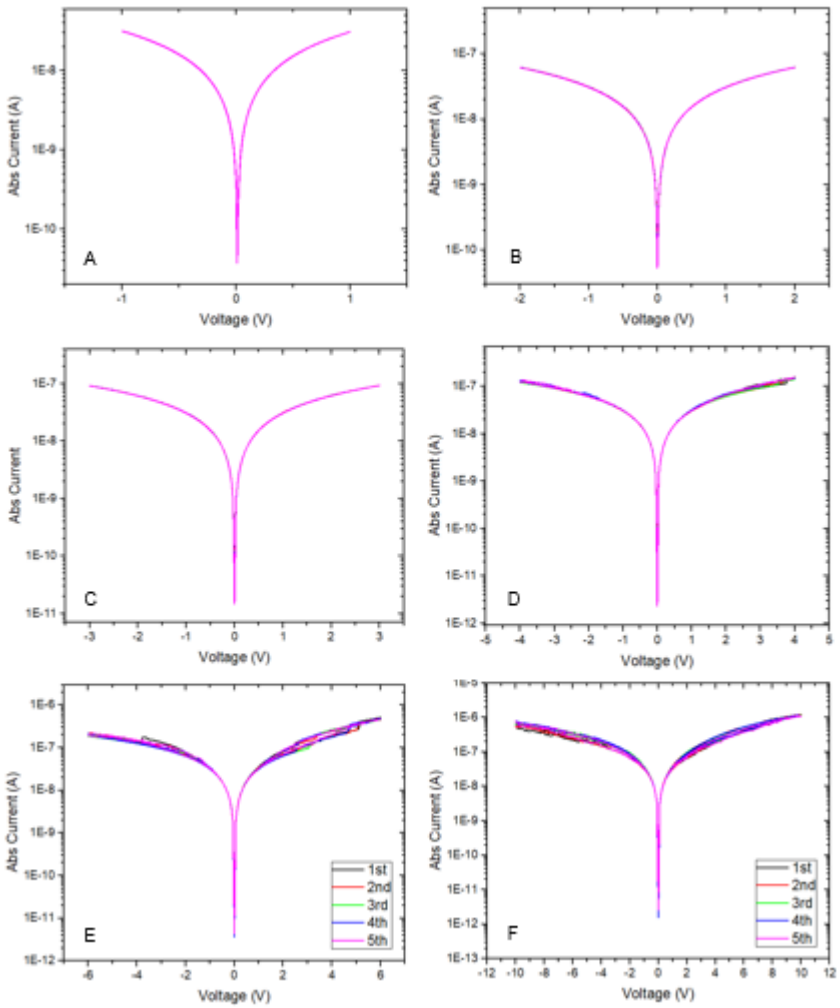

Fig. 6.23: I-V sweep data of a 100 μm x 100 μm Au/ZnO/PMMA/Al device measures in a nitrogen-rich environment.

We observe that switching occurs very readily when the device is switched in air under standard laboratory conditions. By contrast, the devices did not begin to switch in nitrogen until very high voltages were applied (> 10 V). At these voltages, producing much higher electric fields, other effects may begin to overshadow the switching mechanisms that are observed in ordinary switching in air. More

importantly, however, it is notable that such high voltages for very small on/off ratios would render the device unviable for commercial use.

The lack of switching in a nitrogen environment agrees with data published by J. Wang et al [*128*], in which it is found that devices measured in nitrogen or in a vacuum exhibit Ohmic behaviour and no hysteresis. They posited that the transport mechanism was associated with oxygen vacancies and the adsorption of oxygen at the surface of ZnO nanocrystals; adsorbed oxygen on the surface of the crystals acts as a trap for free electrons. Under forward bias, oxygen ions that are close to the Al/ZnO interface drift into the bulk, thus leaving oxygen vacancies at the interface. Molecular oxygen traps free electrons at the interface and adsorbs at the oxygen vacancies; this creates an increased barrier preventing electron injection. By applying a reverse bias, the oxygen ions that moved into the bulk now return to the Al/ZnO interface, and this reduces the number of oxygen vacancies, releasing the adsorbed oxygen molecules at the interface and restoring the device to its original conductance [*128*].

It is notable that switching still occurred in devices with a thick PMMA layer (even 350 nm layers of PMMA) coating the nanorods. PMMA is an insulator, and it may be expected that a uniform coating of PMMA on the nanorods would prohibit the adsorption of ambient oxygen at the nanorod surface. PMMA is also known to by hydrophobic, and thus able to prevent the intrusion of moisture into the nanorod layer [*192*]; as such, humidity effects would also be expected to be mitigated. The cause of the switching may be due to chemical and surface interactions at either the

ZnO/PMMA interface and/or the PMMA/Al interface, in an environment containing ambient oxygen (i.e. air, or a pure oxygen environment). It is known that storage in air can affect the properties of perovskites that have been passivated by a coating with PMMA [*192*], which suggests that a coating of PMMA may not prevent interaction of ambient oxygen with the ZnO nanorods. Further experimentation is required to clarify if this is the case.

Chapter 7

Identifying the Transport Mechanisms

This chapter discusses the different transport mechanisms for each device configuration produced using our fabrication method. Six device configurations are discussed in turn (Au/ZnO/Au, Au/ZnO/PMMA/Au, Au/ZnO/Al, Au/ZnO/PMMA/Al, ITO/ZnO/Al, and ITO/ZnO/PMMA/Al), showing plots for Schottky emission, Poole-Frenkel emission and space-charge-limited conduction (SCLC) mechanisms. The plots will be discussed with respect to whether the data fits the expected behaviour that would indicate the mechanism in question: a linear relationship between $ln\ I$ and $V^{1/2}$ for Schottky emission; a linear relationship between $ln\ I/V$ and $V^{1/2}$ for Poole-Frenkel emission; and a series of regimes of different slopes to indicate SCLC (an Ohmic region where the gradient/slope is ~ 1, a trap-controlled SCLC region where the slope is ~ 2, higher-order regions where the slope is > 2 that indicate an approach to the threshold voltage for the charge traps being filled, and a trap-filled SCLC region where the slope returns to ~ 2). This will allow the identification of the dominant transport mechanisms in each configuration.

The lengths of the nanorods would typically be expected to rule out the Fowler-Nordheim tunnelling mechanism, as this also occurs predominantly in very thin films of < 100 Å along with very high electric fields [*102*]. The tips, however, are tapered, and a Fowler-Nordheim mechanism could be occurring at the interface between the tips and the top electrode. The thickness of the PMMA layer should prohibit this.

For Schottky emission, the y-intercept of a Schottky plot, c_S, can be used to calculate φ_B, using this equation, derived from equation 12 in chapter 2:

$$c_S = \frac{-q\varphi_B}{kT} + lnA^* \quad (29)$$

A^* is the Richardson constant, which for ZnO is 3.2 x 10^5 $AK^{-2}m^{-2}$ [*193*]. It should be noted that c_S depends on the Schottky barrier height which is determined by both the electron affinity of ZnO and the work function of the interface material, and so it will be different for each configuration.

The gradient, m_S, can be used to calculate the dielectric constant of the ZnO, ε_r, using this equation, derived from equation 12 in chapter 2:

$$m_S = \left[\frac{q\left(\sqrt{q/4\pi\varepsilon_r\varepsilon_0}\right)}{kT}\right] \quad (30)$$

The static dielectric constant for ZnO is 4 (as it is equal to the refractive index squared) [*194*]. This gives us a predicted slope in the Schottky plot of 7.34 x 10^{-4} (or ~ 0.0007). If the experimental results approximate to this theoretical value for m_S for any specific configuration of our devices, then that configuration exhibits ideal Schottky emission behaviour.

For Poole-Frenkel emission, the y-intercept of the plot, $c_{P\text{-}F}$, can theoretically be used to calculate the trap energy level φ_t, using this equation, derived from equation 18 in chapter 2:

$$c_{P-F} = \frac{-q\varphi_t}{kT} + ln(qN_c\mu) \qquad (31)$$

The density of states (N_c) and electron drift mobility (μ) for ZnO in our configurations is not known. As such, the value of φ_t cannot be obtained from our data for any configuration.

The gradient, $m_{P\text{-}F}$, can also be used to calculate the relative permittivity (dielectric constant) of the ZnO, ε_r, using this equation, derived from equation 18 in chapter 2:

$$m_{P-F} = \left[\frac{q\left(\sqrt{q/\pi\varepsilon_r\varepsilon_0}\right)}{kT}\right] \qquad (32)$$

This gives us a predicted slope in the Poole-Frenkel plot of 1.47 x 10^{-3} (or ~ 0.0015). This is double the value of the predicted slope for Schottky emission. As is the case for Schottky emission, described above, if the experimental results approximate to this theoretical value for $m_{P\text{-}F}$ for any specific configuration of our devices, then that configuration exhibits ideal Poole-Frenkel emission behaviour.

7.1 Gold (Au) Bottom Electrode with Gold (Au) Top Electrode

Figure 7.1 shows the Schottky behaviour of a device with Au/ZnO/Au configuration. By plotting the natural log of the current against the square root of the voltage in the nonlinear regime of the I-V sweep, we can identify whether the sample exhibits behaviour fitting Schottky emission predictions, as highlighted in Chapter 2. A device that undergoes Schottky emission will show a linear relationship between ln I and $V^{1/2}$ in the nonlinear region that follows the Ohmic conduction region, as the two would be proportional as demonstrated in Chapter 2. However, a linear relationship alone is not enough to demonstrate Schottky emission. By instead plotting ln (J/T^2) vs. $E^{1/2}$, where T in this case is room temperature (~ 300 K), the Schottky barrier height φ_B can be calculated.

The figure shows four images: one showing an entire sweep for that device; one showing an I-V curve demonstrating where the switching begins (importantly, the curve demonstrates an exponential increase in current at a threshold voltage, similar in behaviour to a Schottky diode); one showing a Schottky plot (ln J/T^2 vs $E^{1/2}$) across the full data range shown in the second image, and one showing only the non-linear component. The two Schottky plots show a dotted fitting line, highlighting linear relationships between ln J/T^2 and $E^{1/2}$. The fitted line was added using the Quick Fit option in Origin 2015.

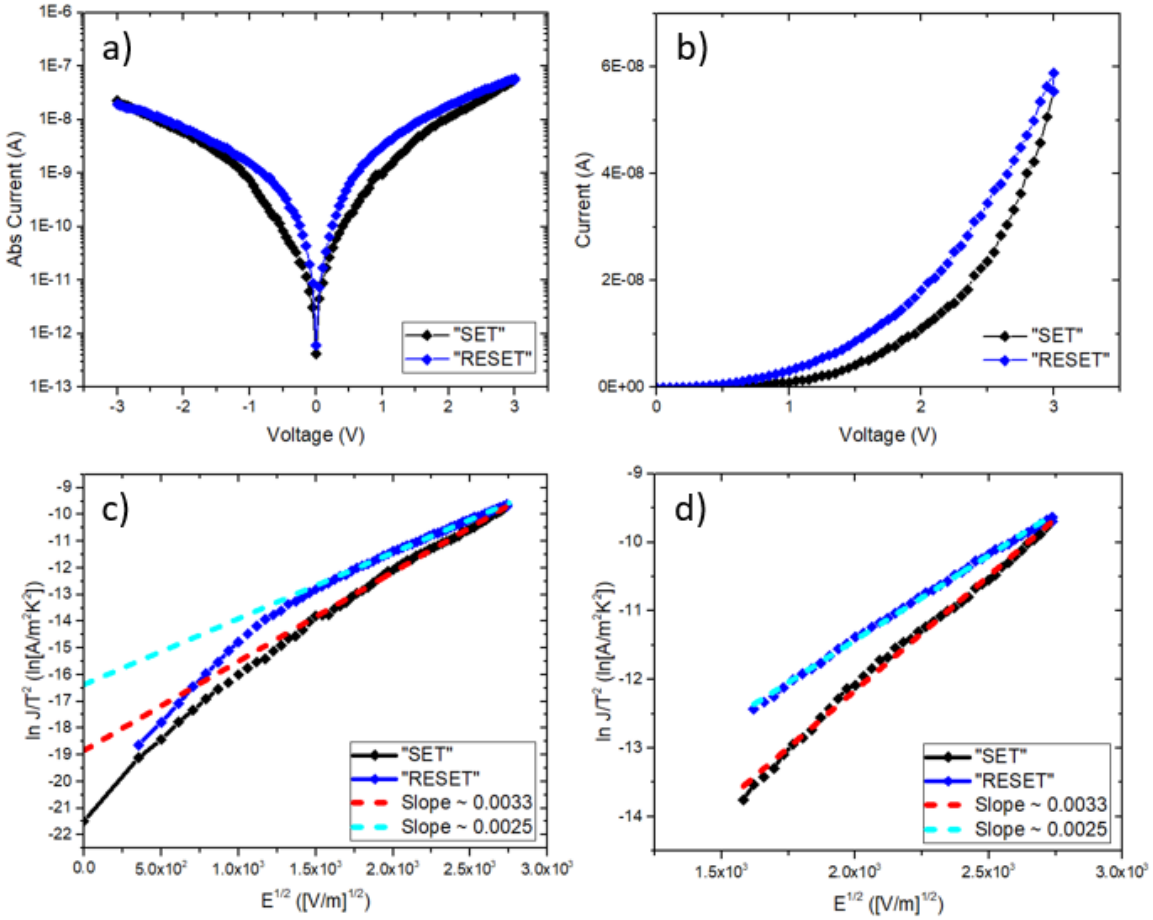

Fig. 7.1: A plot of ln J/T^2 vs. $E^{1/2}$ for the 3 V I-V sweep of the Au/ZnO/Au device: a) shows the full I-V sweep for the device, using a logarithmic y-axis with absolute current; b) shows the I-V curve only in the positive polarity region, and demonstrates that the resistance switching seems to occur at around 1 V; c) shows the Schottky plot (ln J/T^2 vs. $E^{1/2}$) for the entire positive polarity region, while d) focuses on the nonlinear region from 1 V onwards where the switching is identified. The dotted red fitted line closely follows the data in this nonlinear region, suggesting proportionality between ln J/T^2 and $E^{1/2}$, as predicted for Schottky emission. The y-intercept for the red fitted line, representing the "SET" sweep, is -18.84.

Using the y-intercept of -18.84 in equation 29, a barrier height of 0.81 eV is extracted. This is extremely close to the theoretical barrier height of 0.8 eV given by the difference between the work function of Au and the electron affinity of ZnO.

The gradient of 0.0033 for the “SET” sweep in figure 7.1 is much larger than the theoretical gradient of 0.0007 calculated using equation 32. This tells us that, although our results do allow for extraction of a Schottky barrier height that is accurate to the expected value, this configuration does not exhibit ideal Schottky emission behaviour. The gradient of the “RESET” sweep (cyan) does not significantly improve the extracted value for ε_r, indicating that no ideal Schottky emission behaviour is present.

By plotting ln (J/E) against $E^{1/2}$, the switching behaviour can be investigated with respect to Poole-Frenkel emission. Figure 7.2 shows the Poole-Frenkel analysis for an Au/ZnO/Au configuration; this is the same data that was used in the Schottky plot in figure 7.1.

The figure shows two images; one of the full data range, and one showing only the non-linear component, matching the voltage regions shown for the Schottky data above. Both show a dotted fitting line, highlighting a linear relationship between ln (J/E) and $E^{1/2}$, indicating that a Poole-Frenkel emission mechanism may be in effect; the gradient of the fitting line is 0.0024, and the y-intercept is -20.74. As with the Schottky images, this fitted line was added using the Quick Fit option in Origin 2015.

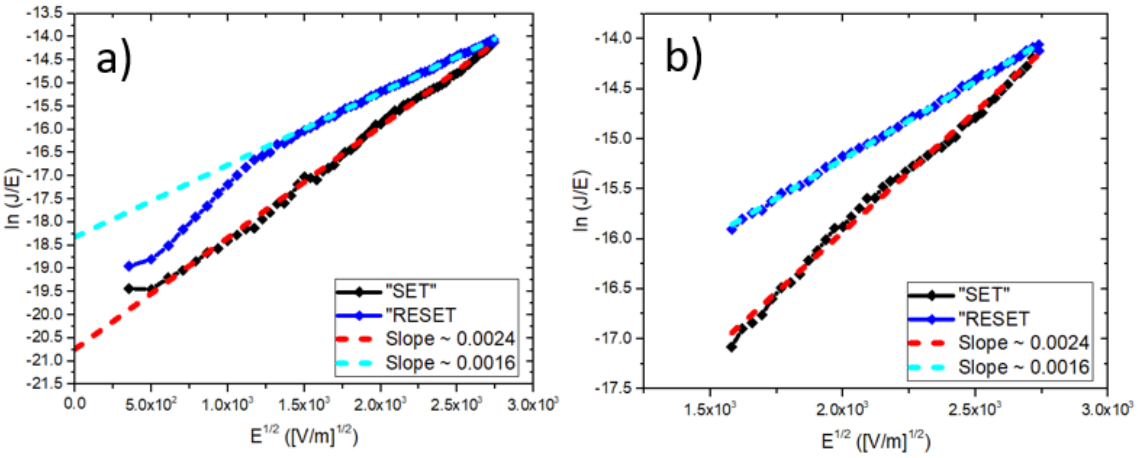

Fig. 7.2: A plot of ln (*J/E*) vs. $E^{1/2}$ for the nonlinear region of the 3 V I-V sweep of the Au/ZnO/Au device shown in figure 7.1: a) shows the Poole-Frenkel plot (ln *J/E* vs $E^{1/2}$) for the entire positive polarity region, while b) focuses on the nonlinear region from 1 V onwards where the switching is identified in figure 7.1b). The y-intercept for the red fitted line is -20.74.

The slope of the fitted line is less than that of Schottky emission (for normal Poole-Frenkel emission, as shown by our calculations from equation 32, the slope would be expected to be twice that of the Schottky slope, and for modified Poole-Frenkel emission the slope should equal the Schottky slope [*99*, *195*]). However, while the gradient of the “SET” sweep is slightly too high, the gradient for the “RESET” sweep is very close to the predicted slope from equation 32 (~ 0.0015). This indicates that this configuration exhibits behaviour very close to ideal Poole-Frenkel emission.

Figure 7.3 shows the I-V characteristics for the Au/ZnO/Au configuration, with both axes on logarithmic scales. This allows SCLC regimes to be identified, if present, by analysing the gradient (slope) of the I-V curve.

As explained in Chapter 2, typically an Ohmic region would be observed at the beginning of the sweep, where the slope should be ~1, indicating direct proportionality between current and voltage. This would be followed by a trap-controlled space-charge-limited conduction (TC-SCLC) region where the slope is ~2, indicating that $I \propto V^2$. This may be followed by regions with even greater slopes, indicating trap charge limited conduction regions in which $I \propto V^{\alpha}$, where $\alpha > 2$. Finally, once a specific threshold voltage has been reached, the trap-filled space-charge-limited conduction (TF-SCLC) region would be observed, where once again a slope of ~2 would indicate that $I \propto V^2$.

As in the previous cases, the fitting lines were applied using the Quick Fit function in Origin 2015.

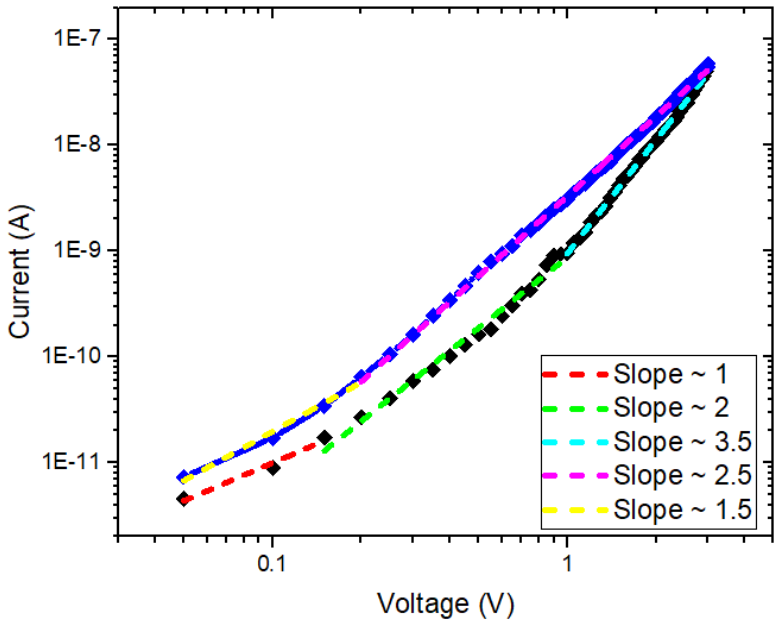

Fig. 7.3: I-V characterisation of an Au/ZnO/Au device, with respect to SCLC current. The quick fitting function in Origin 2015 was used to identify key SCLC regimes: a small Ohmic conduction region (in red), where the slope is ~ 1; a trap-controlled SCLC

region (in blue) where the slope is ~ 2; and a higher-order region (in green) where the current is exponentially increasing as it approaches the threshold voltage V_{TFL}. No trap-filled region is observed after this region, indicating that V_{TFL} was not reached.

Three regimes are identifiable that are typical of SCLC behaviour. The Ohmic region (red), where the slope is ~ 1, is unexpectedly short, as for this device we do not observe switching until close to 1 V (as seen in figure 7.1 earlier). A TC-SCLC region (blue), where the slope is ~ 2, can be observed, and a higher-order region (green) is also observed with a slope of ~ 3.5, as the threshold voltage is approached. However, no TF-SCLC is observed. This indicates that the threshold voltage has not been reached. The slopes that appear when the voltage sweep is reversed (magenta and yellow) may represent the gradual emptying of traps as the voltage approaches 0 V; there is no return to a purely Ohmic regime (slope ~ 1) in this region, as the device does not switch back to a high-resistance “OFF” state until a negative voltage is applied, and as such there would still be trap states that are occupied as a result of the SCLC mechanism.

The Au/ZnO/Au configuration exhibits a strong linear relationship between ln J/T^2 and $E^{1/2}$ in the 1 V – 3 V range and allows us to extract a value for the Schottky barrier height of 0.81 eV, approximately equal to the theoretical value of 0.8 eV. The slopes of the Schottky plot for both the “SET” and “RESET” sweeps do not approximate to the expected slope calculated from equation 29, indicating that the device does not exhibit ideal Schottky emission behaviour. This configuration also exhibits a linear relationship between ln (J/E) and $E^{1/2}$ in the same voltage range, which indicates a Poole-Frenkel emission; the slope of the Poole-Frenkel plot for the

“SET” state is slightly too high for ideal Poole-Frenkel emission, although for the “RESET” sweep the slope is very close to the predicted value from equation 32, suggesting that Poole-Frenkel emission might be contributing to the limitation of the current. As mentioned above, three specific regimes for SCLC can also be identified, suggesting that the switching may be a result of charge traps in the bulk material (as both Poole-Frenkel and SCLC mechanisms are bulk-limited and dependent on charge traps, which may be either zinc interstitials or oxygen vacancies).

7.1.1 With a PMMA Layer

The PMMA layer is intended to fill a number of roles: first, it is an insulating layer that is expected to reduce the current in the “OFF” state (which could potentially improve the switching on/off ratio), and also in the “ON” state, reducing the power consumed by the device and improving the device’s longevity; second, it coats the nanorods and the substrate, preventing the top electrode from sinking between gaps in the nanorod layer or other defects in the sample during the electrode deposition, which would otherwise potentially cause short circuits, and by preventing such, the PMMA should improve device yields. Additionally, it has been found [*196*] that PMMA can act as a buffer layer between the insulator/semiconductor and the metal electrode by forming an Ohmic contact, permitting the injection of electrons into the conduction band of the insulator.

Figures 7.4 – 7.6 show the Schottky, Poole-Frenkel and SCLC characteristics of a device made with Au/ZnO/PMMA/Au configuration, with a ~ 100 nm PMMA layer. Once again, fitting lines were added using the Quick Fit function in Origin 2015, to highlight linear relationships where they are observed.

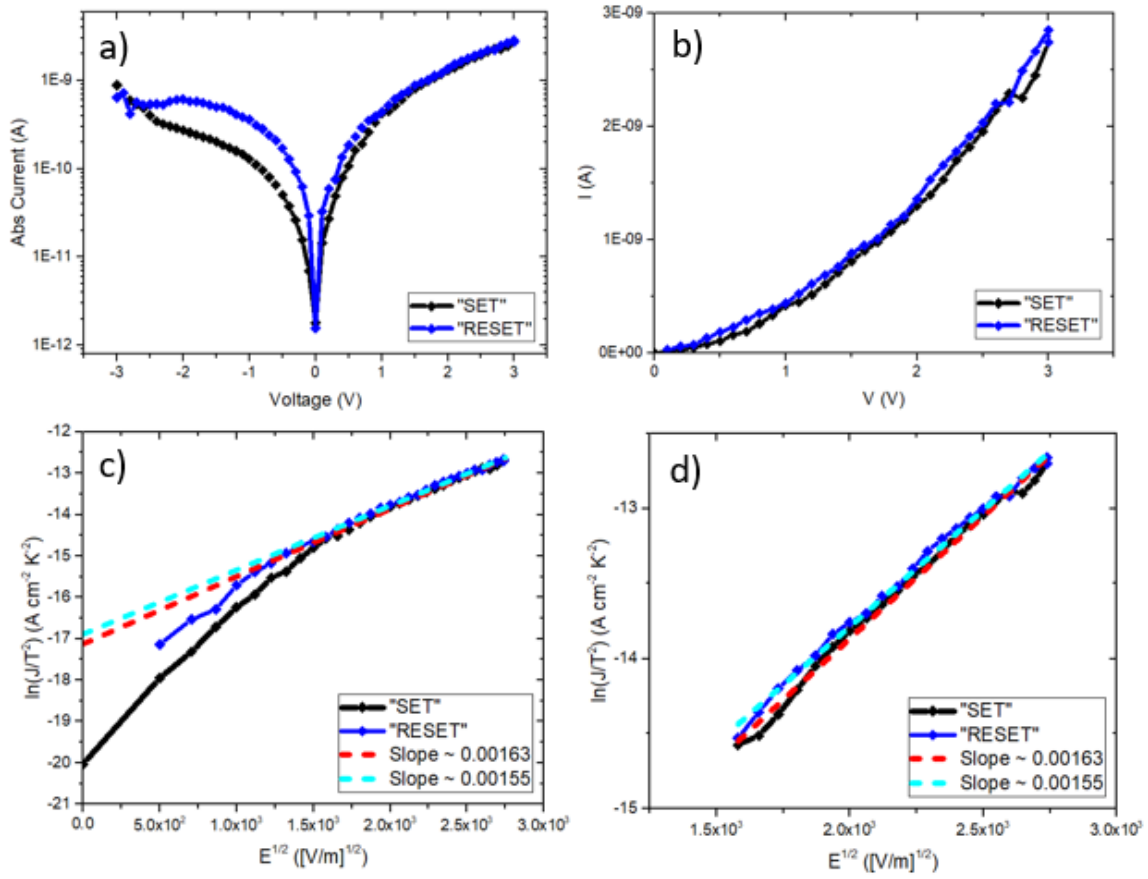

Fig. 7.4: A plot of ln J/T^2 vs $E^{1/2}$ for the nonlinear region of the 3 V I-V sweep of the Au/ZnO/PMMA/Au device: a) shows the full I-V sweep for the device, using a logarithmic y-axis with absolute current; b) shows the I-V curve only in the positive polarity region, and demonstrates that the resistance switching seems to occur at around 1 V; c) shows the Schottky plot (ln J/T^2 vs $E^{1/2}$) for the entire positive polarity region, while d) focuses on the nonlinear region from 1 V onwards where the switching is identified. A linear relationship is observed, as highlighted by the fitted line. The y-intercept is -17.13.

The extracted value for φ_B in this case is 0.77 eV. This is also close to the theoretical predicted value for a ZnO/Au Schottky barrier, although the interface at the top Au electrode is now with PMMA. The electron affinity for PMMA is typically only ~ 0.6 eV, which would be expected to form a barrier height with Au of ~ 4.5 eV. We can see from figure 7.4d that the "SET" and "RESET" slopes are very close, and that there is virtually no separation between them; all of this suggests that the switching is unlikely to be occurring at this voltage polarity, and that the switching is more likely to occur at the bottom electrode. The slope of the two lines is approximately twice as large as it should be, suggesting that the device does not exhibit ideal Schottky behaviour.

Figure 7.5 shows the Poole-Frenkel plots for this data.

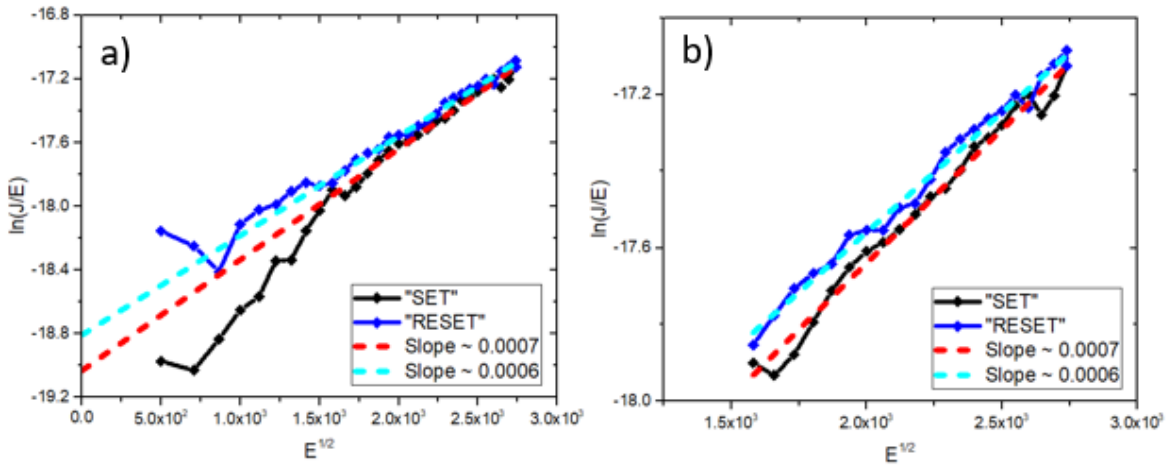

Fig. 7.5: A plot of ln (I/V) vs $V^{1/2}$ for the nonlinear region of the 3 V I-V sweep of the Au/ZnO/PMMA/Au device. The y-intercept for the "SET" slope is ~ 19.03.

Again, there does not appear to be much separation between the two states, so it is unlikely that resistive switching is occurring at this polarisation of voltage. The slope is now half of the predicted value for Poole-Frenkel emission, and as such matches the predicted slope for Schottky emission (although, as figure 7.4 showed, Schottky emission is unlikely); this might suggest that this configuration exhibits the "modified Poole-Frenkel emission" behaviour described in chapter 2, while the configuration without PMMA exhibits normal Poole-Frenkel emission.

Figure 7.6 shows the SCLC characterisation for this configuration.

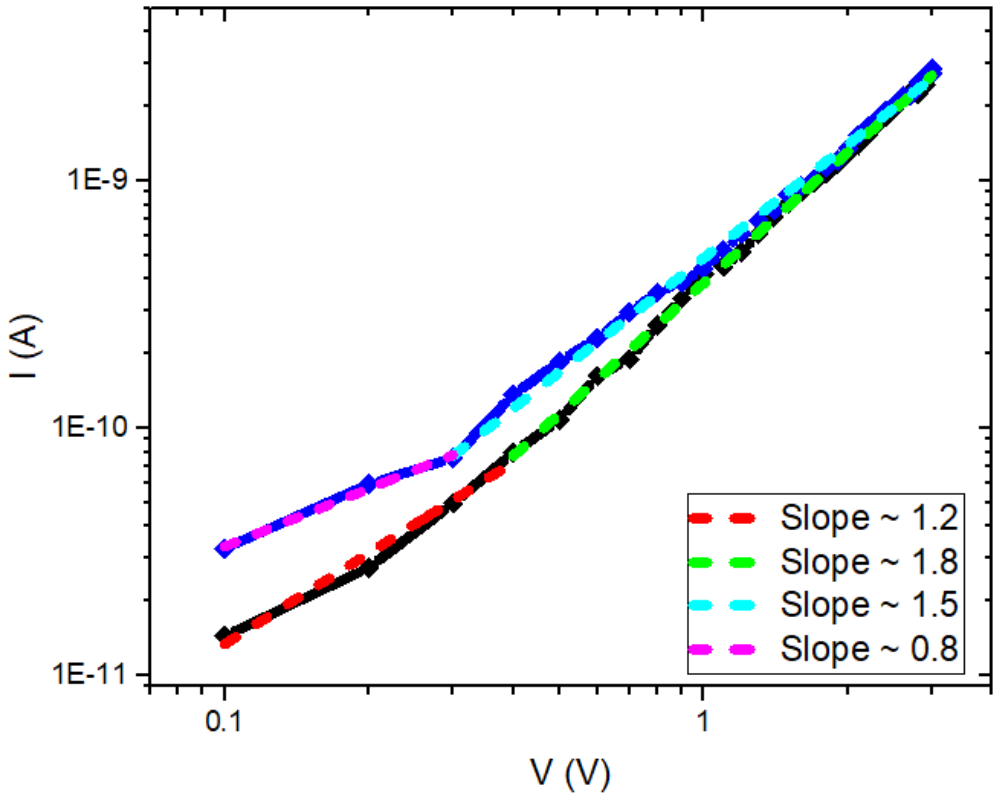

Fig. 7.6: I-V characterisation of an Au/ZnO/PMMA/Au device, with respect to SCLC current.

Compared with figure 7.3 (for the Au/ZnO/Au configuration), the SCLC profile for the Au/ZnO/PMMA/Au configuration (figure 7.6) does not fit the theory as presented in Chapter 2 quite as well; the initial Ohmic region has a gradient (slope) slightly greater than 1 (which would be expected in ideal SCLC profiles), and the following TC-SCLC region slope is slightly less than 2 (which would again be expected in the ideal case). Additionally, there is no higher order region, suggesting that the device is not close to the threshold voltage for TF-SCLC.

From this data, we determine that this configuration does not exhibit ideal Schottky emission behaviour. The Poole-Frenkel gradient is half of that predicted from equation 32, although it is known from chapter 2 that in this case (where the Poole-Frenkel gradient matches the predicted slope for Schottky emission), we may be observing “modified Poole-Frenkel emission”. This suggests that either more trap centres are present as a result of the addition of a PMMA layer, or that the addition of PMMA reduces the number of donor centres. SCLC behaviour still appears to occur, although it is reduced compared to the Au/ZnO/Au configuration (the addition of PMMA only appears to show an Ohmic regime and a potential TC-SCLC regime, with no higher order regimes). This may also potentially be explained by an increase in the number of trap centres: with more trap centres to fill, a higher voltage is required in order to reach the trap-filled limit voltage threshold, and as such the higher-order regimes that occur as this limit is reached will also appear at higher voltages.

7.2 Gold (Au) Bottom Electrode with Aluminium (Al) Top Electrode

Figure 7.7 shows the Schottky behaviour of a device with Au/ZnO/Al configuration. The figure shows four images: one showing an entire sweep for that device; one showing an I-V curve demonstrating where the switching begins (importantly, the curve demonstrates an exponential increase in current at a threshold voltage, similar in behaviour to a Schottky diode); one showing a Schottky plot (ln J/T^2 vs $E^{1/2}$) across the full data range shown in the second image, and one showing only the non-linear component.

The two Schottky plots show a dotted fitting line, highlighting linear relationships between ln J/T^2 and $E^{1/2}$. This may indicate a Schottky emission contribution to the limitation of the current. The fitted line was added using the Quick Fit option in Origin 2015.

The extracted value for φ_B for this configuration is 0.72 eV. Al is not expected to form a Schottky contact with ZnO due to its work function being typically lower than the electron affinity of ZnO; however a thin layer of AlO_{2-x} or Al_2O_{3-x} may form at the interface due to Al being more reactive than ZnO, and this might result in the formation of a Schottky barrier due to the change in electron affinity. The slope for the “SET” sweep is almost twice that of the predicted slope of 0.0007, although for the “RESET” sweep the slope is very close to the predicted value. This suggests that Schottky emission may be a contributing transport mechanism for this configuration.

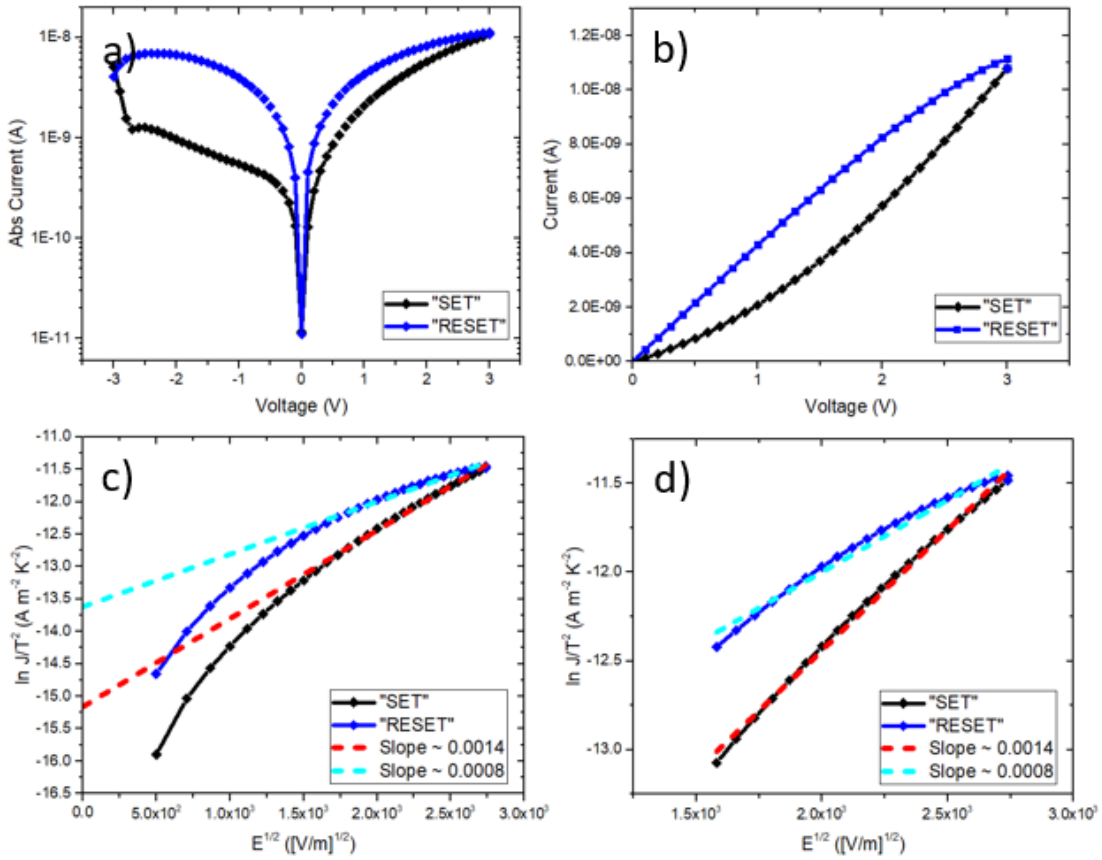

Fig. 7.7: A plot of ln J/T^2 vs $E^{1/2}$ for the nonlinear region of the 3 V I-V sweep of an Au/ZnO/Al device. While the fitted line follows the data very closely, suggesting that there is a strong Schottky emission component to the switching mechanism, in this case b) indicates that the device is not behaving like a Schottky diode, as the resistance prior to 1 V is low (~ 500 MΩ) compared to that expected of a Schottky diode (~ 0 Ω). The y-intercept for the "SET" sweep is -15.16.

Figure 7.8 shows the Poole-Frenkel analysis for an Au/ZnO/Al configuration; this is derived from the same data that was used in the Schottky plot in figure 7.7. As with the Au/ZnO/Au configuration, the data shows a linear relationship between ln (J/E) and $E^{1/2}$, indicating that a Poole-Frenkel emission mechanism may be in effect.

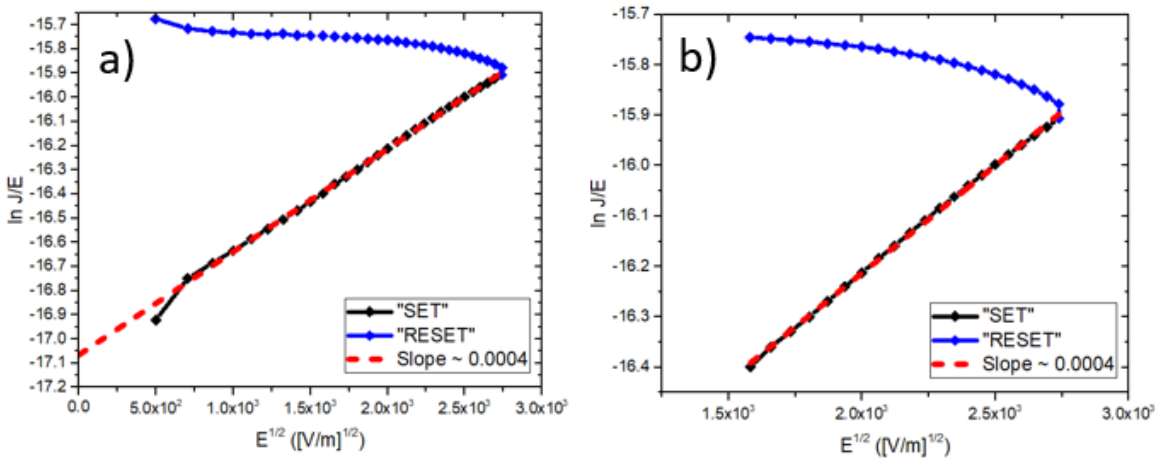

Fig. 7.8: A plot of ln *J/E* vs $E^{1/2}$ for the nonlinear region of the 3 V I-V sweep of the Au/ZnO/Al device shown in figure 7.2. This data shows a very smooth linear trend indicating a strong linear relationship between ln *J/E* and $E^{1/2}$. The y-intercept is -17.07.

The slope in this case is much smaller than the predicted value of 0.0015. This indicates that Poole-Frenkel emission may not be an appropriate model for the transport mechanism in this case. Interestingly, in the “RESET” sweep the Poole-Frenkel plot increases and ceases to be linear. It does not appear that this can be interpreted as Poole-Frenkel behaviour.

Figure 7.9 shows the SCLC characteristics for the Au/ZnO/Al device configuration. While the initial Ohmic conduction region (red) seems identifiable (where the slope is ~ 1), there is no region that can be identified as a trap-controlled SCLC region (where the slope would be expected to be ~ 2), and no higher-order regions. This suggests that any SCLC effects in this sample are quite negligible.

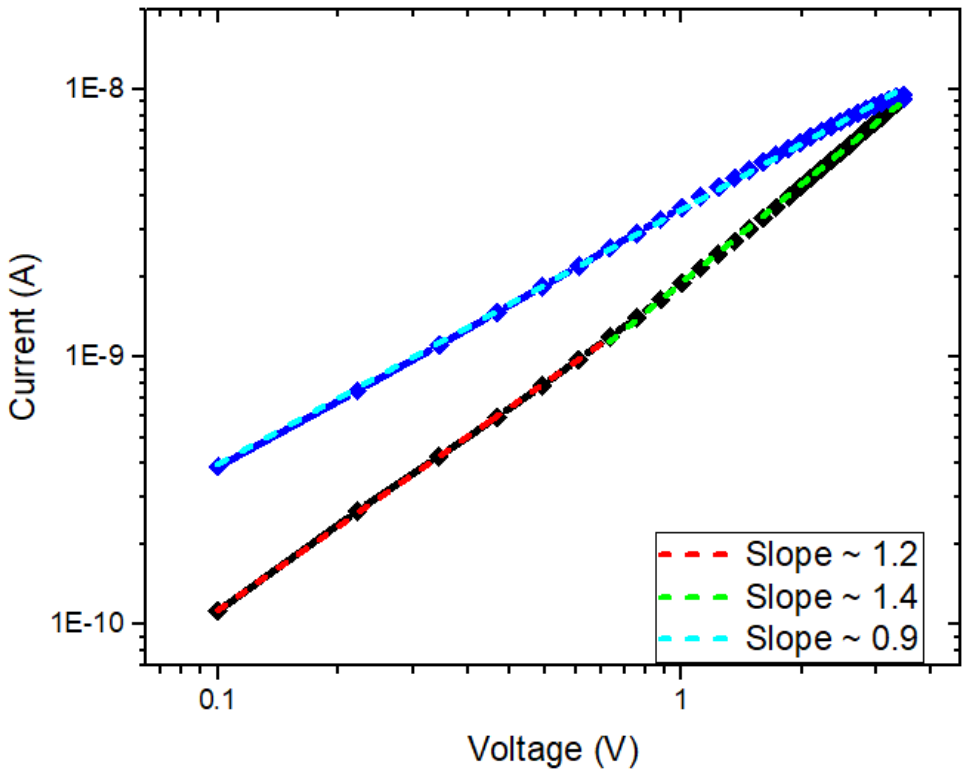

Fig. 7.9: I-V characterisation of an Au/ZnO/Al device, with respect to SCLC current.

While there appears to be an early Ohmic regime in figure 7.9, the slope never increases enough to sufficiently indicate TC-SCLC behaviour (slope ~ 2), suggesting that SCLC is not a significant contributor to electron transport in this configuration.

For this configuration, Schottky emission appears to be the closest fit out of the three models. The slope for the “SET” process is a little bit too high compared with the predicted slope (0.0014 compared with 0.0007), but the “RESET” process gives a slope (0.0008) that is very close to the expected value. In addition, the extracted value for φ_B of 0.72 eV may be explained by a potential formation of a thin layer of oxidised aluminium at the interface, which might create a

Schottky barrier with the Al (as ordinarily ZnO may be expected to form an Ohmic contact with Al). This, combined with the linear relationship between ln J/T^2 and $E^{1/2}$, suggest that Schottky emission behaviour may be present in this configuration. In contrast, while the Poole-Frenkel emission plots also show a linear relationship between ln J/E and $E^{1/2}$, the slope of the plot is 0.0004, which is lower than the expected value. This indicates that the ideal Poole-Frenkel emission model does not fit the data for this configuration. Likewise, no clear SCLC regimes can be observed, with only the Ohmic regions being observable.

7.2.1 With a PMMA Layer

Figures 7.10 – 7.12 show the Schottky, Poole-Frenkel and SCLC characteristics of a device made with Au/ZnO/PMMA/Al configuration.

Figure 7.10 shows the Schottky emission analysis for this configuration. A linear relationship can be observed between ln J/T^2 and $E^{1/2}$ in the “SET” sweep but not in the “RESET” sweep. The extracted value for φ_B is 0.68 eV. The Schottky barrier height may have arisen here as a result of the PMMA/Al interface forming a Schottky contact, although it is unclear, as the electron affinity for PMMA is typically ~ 0.6 eV and should form a large Schottky barrier, however methyl methacrylate radicals are found to have electron affinities that can be ~ 3.8 eV [*197*]; this would form a barrier with Al of ~ 0.48 eV, which the extracted value would be close to. However, 7.10b does not display clear Schottky diode-like behaviour. The slope of 0.0015 is also too

high compared with the expected gradient of 0.0007 predicted from equation 29. The “RESET” process does not appear to be linear in this region, and therefore does not fit Schottky emission behaviour. This information suggests that the configuration does not exhibit ideal Schottky emission.

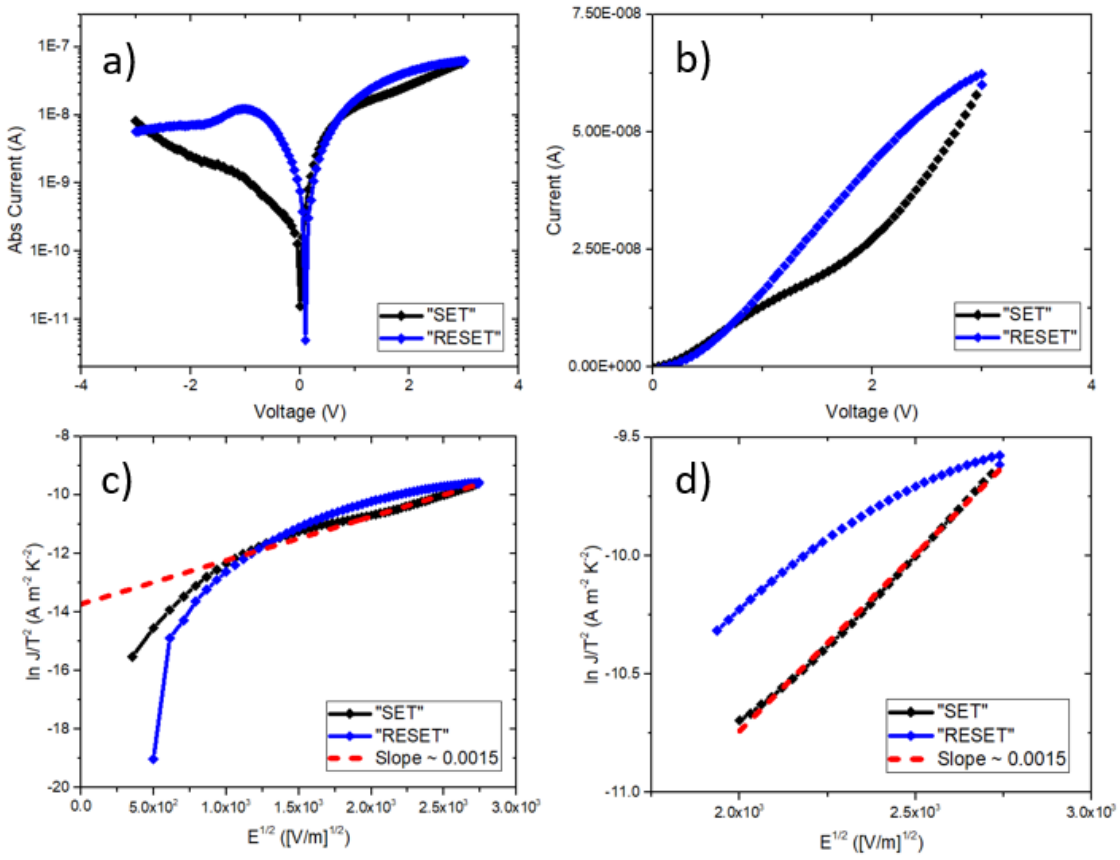

Fig. 7.10: A plot of ln J/T^2 vs $E^{1/2}$ for the nonlinear region of the 3 V I-V sweep of the Au/ZnO/PMMA/Al device: a) shows the full I-V sweep for the device, using a logarithmic y-axis with absolute current; b) shows the I-V curve only in the positive polarity region, and demonstrates that the resistance switching seems to occur at around 1 V; c) shows the Schottky plot (ln J/T^2 vs $E^{1/2}$) for the entire positive polarity region, while d) focuses on the nonlinear region from 1 V onwards where the switching is identified. The y-intercept is -13.73.

Figure 7.11 shows the Poole-Frenkel emission analysis for this configuration. No linear relationship is observed in this data, indicating that Poole-Frenkel is not contributing to the transport mechanism at this voltage polarisation.

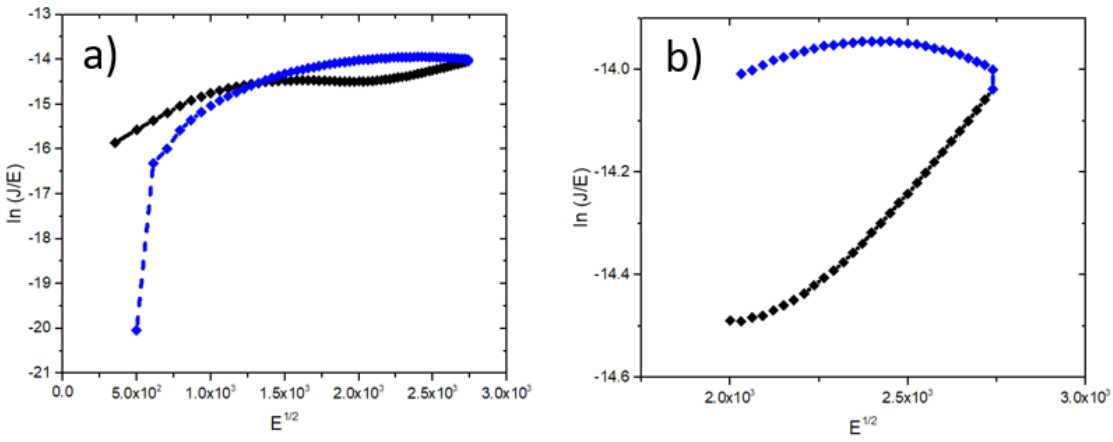

Fig. 7.11: A Poole-Frenkel plot of ln (*J*/*E*) vs $E^{1/2}$ for the nonlinear region of the 3 V I-V sweep of the Au/ZnO/PMMA/Al device. In the nonlinear region shown in figure 7.13 b), we see no corresponding linear relationship between ln (*J*/*E*) and $E^{1/2}$, suggesting that there is no Poole-Frenkel emission in this configuration.

Figure 7.12 shows the SCLC characteristics for this configuration. While some of the changes in slope observed might be attributable to SCLC behaviour, the initial slope (red) of ~ 1.48 does not fit the model. Indeed, the general behaviour observed in this plot does not seem representative of SCLC.

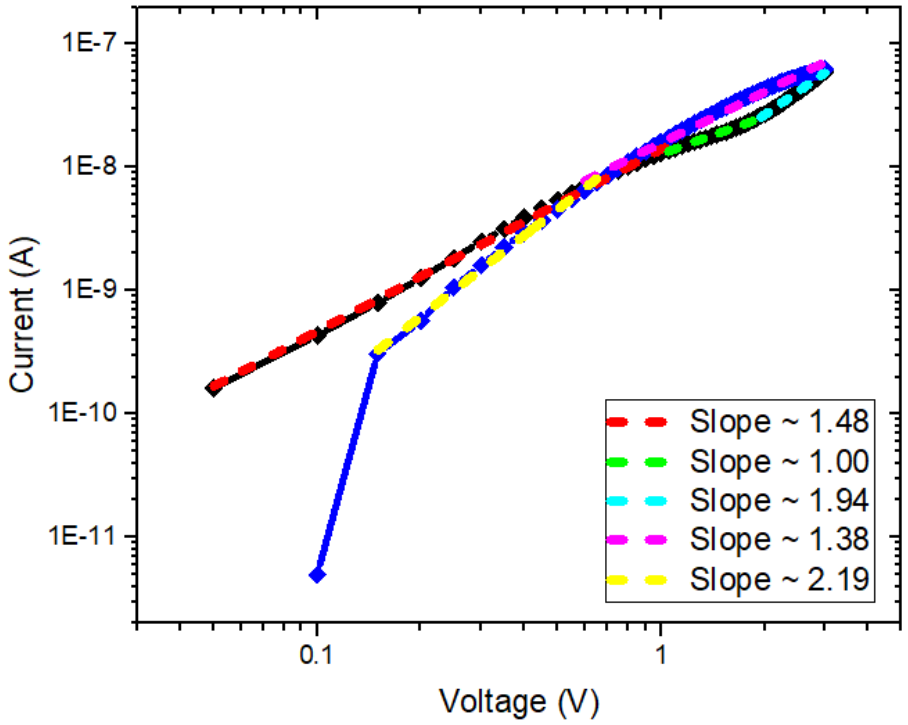

Fig. 7.12: I-V characterisation of an Au/ZnO/PMMA/Au device, with respect to SCLC current. The initial slope is too high for the characteristic Ohmic conduction region (which should have a slope of ~ 1), and while the cyan slope is close to 2 (which might indicate a TC-SCLC region), the preceding slope lines make this questionable, especially since there is little difference between the slope of the red region and that of the cyan region.

None of the models analysed properly fit the data for the Au/ZnO/PMMA/Al configuration. While a linear relationship is observed between ln J/T^2 and $E^{1/2}$ that could suggest a Schottky contribution, the information extracted from the gradient does not appear to agree with theoretical expectations. No linear relationship is observed between ln J/E and $E^{1/2}$, suggesting that the Poole-Frenkel emission model does not fit this data. The SCLC model also does not appear to fit, as the expected SCLC regime transitions (from Ohmic slope ~ 1, to TC-SCLC slope ~ 2, etc.) are not observed. The dominant transport mechanism here is unclear.

7.3 Indium Tin Oxide (ITO) Bottom Electrode with Aluminium (Al) Top Electrode

Figure 7.13 shows the Schottky behaviour of a device with ITO/ZnO/Al configuration. The figure shows four images: one showing an entire sweep for that device; one showing an I-V curve demonstrating where the switching begins (importantly, the curve demonstrates an exponential increase in current at a threshold voltage, similar in behaviour to a Schottky diode); one showing a Schottky plot (ln J/T^2 vs $E^{1/2}$) across the full data range shown in the second image, and one showing only the non-linear component.

The two Schottky plots show a dotted fitting line, highlighting linear relationships between ln J/T^2 and $E^{1/2}$. The fitted line was added using the Quick Fit option in Origin 2015.

The relationship between ln J/T^2 and $E^{1/2}$ for the ITO/ZnO/Al device are extremely similar to those of the Au/ZnO/Al device. This is because the polarity of the voltage shows the behaviour at the ZnO/Al interface. The change in y-intercept, however, gives an extracted value for φ_B of 0.5 eV, which matches the value expected from the electron affinity of ZnO and the work function of ITO. The “SET” and “RESET” slopes are 0.0013 and 0.0008 respectively, which are almost the same as for the Au/ZnO/Al device, with the latter being very close to the predicted value of 0.0007. This indicates that Schottky emission is a contributing mechanism in this configuration.

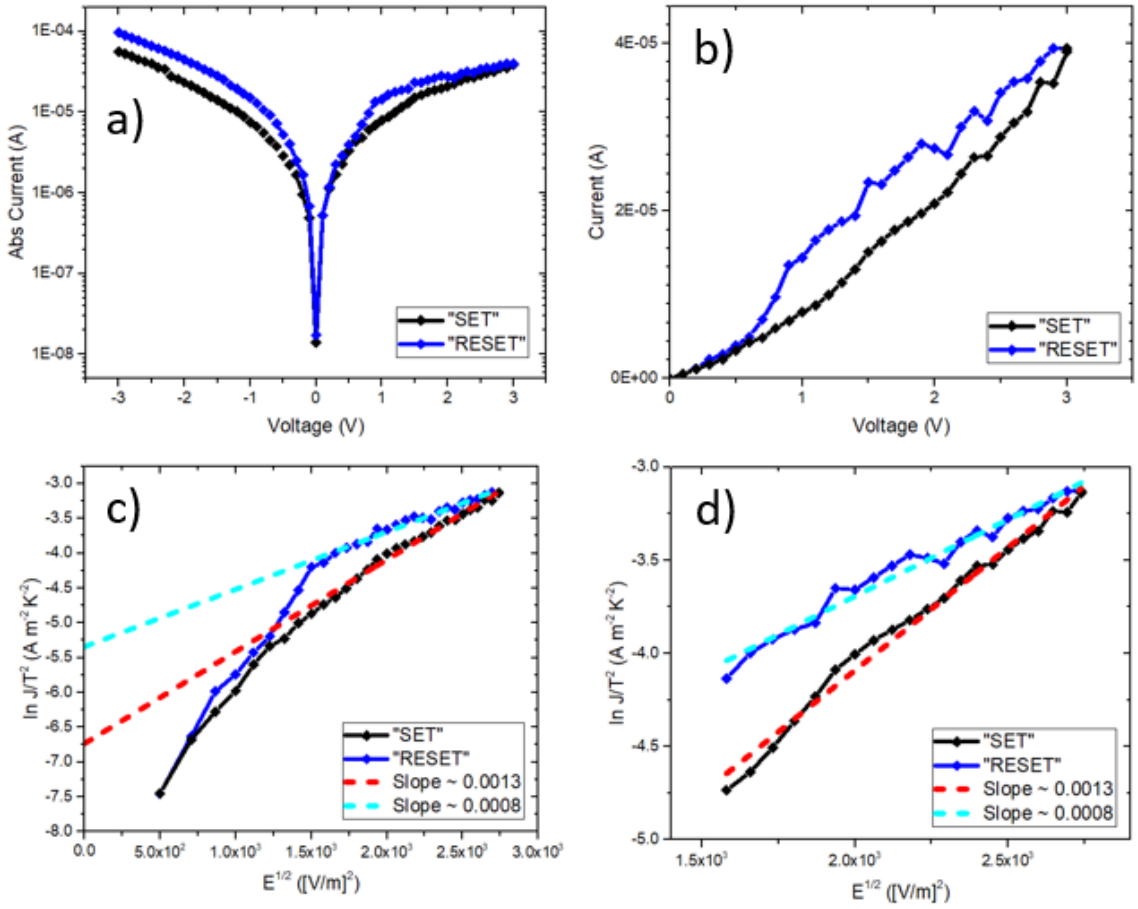

Fig. 7.13: A plot of ln *I* vs $V^{1/2}$ for the nonlinear region of the 3 V I-V sweep of an ITO/ZnO/Al device. The y-intercept of the "SET" fitting line is -6.736.

Figure 7.14 shows the Poole-Frenkel analysis for this ITO/ZnO/Al configuration; this is derived from the same data that was used in the Schottky plot in figure 7.13. There is a linear relationship observed between ln *J/E* and $E^{1/2}$ in the 1 V – 3 V region where switching is observed to occur, but no such relationship when the "RESET" sweep is applied. As with the Au/ZnO/Al device, the slope (0.0004) is lower than the expected slope of 0.0015; this seems to indicate that Poole-Frenkel emission does not contribute to the transport mechanism for this configuration.

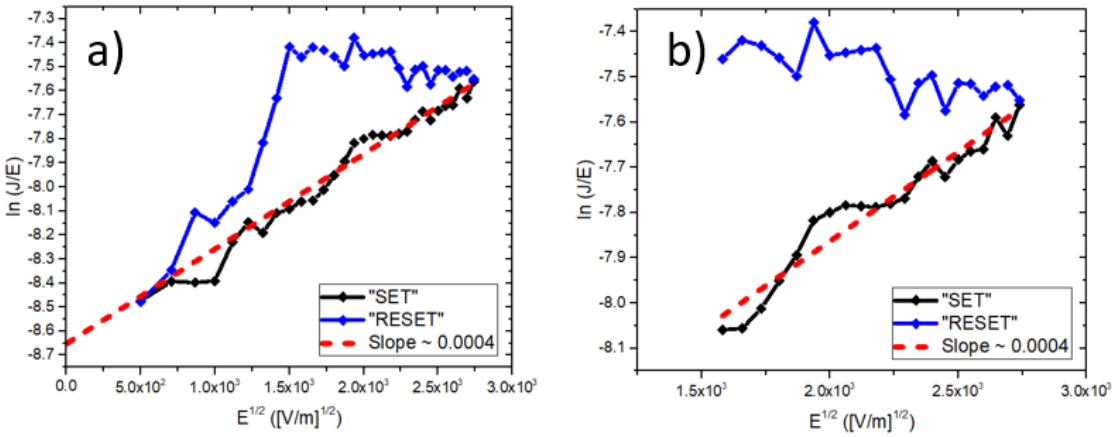

Fig. 7.14: A plot of ln (*J/E*) vs $E^{1/2}$ for the nonlinear region of the 3 V I-V sweep of the ITO/ZnO/Al device configuration. The y-intercept is -8.6531.

Figure 7.15 shows the SCLC profile for the ITO/ZnO/Al device. No recognisable SCLC regimes exist in this particular device.

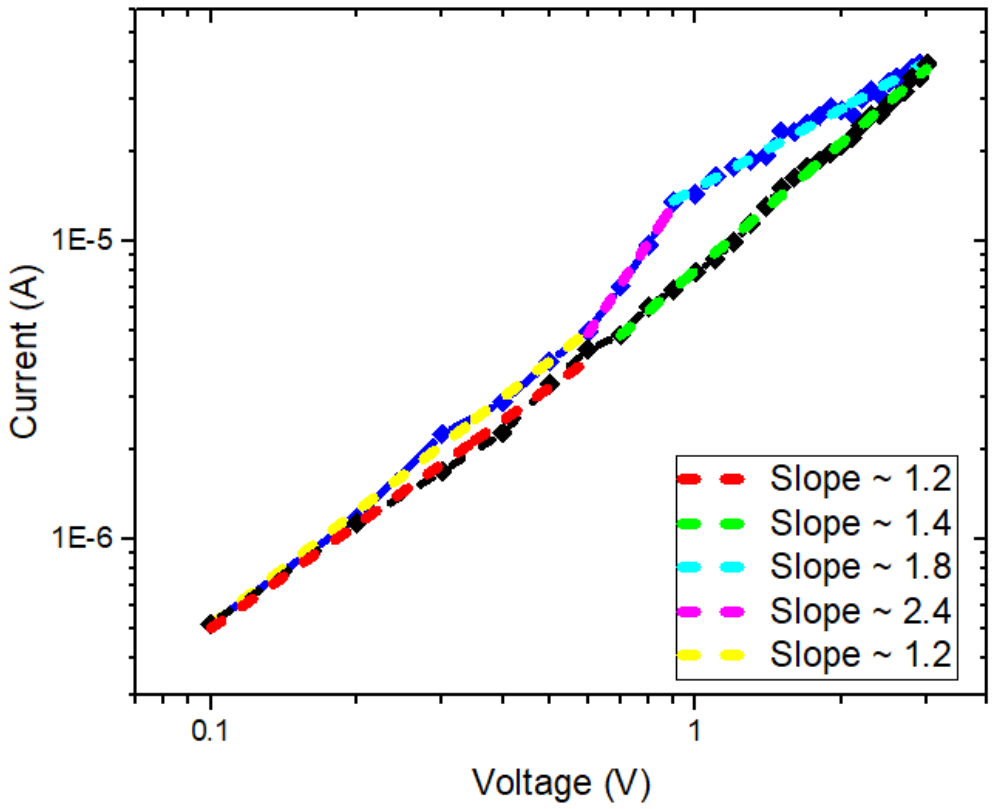

Fig. 7.15: I-V characterisation of an ITO/ZnO/Al device, with respect to SCLC current.

This configuration also exhibited no Poole-Frenkel emission behaviour, as can be seen in figure 7.14 above. Both Poole-Frenkel emission and SCLC are bulk-limited mechanisms dependent on traps, so the data may indicate that such mechanisms do not occur in ITO/ZnO/Al configurations, although more experimental data would be needed to confirm this, as well as the underlying reason.

This configuration (ITO/ZnO/Al) exhibits very similar behaviour to the Au/ZnO/Al configuration. This is due to the fact that at positive voltage polarity, the behaviour observed is that of the ZnO/Al interface. As this is common between the two devices, much of the behaviour, as indicated by the slopes for the two graphs, are the same between the two configurations. Because of this, it can be concluded that at the ZnO/Al interface, Schottky emission may contribute to the electron transport behaviour, while Poole-Frenkel and SCLC models do not fit the observed behaviour.

7.3.1 With a PMMA Layer

Figures 7.16 – 7.18 show the Schottky, Poole-Frenkel and SCLC characteristics of a device made with ITO/ZnO/PMMA/Al configuration. As discussed in Chapter 6, this configuration exhibits peculiar behaviour at around 1.8 V magnitudes, by which the current rapidly increases as the magnitude of the voltage increases above 1.8 V, and then decreases as the magnitude of the voltage decreases below 1.8 V. This unusual behaviour typically occurs in our devices when the HP 4140 B probes are applied to the top electrode in such a way as to cause excess pressure on the

device; as a result, the top electrode may be compressed into the PMMA layer, causing additional current paths to be formed at high voltages due to a narrowing of the barrier thickness at the PMMA/Al interface. Further experimentation is needed to gain a complete understanding of this effect, and whether it has controllable beneficial applications that can be exploited.

Figure 7.16 shows the Schottky emission plots for this configuration. The effect described above can be observed in the I-V sweep in 7.16 a). Because of this, it is unclear whether the highlighted region truly demonstrates Schottky behaviour.

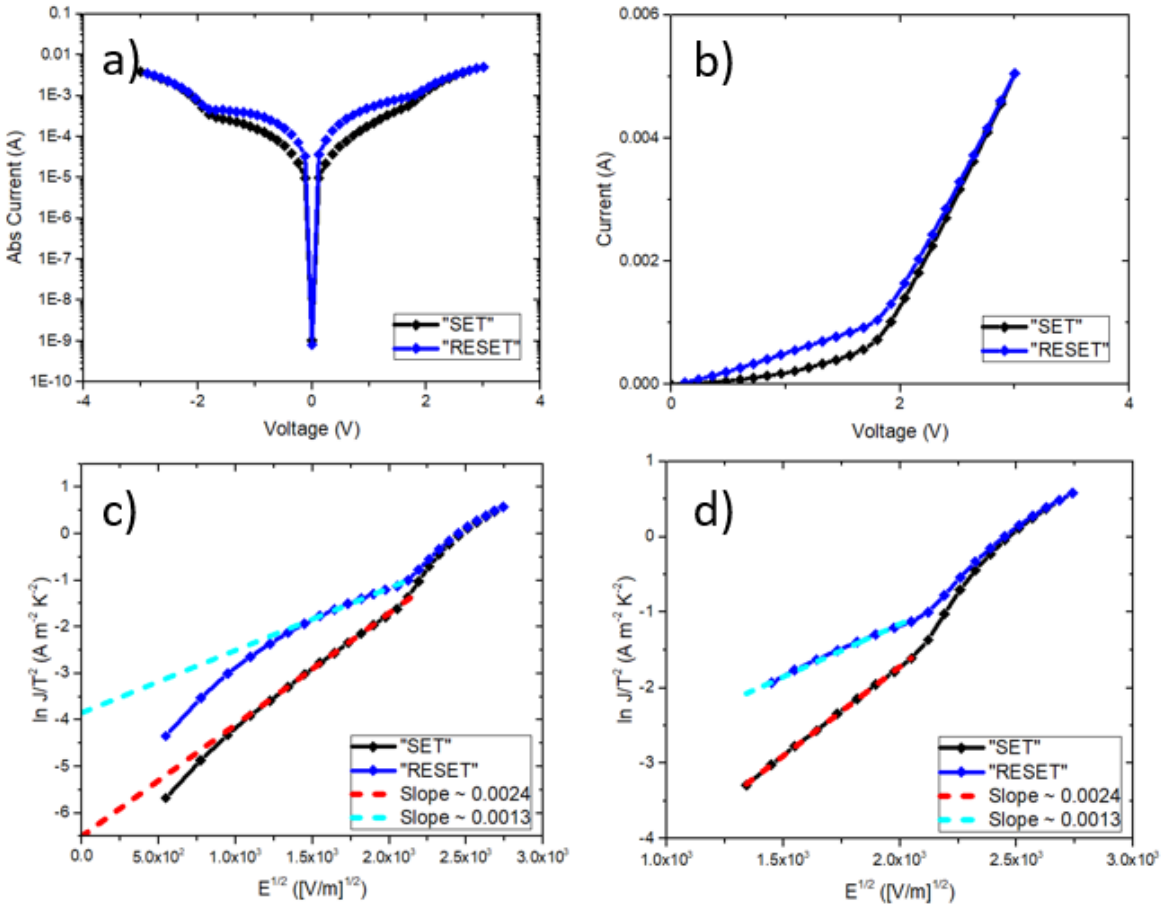

Fig. 7.16: A plot of ln J/T^2 vs $E^{1/2}$ for the nonlinear region of the 3 V I-V sweep of an ITO/ZnO/PMMA/Al device. The y-intercept is -6.502.

The extracted value for φ_B is 0.5 eV, which is identical to that of the device without PMMA, while the slope is now even greater (0.0024 for “SET” and 0.0013 for “RESET”, instead of 0.0013 for “SET” and 0.0008 for “RESET”). The identical barrier height might suggest that Al atoms are diffusing into the PMMA and interacting directly with the ZnO, or that pressure from the HP 4140 B V-output probe may be compressing the PMMA and allowing direct contact between the electrode and the ZnO. The increased slope may suggest that Schottky emission is not present in this configuration.

Figure 7.17 shows the Poole-Frenkel analysis for an ITO/ZnO/PMMA/Al configuration; this is derived from the same data that was used in the Schottky plot in figure 7.16.

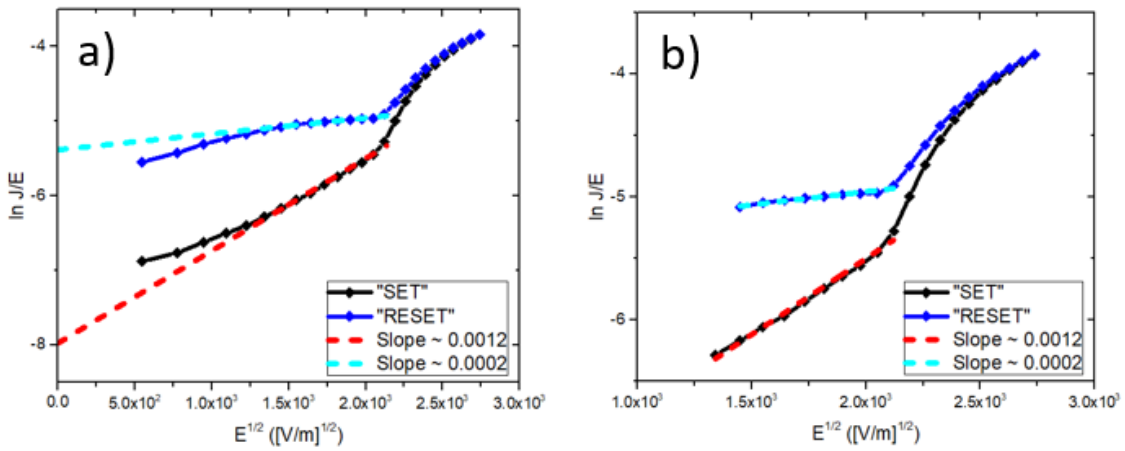

Fig. 7.17: A plot of ln (J/E) vs $E^{1/2}$ for the nonlinear region of the 3 V I-V sweep of the ITO/ZnO/Al device configuration. The y-intercept for the “SET” line is -7.977.

The slope of 0.0012 is close to the predicted value of 0.0015, suggesting that Poole-Frenkel emission may be occurring in the “SET” process. The slope of 0.0002 for the “RESET” process is much too low, suggesting that the change in resistance state may come as a result in a significant change of transport mechanism.

Figure 7.18 shows the SCLC profile for the ITO/ZnO/Al device.

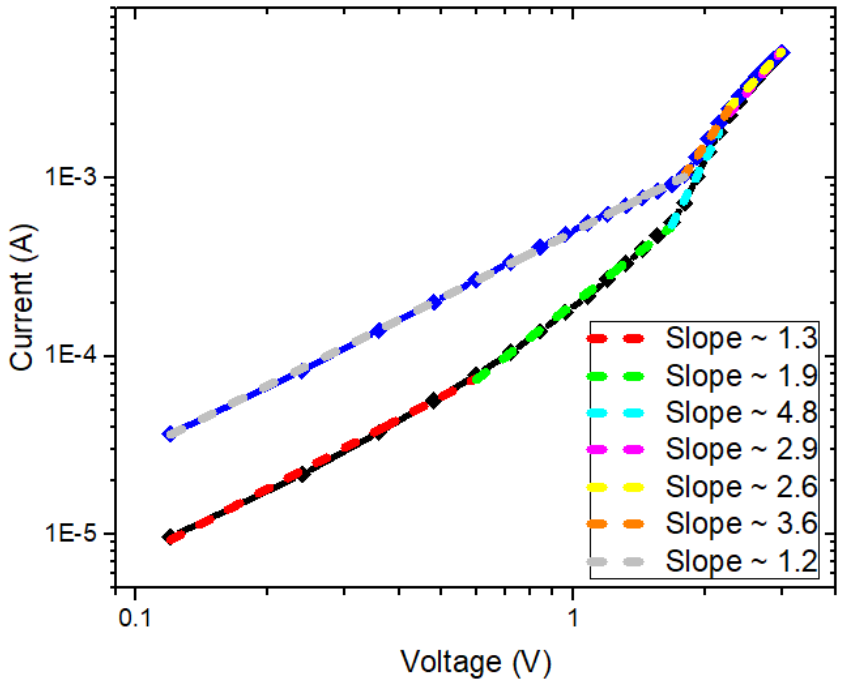

Fig. 7.15: I-V characterisation of an ITO/ZnO/PMMA/Al device, with respect to SCLC current. The slope highlighted by the red fitted line is marginally greater than is expected from the Ohmic conduction region, where the slope would be expected to be ~ 1. A TC-SCLC region is observed (slope ~ 2) and a higher-order region (slope ~ 5). In addition, a region with a slope of ~ 2.9 is observed; this may be close to the TF-SCLC, which has not been observed in any other configurations of our devices.

The plot reveals the Ohmic (slope ~ 1), TC-SCLC (slope ~ 2) and trap charge limited conduction (slope > 2) regions that indicate that this configuration exhibits SCLC

behaviour. In addition, a fourth regime arises, highlighted as a region with a slope of ~ 2.9. This is higher than the slope of ~ 2 that would be expected to reappear when the device is in TF-SCLC, although may be indicative of the device entering this regime. Similar behaviour is observed in reverse when the “RESET” sweep is applied; it is unclear what this means, as the overall behaviour may indicate SCLC transport, while the behaviour for the “RESET” process may indicate that any SCLC is not a result of memristive behaviour.

For the ITO/ZnO/PMMA/Al configuration, we observe that the Schottky emission data produces an extracted value of φ_B that is identical to that of the ITO/ZnO/Al device (0.5 eV), although the slope (0.0024) is much higher than the expected value (0.0007). This makes it unlikely that Schottky emission is taking place, which is a significant change in comparison to the ITO/ZnO/Al device. The Poole-Frenkel model does seem to fit better than for our other configurations, with a slope of 0.0012, close to the predicted slope of 0.0015. The SCLC model also appears to fit reasonably, with multiple SCLC regimes observable in the plot. However, it is unclear as to why this particular configuration exhibits this behaviour compared with the ITO/ZnO/Al device.

7.4 Summary

We see that, not only does the on/off ratio and the voltage required to initiate switching depend on the electrodes that you use (as seen in chapter 6), but also that different electrode materials seem to favour different transport mechanisms.

Au/ZnO/Au device configurations appear to favour trap-based bulk-limited transport mechanisms, as both Poole-Frenkel emission and SCLC models fit the data well; the Schottky emission model produces a value for the Schottky barrier height that is a close match to the theoretical barrier height predicted using the work function of Au and the electron affinity of ZnO, but the slope does not match closely to the predicted slope of 0.0007. Au/ZnO/PMMA/Au devices also do not fit the Schottky model, and the slope from the Poole-Frenkel model indicates that the configuration may exhibit the “modified Poole-Frenkel effect”. The SCLC plot shows that, while the initial Ohmic region and the TC-SCLC region can still be observed, the higher-order trap charge limited conduction region is lost. This, alongside the information from the Poole-Frenkel plot, suggest the possibility of additional trap centres being formed in this configuration compared to the configuration without PMMA.

Au/ZnO/Al device configurations appear to potentially favour Schottky emission as the dominant mechanism, at the ZnO/Al interface; neither Poole-Frenkel nor SCLC models fit the data. The “SET” slope appears to be too large to indicate ideal Schottky emission behaviour, while the “RESET” slope seems to fit the ideal model much more closely. When PMMA is added, none of the three models appear to fit the data well at all.

ITO/ZnO/Al device configurations have similar behaviour at the voltage polarities analysed, due to the fact that this voltage polarity shows the behaviour at the ZnO/Al interface. The Schottky plot allows the extraction of a value for the Schottky barrier height of 0.5 eV, which matches the expected value; in addition, as with the

Au/ZnO/Al configuration, the “SET” gradient is too high for ideal Schottky emission (almost double), but the “RESET” gradient matches very closely to the expected value of 0.0007. The Poole-Frenkel model does not fit the data well, and SCLC also appears unlikely as the TC-SCLC regime is not observed. However, when a PMMA layer is added, the SCLC model fits the data much better, showing Ohmic, TC-SCLC and higher-order regimes, and the Poole-Frenkel plot for the “SET” process shows a slope (0.0012) that is close to the predicted value of 0.0015, suggesting that Poole-Frenkel emission may contribute; the Schottky model does not fit the data for the ITO/ZnO/PMMA/Al configuration.

Figure 7.19 shows a table identifying the observed transport mechanisms for each of the tested device configurations.

Configuration	Schottky	Poole-Frenkel	SCLC	Notes
Au/ZnO/Au	No	Yes	Yes	
Au/ZnO/PMMA/Au	No	Yes (modified)	Yes*	Only Ohmic and TC-SCLC observed
Au/ZnO/Al	Yes	No	No	
Au/ZnO/PMMA/Al	No	No	No	
ITO/ZnO/Al	Yes	No	No	
ITO/ZnO/PMMA/Al	No	Yes	Yes	

Fig. 7.19: A table identifying the transport mechanisms observed for the device configurations tested.

Chapter 8

Conclusions and Future Work

This chapter summarizes the work that has been carried out as part of this thesis and highlight the key points that have been discussed. Key findings from Chapters 5 – 7 will be revisited.

The potential for continuation of the project will be discussed, focusing on the work that has not yet been completed as well as other potential future work that has yet to begin.

Finally, a concluding statement shall be given, returning to the objectives of the project and questioning whether those objectives have been adequately met.

8.1 Summary of Results and Discussion

In Chapter 5, the results of a study into the growth of nanorods via a microwave-assisted hydrothermal process were presented. It was found that, to produce uniform nanorods that are densely distributed and well-aligned perpendicular to the substrate, a high-quality seed layer should first be deposited. Our method, comprised of spin coating a 10 mM seed solution of zinc acetate dihydrate dissolved in propan-1-ol three times onto the substrate, and then annealing at 350°C after each anneal [*59*], produces a uniform seed layer, with seeds of ~50 nm diameter and about 5 nm height.

Annealing at lower temperatures can also produce a uniform layer of aligned nanorods; however, we find that temperatures below 150°C are not enough to align the seeds, and thus the nanorods are not properly structured. Higher annealing temperatures for the seed layer are reported to improve the crystallinity of the nanorods produced [*165*].

The growth step itself was also studied. It was found that the rate of heating the growth solution (an equimolar solution of zinc nitrate hexahydrate and hexamethylenetetramine dissolved in deionized water) could cause large, undesirable crystallites to form on the surface of the sample. Where this occurs, large dark patches typically become visible on the SEM; these patches typically appear where the nanorod film becomes damaged (such as where scratches are left by the tweezers after contact), or where nanorods have not formed, as in both

cases the nanorod layer produces a stronger signal than the deeper background regions. It is believed that ZnO nanostructures and crystals form via a ripening process, similar to Ostwald ripening [*174*], and that the inclusion of a capping agent (such as HMTA) in the growth solution can limit the effect of the ripening process [*175*], ensuring that nanorods dominate the growth. Our results show that rapid growth at high power increases the number of larger crystal structures to form, which we propose to be the result of a shift in the equilibrium of the hydroxyl reaction causing more OH^- ions to be produced and precipitating out more of the Zn^+ ions as a result.

It is observed that crystallites form in the early stages of nanorod growth, as shown in figure 5.13. XRD shows that the nanorods are aligned in the (002) direction, which is perpendicular to the substrate. It is also identified, both through SEM images and the information from the XRD, that the nanorods have the hexagonal wurtzite structure. Large crystallites with no nanorods in the background are too sparsely distributed across the substrate surface to give sufficient signal, and as such it is difficult to obtain detailed structural information from them.

In Chapter 6, electrical measurement data was presented that was used to develop an understanding of the role of each of the components of the memristor devices. It was found that the electrode materials are very important, and the combination of electrodes used is key in optimizing the behaviour of the devices. Samples with Au bottom electrodes and Al top electrodes appear to have the largest on/off ratios, although the on/off ratios of all devices are typically only ~ 10 at best.

The different electrode combinations and the addition of the PMMA layer also appear to have a direct effect on the mechanisms that cause the switching behaviour. Au/ZnO/Au and Au/ZnO/PMMA/Au configurations exhibit SCLC behaviour in the corresponding plots (I vs V on logarithmic axis scales for both axes), although the addition of a PMMA layer removes the trap charge limited conduction region (where the slope of the plot is > 2) that is observed in the Au/ZnO/Au configuration. Neither Au/ZnO/Au nor Au/ZnO/PMMA/Au seem to clearly exhibit Schottky emission behaviour, in spite of the linear relationship between ln J/T^2 and $E^{1/2}$, as the slope of the plot (0.0033) is much higher than that predicted (0.0007), although the extracted barrier height of 0.81 eV closely matches the expected value of 0.8 eV. The Poole-Frenkel plot for Au/ZnO/Au fits the ideal model very closely for the "RESET" state, with a slope of 0.0016 compared with the predicted value of 0.0015, although the "SET" state has a slope of 0.0024 which is too high for ideal Poole-Frenkel behaviour. Both the "SET" and "RESET" slopes for the Au/ZnO/PMMA/Au have very similar gradients (0.0007 and 0.0006 respectively), which are half of the expected gradient for normal Poole-Frenkel emission and equal the expected slope of Schottky emission, indicating that this configuration might be exhibiting "modified Poole-Frenkel emission" as described in chapter 2, where the number of trap centres, N_t, is approximately equal to the number of donor states, N_d. This, alongside the SCLC data, suggests that the addition of a PMMA layer may create additional trap centres, thus increasing V_{TFL}, the threshold voltage at which all traps are filled in the SCLC model.

Au/ZnO/Al devices appear to exhibit Schottky emission behaviour (the slope for the “RESET” process is 0.0008, close to the predicted value of 0.0007, although the “SET” slope is higher than expected for ideal Schottky emission) but do not clearly exhibit Poole-Frenkel or SCLC; the addition of a PMMA layer diminishes the separation between the “ON” and “OFF” states, and none of the transport models tested fit the data well.

The ITO/ZnO/Al configuration exhibits similar Schottky behaviour compared with the Au/ZnO/Al configuration, with the same slopes for the “SET” and “RESET” processes; the data also allows the extraction of a value for the barrier height of 0.5eV, which matches the predicted value. This configuration does not exhibit Poole-Frenkel emission behaviour, and also does not exhibit the TC-SCLC regime that would indicate SCLC. ITO/ZnO/PMMA/Al devices do not appear to exhibit Schottky emission behaviour; their SCLC plot, however, shows SCLC regimes that the device without PMMA does not reveal. In addition, the Poole-Frenkel data for the “SET” process shows a gradient of 0.0012, close to the predicted value of 0.0015, suggesting that both Poole-Frenkel emission and SCLC take place in this configuration.

Carrying out measurements in a nitrogen environment instead of air causes the devices to no longer exhibit hysteresis effects. This has been proposed [*128*] to be a result of a lack of oxygen to adsorb onto the oxygen vacancies left as a result of oxygen ions migrating into the bulk in the presence of a forward bias.

The endurance and retention data gathered thus far suggests that devices will currently struggle to handle more than 10,000 cycles without the resistances of the devices gradually decaying to a level where, although the two states remain distinguishable from one another in the majority of cases, they are not clearly distinguishable from one device to the next. As such, more work is needed to optimize the devices before they could be commercialized (commercial memristors aim to survive > 100,000 cycles, with retention durations measured in years).

8.2 Future Work

Much work remains before the devices produced by the methods detailed in this thesis are optimized enough to be considered for commercial use. Some key experiments would allow for greater understanding of the functions of the devices and more depth of understanding of the roles of each of the materials.

Primarily, the significance of the nanorods themselves must be further addressed. Nanorods are known to have advantages over thin films, in that individual nanorods with high aspect ratios will generate enhanced electric fields at the tips when a voltage is applied to them, and that they are able to operate as a switching layer even when the nanorod thickness is large (in the order of microns). They are also able to be fabricated at low cost, with simple techniques. A detailed study into the differences in behaviour of nanorods, thin films, and nanoparticle films would provide greater insight into the mechanisms involved in the switching behaviour, and allow for the identification of further advantages of the use of nanorods. This study

has already begun; however, unfortunately not enough results have been obtained to include in this thesis.

To further identify the dominant switching mechanisms for each configuration of memristor device, the effect of varying temperature on the switching behaviour needs to be investigated. Schottky emission and Poole-Frenkel emission are both temperature-dependent mechanisms, and it is important to carry out the temperature study in order to confirm that these mechanisms are indeed occurring, and to identify whether specific temperatures (for example, the typical operating temperatures of a CPU) would damage the devices.

Many of the switching mechanisms ascribed to ZnO as a material rely upon the presence (or absence) of oxygen vacancies. The rapid hydrothermal growth method is known to create defects in the nanorods; a study into the formation of defects in the nanorods and the effect of those defects on the switching behaviour would further develop understanding of the role of the switching material itself.

Critically, more endurance and retention measurements need to be taken to ascertain whether the method is suitable for mass-production of commercial memristors. At present, we do not have enough data to truly estimate the endurance of the devices, and it is known that metal oxides have issues with poor retention times and unreliable behaviour from one device to another. Refinement of our method may be able to solve the problem that others have struggled to solve.

8.3 Conclusions

Memristors are no longer a new technology, yet there are still many unanswered questions that stand in the way of full, public commercialization. One problem is cost; Flash is currently the market's dominant non-volatile memory technology and is a multi-billion-dollar market known across the globe, and replacing that technology is very risky. The capability to produce a cheaper alternative, that is also simpler to produce, would be a strong incentive to further invest in the newer technology.

We proposed a low-cost, microwave-assisted growth method of producing ZnO nanorods as part of a cost-effective fabrication method for memristors. These devices have produced some promising results, including ease of switching without needing a forming step, and switching at low voltages with low switching currents. While more work is needed to optimize the devices, in particular to improve endurance and state retention, this early-stage development and characterization of a simple, cost-effective material-hybrid memristor may have the potential to become the universal memory the scientific community has been searching for.

References

[1] N. R. Kadlec J, NAND Flash Memory Organization and Operations. *J. Inf. Technol. Softw. Eng.* **05** (2015), doi:10.4172/2165-7866.1000139.

[2] C. Preimesberger, NAND Flash Memory: 25 Years of Invention, Development - Data Storage - News & Reviews - eWeek.com. *eWeek.com* (2012), (available at http://www.eweek.com/c/a/Data-Storage/NAND-Flash-Memory-25-Years-of-Invention-Development-684048/).

[3] J. Cooke, in *Flash Memory Summit* (2007; http://cushychicken.github.io/assets/cooke_inconvenient_truths.pdf), pp. 1–32.

[4] K. O'Brien, D. C. Salyers, A. D. Striegel, C. Poellabauer, Power and performance characteristics of USB flash drives. *2008 IEEE Int. Symp. A World Wireless, Mob. Multimed. Networks, WoWMoM2008* (2008), pp. 1–4.

[5] S. A. Wolf, J. Lu, M. R. Stan, E. Chen, D. M. Treger, The promise of nanomagnetics and spintronics for future logic and universal memory. *Proc. IEEE*. **98**, 2155–2168 (2010).

[6] L. Chua, Memristor - the missing circuit element. *IEE Trans. Circuit Theory*. **18**, 507–519 (1971).

[7] T. Prodromakis, C. Toumazou, L. Chua, Two centuries of memristors. *Nat.*

Mater. **11**, 478–481 (2012).

[8] H. Davy, Elements of chemical philosophy. *Bradford and Inskeep* (1812), p. 326.

[9] H. Davy, Additional Experiments on Galvanic Electricity. *Nicholson's J. Nat. Philos. Chem. Arts*. **IV**, 326–328 (1800).

[10] S. Y. H. D. Lin, L. Chua, The First Man-Made Memristor: Circa 1801 (Scanning Our Past). *Proc. IEEE*. **103**, 131–136 (2015).

[11] B. Widrow, An Adaptive "Adaline" Neuron Using Chemical "Memistors." *Stanford Electron. Lab. Tech. Rep.* (1960), pp. 1553–2.

[12] G. E. Moore, Cramming more components onto integrated circuits. *Proc. IEEE*. **86**, 82–85 (1998).

[13] B. Mouttet, Memistors , Memristors , and Memresistors. *Memresistor Version 25* (2014), pp. 1–7.

[14] J. G. Simmons, R. R. Verderber, New Conduction and Reversible Memory Phenomena in Thin Insulating Films. *Proc. R. Soc. A Math. Phys. Eng. Sci.* **301**, 77–102 (1967).

[15] T. E. of E. Britannica, Trap Solid-State Physics. *Encycl. Br. Online* (2016), (available at https://www.britannica.com/science/trap-solid-state-physics).

[16] E. W. Weisstein, Hysteresis effect. *Eric Weisstein's World Phys.* (2017),

(available at http://scienceworld.wolfram.com/physics/HysteresisEffect.html).

[17] W.-K. Chen, *The Electrical Engineering Handbook* (Elsevier, 1997; http://books.google.com/books?hl=en&lr=&id=qP7HvuakLgEC&oi=fnd&pg=PA2&dq=The+Electrical+Engineering+Handbook&ots=X-q10UDfI4&sig=tsgqNogPB6dnc4jM07QTjtrvwBA).

[18] S. M. K. L. O. Chua, Memristive Devices and Systems..pdf. *Proc. IEEE*. **64**, 209–223 (1976).

[19] R. Marani, G. Gelao, A. G. Perri, A review on memristor applications. *Int. J. Adv. Eng. Technol.* **8**, 294–305 (2015).

[20] S. R. O. R. R. Johnson, Method for making, parallel preprogramming or field programming of electronic matrix arrays (2009), pp. 1–15.

[21] R. S. W. D. B. Strukov, G. S. Snider, D. R. Stewart, The Missing Memristor Found. *Nature*. **453**, 80–83 (2008).

[22] ETHW.org, Memristor. *Eng. Technol. Wiki*, (available at http://ethw.org/Memristor).

[23] J. B. A. B. Widrow, W. H. Pierce, Birth, Life, and Death in Microelectronic Systems. *IRE Trans. Mil. Electron.*, 191–201 (1961).

[24] R. S. Williams, A short history of memristor development. *Report* (2012), pp. 1–5.

[25] L. O. Chua, Resistance switching memories are memristors.pdf. *Appl. Phys. A - Mater. Sci. Process.* **102**, 765–783 (2011).

[26] J. C. Sankey *et al.*, Measurement of the spin-transfer-torque vector in magnetic tunnel junctions. *Nat. Phys.* **4**, 67–71 (2008).

[27] B. F. Lu, W. Cai, Y. Zhang, ZnO Hierarchical Micro / Nanoarchitectures : Solvothermal Synthesis and Structurally Enhanced Photocatalytic Performance *. *Adv. Funct. Mater.* **18**, 1047–1056 (2008).

[28] G. T. T. A. Krajewski, G. Luka, L. Wachnicki, R. Jakiela, B. Witkowski, E. Guziewics, M. Godlewski, N. Huby, Optical and electrical characterization of defects in zinc oxide thin films grown by atomic layer deposition. *Opt. Appl.* **39** (2009).

[29] R. N. Tiwari, R. N. Tiwari, K. S. Kim, Zero-dimensional, one-dimensional, two-dimensional and three-dimensional nanostructured materials for advanced electrochemical energy devices. *Prog. Mater. Sci.* **57**, 724–803 (2012).

[30] R. Koole, E. Groeneveld, D. Vanmaekelbergh, A. Meijerink, C. de M. Donegá, *Size Effects on Semiconductor Nanoparticles* (Springer, 2014; http://link.springer.com/10.1007/978-3-662-44823-6).

[31] Y. Zhang, M. K. Ram, E. K. Stefanakos, D. Y. Goswami, Synthesis, characterization, and applications of ZnO nanowires. *J. Nanomater.* **2012**

(2012), doi:10.1155/2012/624520.

[32] Y. Zhang, ZnO Nanostructures: Fabrication and Applications. *Nanosci. Nanotechnol. Ser.* **43**, 8–9 (2017).

[33] A. H. Adl, thesis, University of Alberta (2016).

[34] L. E. Greene, B. D. Yuhas, M. Law, D. Zitoun, P. Yang, Solution-grown zinc oxide nanowires. *Inorg. Chem.* **45**, 7535–7543 (2006).

[35] Q. Li *et al.*, Fabrication of ZnO Nanorods and Nanotubes in Aqueous Solutions. *Chem. Mater.* **17**, 1001–1006 (2005).

[36] G. D. Yuan *et al.*, p-Type ZnO Nanowire Arrays 2008. *Nano Lett.* **8**, 2591–2597 (2008).

[37] Y. Qin, X. Wang, Z. L. Wang, Microfibre-nanowire hybrid structure for energy scavenging. *Nature*. **457**, 340 (2009).

[38] H. E. Unalan *et al.*, Rapid synthesis of aligned zinc oxide nanowires. *Nanotechnology*. **19**, 1–5 (2008).

[39] W. G. Yang, F. R. Wan, S. W. Chen, C. H. Jiang, Hydrothermal Growth and Application of ZnO Nanowire Films with ZnO and TiO2 Buffer Layers in Dye-Sensitized Solar Cells. *Nanoscale Res. Lett.* **4**, 1486–1492 (2009).

[40] J. Cheng, X. Zhang, Z. Luo, Aligned ZnO nanorod arrays fabricated on Si substrate by solution deposition. *Phys. E*. **31**, 235–239 (2006).

[41] P.-C. Chang, C.-J. Chien, D. Stichtenoth, C. Ronning, J. G. Lu, Finite size effect in ZnO nanowires. *Appl. Phys. Lett.* **90**, 113101 (2007).

[42] X. Jiang, F. L. Wong, M. K. Fung, S. T. Lee, X. Jiang, Aluminum-doped zinc oxide films as transparent conductive electrode for organic light- emitting devices Aluminum-doped zinc oxide films as transparent conductive electrode for organic light-emitting devices. *Appl. Phys. Lett.* **1875**, 2001–2004 (2013).

[43] K. Ellmer, A. Klein, R. Bernd, in *Springer Series in Materials Science 104* (Springer-Verlag Berlin Heidelberg, 2007; http://books.google.ch/books/about/Transparent_Conductive_Zinc_Oxide.html?id=7WELet9RU5IC&pgis=1%5Cnhttp://library.wur.nl/WebQuery/clc/1239985#).

[44] K. Ellmer, Magnetron sputtering of transparent conductive zinc oxide relation between the sputtering. *J. Phys. D. Appl. Phys.* **33**, R17–R32 (2000).

[45] M. Chen, Z. L. Pei, X. Wang, C. Sun, L. S. Wen, Structural, electrical, and optical properties of transparent conductive oxide ZnO:Al films prepared by dc magnetron reactive sputtering. *J. Vac. Sci. Technol. A Vacuum, Surfaces, Film.* **19**, 963–970 (2001).

[46] A. Yamada, B. Sang, M. Konagai, Atomic layer deposition of ZnO transparent conducting oxides. *Appl. Surf. Sci.* **112**, 216–222 (1997).

[47] A. Kumar, Y. Rawal, M. S. Baghini, in *2012 International Conference on Emerging Electronics, ICEE 2012* (2012), pp. 1–3.

[48] M. Lanza, A Review on Resistive Switching in High-k Dielectrics: A Nanoscale Point of View Using Conductive Atomic Force Microscope. *Materials (Basel).* **7**, 2155–2182 (2014).

[49] K. Y. J. Park, S. Lee, J. Lee, A Light Incident Angle Switchable ZnO Nanorod Memristor: Reversible Switching Behaviour Between Two Non-Volatile Memory Devices. *Adv. Mater.* **25**, 6423–6429 (2013).

[50] Y. C. C. Huang, J. Huang, C. Lai, H. Huang, S. Lin, Manipulated Transformation of Filamentary and Homogeneous Resistive Switching on ZnO Thin Film Memristor With Controllable Multistate. *ACS Appl. Mater. Interfaces*. **5**, 6017–6023 (2013).

[51] H. Ryu *et al.*, ZnO sol – gel derived porous film for CO gas sensing. *Sensors Actuators, B Chem.* **96**, 717–722 (2003).

[52] S. Sabir, M. Arshad, S. K. Chaudhari, Zinc Oxide Nanoparticles for Revolutionizing Agriculture. *Sci. world J.* **2014**, 1–8 (2014).

[53] J. J. W. Morris, *Chapter 4: Defects in Crystals* (Wiley, 2013).

[54] J. Huang, Z. Yin, Q. Zheng, Applications of ZnO in organic and hybrid solar cells. *Energy Environ. Sci.* **4**, 3861 (2011).

[55] B. Van Zeghbroeck, Carrier Transport. *Princ. Semicond. Devices* (2011), (available at https://ecee.colorado.edu/~bart/book/book/chapter2/ch2_7.htm#2_7_2).

[56] G. Cramer, Fabrication and Comparison of ZnO Thin Film Transistors with Various Gate Insulators. *Electr. Eng. Cooper Union …*, 34–35 (2006).

[57] Y. Liu, Y. Li, H. Zeng, ZnO-based transparent conductive thin films: Doping, performance, and processing. *J. Nanomater.* **2013** (2013), doi:10.1155/2013/196521.

[58] C. J. A. Ashrafi, Review of zincblende ZnO Stability of metastable ZnO phases. *J. Appl. Phys.* **102** (2007).

[59] E. Verrelli, R. J. Gray, M. O'Neill, S. M. Kelly, N. T. Kemp, Microwave oven fabricated hybrid memristor devices for non-volatile memory storage. *Mater. Res. Express*. **1** (2015), doi:10.1088/2053-1591/1/4/046305.

[60] K. Gorshkov, T. Berzina, V. Erokhin, M. P. Fontana, Organic memristor based on the composite materials: Conducting and ionic polymers, gold nanoparticles and graphenes. *Procedia Comput. Sci.* **7**, 248–249 (2011).

[61] B. F. Bory, thesis, Eindhoven, Technische Universiteit (2014).

[62] A. H. Jaafar *et al.*, Reversible optical switching memristors with tunable STDP synaptic plasticity: a route to hierarchical control in artificial intelligent systems. *Nanoscale*. **9**, 17091–17098 (2017).

[63] W. Schilling, Properties of Frenkel defects. *J. Nucl. Mater.* **216**, 45–48 (1994).

[64] G. D. Mahan, Intrinsic defects in ZnO varistors. *J. Appl. Phys.* **54**, 3825–3832 (1983).

[65] J. Han, P. Q. Mantas, A. M. R. Senos, Defect chemistry and electrical characteristics of undoped and Mn-doped ZnO. *J. Eur. Ceram. Soc.* **22**, 49–59 (2002).

[66] Ü. Özgür *et al.*, A comprehensive review of ZnO materials and devices. *J. Appl. Phys.* **98**, 041301 (2005).

[67] A. Younis, D. Chu, S. Li, Evidence of filamentary switching in oxide-based memory devices via weak programming and retention failure analysis. *Sci. Rep.* **5** (2015), doi:10.1038/srep13599.

[68] Y. Chen *et al.*, Polymer memristor for information storage and neuromorphic applications. *Mater. Horizons*. **1**, 489 (2014).

[69] I. Köymen, in *Imperial College London* (2014; https://spiral.imperial.ac.uk/handle/10044/1/39971).

[70] K. Kerur, A study of the memristor, the fourth circuit element. *Simulation* (2010), (available at http://krex.k-state.edu/dspace/bitstream/handle/2097/4605/KetakiKerur2010.pdf;jsessionid=4EC72C0E107D618A453D91A109B76DFB?sequence=3).

[71] R. S. Williams, HP Memristor FAQ. *HP Website* (2012), pp. 3–5.

[72] J. Beckett, Demystifying the memristor. *HP Website* (2008), (available at http://www.hpl.hp.com/news/2008/apr-jun/memristor.html).

[73] B. R. Stanley, W. Posted, How We Found The Missing Memristor. *IEEE Spectr.* **45** (2015), pp. 1–12.

[74] A. G. Radwan, M. E. Fouda, *Memristor: Models, types, and applications* (2015), vol. 26.

[75] B. Mouttet, Programmable crossbar signal processor with rectification layer. *US Pat. App. 20,070/229,111* (2007), pp. 35–47.

[76] S. H. Jo *et al.*, Nanoscale memristor device as synapse in neuromorphic systems. *Nano Lett.* **10**, 1297–1301 (2010).

[77] Y. V. Pershin, M. Di Ventra, Experimental demonstration of associative memory with memristive neural networks. *Neural Networks*. **23**, 881–886 (2010).

[78] W. Grossman, Transistor successor set to bring on The Machine age soon. *Nat. News*. **Online** (2014), p. doi:10.1038/nature.2014.1561, , doi:10.1038/nature.2014.15611.

[79] J. Clark, HP starts a memristor-based space program to launch… THE MACHINE. *Regist.* (2014), (available at

http://www.theregister.co.uk/2014/06/11/hp_memristor_the_machine/).

[80] Q. Hardy, HP Destroys a Dream Computer to Save It. *New York Times website* (2017), (available at https://bits.blogs.nytimes.com/2015/06/03/hp-destroys-a-dream-computer-to-save-it/?_r=2).

[81] F. M. Simanjuntak, D. Panda, K.-H. Wei, T.-Y. Tseng, Status and Prospects of ZnO-Based Resistive Switching Memory Devices. *Nanoscale Res. Lett.* **11**, 368 (2016).

[82] R. Soni *et al.*, On the stochastic nature of resistive switching in Cu doped $Ge_{0.3}Se_{0.7}$ based memory devices. *J. Appl. Phys.* **110**, 054509 (2011).

[83] B. Singh, B. R. Mehta, Relationship between nature of metal-oxide contacts and resistive switching properties of copper oxide thin film based devices. *Thin Solid Films*. **569**, 35–43 (2014).

[84] W. L. Y. Yang, P. Gao, S. Gaba, T. Chang, X. Pan, Observation of conducting filament growth in nanoscale resistive memories. *Nat. Commun.* **2012**, 732 (2012).

[85] Z. L. W. J. Song, Y. Zhang, C. Xu, W. Wu, Polar Charges Induced Electric Hysteresis of ZnO Nano/Microwire for Fast Data Storage. *Nano Lett.* **2011**, 2829 (2011).

[86] J. M. Wang *et al.*, Corrosion and electrochemical behaviors of pure aluminum in novel KOH-ionic liquid-water solutions. *Mater. Corros.* **60**, 977–

981 (2009).

[87] F. Raffone, F. Risplendi, G. Cicero, A New Theoretical Insight Into ZnO NWs Memristive Behavior. *Nano Lett.* **16**, 2543–2547 (2016).

[88] R. Waser, R. Dittmann, G. Staikov, K. Szot, Redox - Based Resistive Switching Memories – Nanoionic Mechanisms , Prospects , and Challenges Redox-Based Resistive Switching Memories – Nanoionic Mechanisms , Prospects , and Challenges. *Adv. Mater.* **21**, 2632–2663 (2009).

[89] N. Onofrio, D. Guzman, A. Strachan, Atomic origin of ultrafast resistance switching in nanoscale electrometallization cells. *Nat. Mater.* **14**, 440–446 (2015).

[90] E. Lim, R. Ismail, Conduction Mechanism of Valence Change Resistive Switching Memory: A Survey. *Electronics*. **4**, 586–613 (2015).

[91] A. Baikalov *et al.*, Field-Driven Hysteretic and Reversible Resistive Switch at the Ag-Pr0.7Ca0.3MnO3 Interface. *Appl. Phys. Lett.* **83**, 957 (2002).

[92] S. Tsui *et al.*, Field-induced resistive switching in metal-oxide interfaces. *Appl. Phys. Lett.* **85**, 317–319 (2004).

[93] A. Sawa, T. Fujii, M. Kawasaki, Y. Tokura, Hysteretic current–voltage characteristics and resistance switching at a rectifying Ti/Pr[sub 0.7]Ca[sub 0.3]MnO[sub 3] interface. *Appl. Phys. Lett.* **85**, 4073 (2004).

[94] R. Fors, S. I. Khartsev, A. M. Grishin, Non-volatile giant resistance switching in metal-insulator-manganite junctions. *Mater. Res. Soc. Symp. Proc.* **830** (2005).

[95] T. Oka, N. Nagaosa, Interfaces of correlated electron systems: Proposed mechanism for colossal electroresistance. *Phys. Rev. Lett.* **95** (2005), doi:10.1103/PhysRevLett.95.266403.

[96] J. Fu *et al.*, Stability and its mechanism in Ag/CoOx/Ag interface-type resistive switching device. *Sci. Rep.* **6**, 35630 (2016).

[97] F. Gul, H. Efeoglu, ZnO and ZnO 1−x based thin film memristors: The effects of oxygen deficiency and thickness in resistive switching behavior. *Ceram. Int.* **43** (2017), pp. 10770–10775.

[98] R. Meyer *et al.*, in *Proceedings - 2008 9th Annual Non-Volatile Memory Technology Symposium, NVMTS 2008* (2008), pp. 54–58.

[99] F. Chiu, A Review on Conduction Mechanisms in Dielectric Films. *Adv. Mater. Sci. Eng.* **2014** (2014), doi:10.1155/2014/578168.

[100] McGraw-Hill, *Fowler–Nordheim Tunneling* (2002).

[101] M. E. Kiziroglou, X. Li, A. A. Zhukov, P. A. J. De Groot, C. H. De Groot, Thermionic field emission at electrodeposited Ni – Si Schottky barriers. *Solid State Electron.* **52**, 1032–1038 (2008).

[102] P. R. Emtage, W. Tantraporn, Schottky emission through thin insulating films. *Phys. Rev. Lett.* **8**, 267–268 (1962).

[103] H. Spahr *et al.*, Conduction mechanisms in thin atomic layer deposited Al 2 O 3 layers. *J. Appl. Phys.* **114**, 183714 (2013).

[104] C. A. Mead, Metal-semiconductor surface barriers. *Solid State Electron.* **9**, 1023–1033 (1966).

[105] Sze, *Physics of Semiconductor Devices* (Wiley, New York, ed. 2nd, 1995), vol. 10.

[106] M. W. Allen, S. M. Durbin, *Appl. Phys. Lett.*, in press, doi:http://dx.doi.org/10.1063/1.2894568.

[107] U. Mishra, J. Singh, *Semiconductor Device Physics and Design* (Springer Science & Business Media, 2007; https://books.google.com/books?id=7WKOfUR-8M4C&pgis=1), vol. 6.

[108] F. P. McCluskey, T. Podlesak, R. Grzybowski, *High Temperature Electronics* (CRC Press, 1996).

[109] L. Kaye, in *Handbook of the Physicochemical Properties of the Elements* (1968; http://dx.doi.org/10.1007/978-1-4684-6066-7_7), pp. 387–446.

[110] J. I. Sohn *et al.*, Engineering of efficiency limiting free carriers and an interfacial energy barrier for an enhancing piezoelectric generation †. *Energy*

Environ. Sci. **6**, 97–104 (2013).

[111] H. R. A. J. K. L. Mittal, *Acid-Base Interactions: Relevance to Adhesion Science and Technology: Festschrift in Honor of the 75th Birthday of Professor F. M. Fowkes* (Utrecht, The Netherlands, 1991).

[112] J. Frenkel, On Pre-Breakdown Phenomena in Insulators and Electronic Semi-Conductors. *Phys. Rev.* **54**, 647 (1938).

[113] J. G. Simmons, Poole-Frenkel effect and Schottky effect in metal-insulator-metal systems. *Phys. Rev.* **155**, 657–660 (1967).

[114] H. Schroeder, Poole-Frenkel-effect as dominating current mechanism in thin oxide films - An illusion?! *J. Appl. Phys.* **117** (2015), doi:10.1063/1.4921949.

[115] R. L. Angle, H. E. Talley, Electrical and Charge Storage Characteristics of the Tantalum Oxide-Silicon Dioxide Device. *IEEE Trans. Electron Devices*. **25**, 1277–1283 (1978).

[116] H. Akinaga, H. Shima, Resistive random access memory (ReRAM) based on metal oxides. *Proc. IEEE*. **98**, 2237–2251 (2010).

[117] S. Akihito, Resistive switching in transition metal oxides. *Materialstoday*. **11**, 28–36 (2008).

[118] V. K. Sangwan *et al.*, Gate-tunable memristive phenomena mediated by grain boundaries in single-layer MoS2. *Nat. Nanotechnol.* **10**, 403–406

(2015).

[119] L. O. C. A. Adamatsky, *Memristor Networks* (Springer International Publishing, Switzerland, 2014; http://link.springer.com/10.1007/978-3-319-02630-5).

[120] J.-P. Colinge, C. A. Colinge, *Physics of Semiconductor Devices* (Springer Science & Business Media, 2005).

[121] W. Brütting, S. Berleb, A. G. Mückl, Space-charge limited conduction with a field and temperature dependent mobility in Alq light-emitting devices. *Synth. Met.* **122**, 99–104 (2001).

[122] N. F. Mott, R. W. Gurney, *Electronic Processes in Ionic Crystals* (Oxford University Press, 1964).

[123] S. A. Moiz, I. A. Khan, W. A. Younis, K. S. Karimov, Space Charge–Limited Current Model for Polymers. *Conduct. Polym.* (2016), doi:10.5772/63527.

[124] C. D. Child, Discharge from hot CaO. *Phys. Rev. (Series I)*. **32**, 492–511 (1911).

[125] M. Bajpai, R. Srivastava, M. N. Kamalasanan, R. S. Tiwari, S. Chand, Charge transport and microstructure in PFO: MEH-PPV polymer blend thin films. *Synth. Met.* **160**, 1740–1744 (2010).

[126] M. N. Awais *et al.*, Resistive-switching and current-conduction mechanisms

in F8BT polymer resistive switch. *Micro Nano Lett.* **11**, 712–714 (2016).

[127] N. Mir, M. Salavati-Niasari, F. Davar, Preparation of ZnO nanoflowers and Zn glycerolate nanoplates using inorganic precursors via a convenient rout and application in dye sensitized solar cells. *Chem. Eng. J.* **181**–**182**, 779–789 (2012).

[128] J. Wang, B. Sun, F. Gao, N. C. Greenham, Memristive devices based on solution-processed ZnO nanocrystals. *Phys. Status Solidi Appl. Mater. Sci.* **207**, 484–487 (2010).

[129] J. C. Simpson, J. F. Cordaro, Characterization of deep levels in zinc oxide. *J. Appl. Phys.* **63**, 1781–1783 (1988).

[130] A. Y. Polyakov *et al.*, Electrical characteristics of Au and Ag Schottky contacts on n-ZnO. *Appl. Phys. Lett.* **83**, 1575–1577 (2003).

[131] P. Mark, T. E. Hartman, On distinguishing between the Schottky and Poole-Frenkel effects in insulators. *J. Appl. Phys.* **39**, 2163–2164 (1968).

[132] P. K. Radtke, L. Schimansky-Geier, A nonlinear HP-type complementary resistive switch. *AIP Adv.* **6** (2016), doi:10.1063/1.4952755.

[133] M. J. Lee *et al.*, A fast, high-endurance and scalable non-volatile memory device made from asymmetric Ta2O5− x/TaO2− x bilayer structures. *Nat. Mater.* **10**, 625–630 (2011).

[134] Knowm, Memristors. *Knowm website* (2017), (available at http://knowm.org/memristors/).

[135] J. C. Scott, L. D. Bozano, Nonvolatile memory elements based on organic materials. *Adv. Mater.* **19**, 1452–1463 (2007).

[136] A. Brown, Digital preservation guidance note 2: Selecting storage media for long-term preservation. *Natl. Arch.*, 7 (2008).

[137] I. Vourkas, D. Stathis, G. C. Sirakoulis, Improved read voltage margins with alternative topologies for memristor-based crossbar memories. *IEEE/IFIP Int. Conf. VLSI Syst. VLSI-SoC*, 336–339 (2013).

[138] H. T. Ng *et al.*, Optical properties of single-crystalline ZnO nanowires on m-sapphire. *Appl. Phys. Lett.* **82**, 2023–2025 (2003).

[139] Y. Zhang, F. Lu, Z. Wang, L. Zhang, Aggregation of ZnO nanorods into films by oriented attachment. *J. Phys. Chem. C*. **111**, 4519–4523 (2007).

[140] J. H. Zheng, Q. Jiang, J. S. Lian, Synthesis and optical properties of flower-like ZnO nanorods by thermal evaporation method. *Appl. Surf. Sci.* **257**, 5083–5087 (2011).

[141] Q. Li *et al.*, Photoluminescence and wetting behavior of ZnO nanoparticles/nanorods array synthesized by thermal evaporation. *J. Alloys Compd.* **560**, 156–160 (2013).

[142] C. W. Litton, D. C. Reynolds, T. C. Collins, *Zinc Oxide Materials for Electronic and Optoelectronic Device Applications* (John Wiley and Sons Ltd, 2011; http://doi.wiley.com/10.1002/9781119991038).

[143] R. Kumar, G. Kumar, O. Al-Dossary, A. Umar, ZnO nanostructured thin films: Depositions, properties and applications—A review. *Mater. Express*. **5**, 3–23 (2015).

[144] R. Nandi, S. S. Major, The mechanism of growth of ZnO nanorods by reactive sputtering. *Appl. Surf. Sci.* **399**, 305–312 (2017).

[145] D. C. Agarwal *et al.*, VLS-like growth and characterizations of dense ZnO nanorods grown by e-beam process. *J. Phys. D. Appl. Phys.* **42** (2009), doi:10.1088/0022-3727/42/3/035310.

[146] E. Chen, Thin Film Deposition. *Harvard Univ. website* (2004), pp. 1–34.

[147] Electron Beam Evaporation: Overview. *Angstrom Eng. website* (2018), (available at https://angstromengineering.com/tech/electron-beam-evaporation/?gclid=Cj0KCQjw5-TXBRCHARIsANLixNywJSODeR4QWzQtONc6jaSzpY25fOmJ3NK_mdxxhnzpqNcvabiRAUkaAuHUEALw_wcB).

[148] Electron Beam Evaporation. *Midwest Tungsten Serv. website* (2003), (available at https://www.tungsten.com/how-does-electron-beam-evaporation-work/).

[149] G. Kumar, R. Kumar, A. Kumar, ZnO Thin Films: Chemical Vapour Deposition, Growth and Functional Properties. *Rev. Adv. Sci. Eng.* **5**, 150–160 (2016).

[150] A.-J. Cheng *et al.*, Thermal chemical vapor deposition growth of zinc oxide nanostructures for dye-sensitized solar cell fabrication. *Appl. Phys. Lett.* **92** (2008), doi:10.1063/1.2889502.

[151] Z. C. Z. Chen, K. S. K. Shum, T. Salagaj, W. Z. W. Zhang, K. Strobl, ZnO thin films synthesized by chemical vapor deposition. *Appl. Technol. Conf. (LISAT), 2010 Long Isl. Syst.*, 4–9 (2010).

[152] A. C. Jones, M. L. Hitchman, *Overview of Chemical Vapour Deposition* (Springer, 2009).

[153] Q. Zhang, D. Sando, V. Nagarajan, Chemical route derived bismuth ferrite thin films and nanomaterials. *J. Mater. Chem. C*. **4**, 4092–4124 (2016).

[154] S. N. L. J.R. Creighton, S. N. L. P. Ho, Introduction to Chemical Vapor Deposition (CVD). *Chem. Vap. Depos. (ASM Int.* (2001), pp. 1–22.

[155] A. C. Cruickshank *et al.*, Electrodeposition of ZnO nanostructures on molecular thin films. *Chem. Mater.* **23**, 3863–3870 (2011).

[156] F. F. Oliveira, M. P. Proenca, J. P. Araújo, J. Ventura, Electrodeposition of ZnO thin films on conducting flexible substrates. *J. Mater. Sci.* **51**, 5589–5597 (2016).

[157] W. D. Wijesooriyage, thesis, Chalmers University of Technology (2011).

[158] M. J. Matlosz, *Fundamental Aspects of Electrochemical Deposition and Dissolution* (2000).

[159] N. Pham, E. Boellard, P. M. Sarro, J. N. Burghartz, Spin, Spray coating and Electrodeposition of photoresist for MEMS structures–A comparison. *… Adv. Futur. …*, 81–86 (2002).

[160] M. Poornajar, P. Marashi, D. H. Fatmehsari, M. K. Esfahani, Synthesis of XnO Nanorods via Chemical Bath. *Ceram. Int.*, 1–28 (2015).

[161] V. Strano *et al.*, Double role of HMTA in ZnO nanorods grown by chemical bath deposition. *J. Phys. Chem. C*. **118**, 28189–28195 (2014).

[162] A. Mason *et al.*, Investigation of growth parameter influence on hydrothermally grown ZnO nanowires using a research grade microwave. *2009 Int. Semicond. Device Res. Symp.*, 1–2 (2009).

[163] A. Sugunan, H. C. Warad, M. Boman, J. Dutta, Zinc oxide nanowires in chemical bath on seeded substrates: Role of hexamine. *J. Sol-Gel Sci. Technol.* **39**, 49–56 (2006).

[164] B. Weintraub, Z. Zhou, Y. Li, Y. Deng, Solution synthesis of one-dimensional ZnO nanomaterials and their applications. *Nanoscale*. **2**, 1573–1587 (2010).

[165] † Lori E. Greene *et al.*, General Route to Vertical ZnO Nanowire Arrays

Using Textured ZnO Seeds. *Nano Lett.* **5**, 1231–1236 (2005).

[166] U. of W. S. Swapp, Scanning Electron Microscopy (SEM). *Carlet. Coll.* (2017), (available at http://serc.carleton.edu/research_education/geochemsheets/techniques/SEM.html).

[167] G. Binnig, C. F. Quate, C. C. N.-P. Gerber, Atomic Force Microscope. *Phys. Rev. Lett.* **56**, 930–933 (1986).

[168] Y. Martin, C. C. Williams, H. K. Wickramasinghe, Atomic force microscope-force mapping and profiling on a sub 100-Å scale. *J. Appl. Phys.* **61**, 4723–4729 (1987).

[169] Bruker, Tapping Mode AFM. *Bruker website* (2012), p. 2011.

[170] N. Xu *et al.*, Characteristics and mechanism of conduction / set process in TiN / ZnO / Pt resistance switching random-access memories. *Appl. Phys. Lett.* **92**, 1–4 (2008).

[171] K. Campbell, The Trouble with Oxide-Based Memristors. *Knowm website* (2015), (available at https://knowm.org/the-trouble-with-oxide-based-memristors/).

[172] D. Y. G. Y. Zhang, M. K. Ram, E. K. Stefanakos, Synthesis, Characterization and Applications of ZnO Nanowires. *J. Nanomater.* **2012** (2012).

[173] S. Xu, C. Lao, B. Weintraub, Z. L. Wang, Density-controlled growth of aligned ZnO nanowire arrays by seedless chemical approach on smooth surfaces. *J. Mater. Res.* **23**, 2072–2077 (2008).

[174] N. D. Alikakos, G. Fusco, G. Karali, Ostwald ripening in two dimensions - The rigorous derivation of the equations from the Mullins-Sekerka dynamics. *J. Differ. Equ.* **205**, 1–49 (2004).

[175] R. Viswanatha, H. Amenitsch, D. D. Sarma, Growth Kinetics of ZnO Nanocrystals : A Few Surprises. *J. Am. Chem. Soc.* **129**, 4470–4475 (2007).

[176] A. D. Raj, P. S. Kumar, D. Nataraj, D. Mangalaraj, Growth and characterization of ZnO nanostructured thin films by a two step chemical method. *Appl. Surf. Sci.* **255**, 2382–2387 (2008).

[177] P. Ghosh, A. K. Sharma, Optical characterization and growth mechanism of combination of zinc oxide nanowires and nanorods at various substrate temperatures. *J. Nanomater.* **2013**, 1–9 (2013).

[178] B. B. He, *Two-dimensional X-ray diffraction* (John Wiley & Sons, 2009).

[179] M. Howdyshell, Structure of ZnO Nanorods using X-Ray Diffraction. *Albion Coll. Stanford Linear Accel. Center, Stanford, Calif.* (2007), (available at http://www.slac.stanford.edu/cgi-wrap/getdoc/slac-tn-07-024.pdf).

[180] L. J. Brillson, Y. Lu, ZnO Schottky barriers and Ohmic contacts. *J. Appl. Phys.* **109** (2011), doi:10.1063/1.3581173.

[181] M. Laurenti, S. Porro, C. F. Pirri, C. Ricciardi, A. Chiolerio, Zinc Oxide Thin Films for Memristive Devices: A Review. *Crit. Rev. Solid State Mater. Sci.* **42**, 153–172 (2017).

[182] S. P. Heluani, G. Braunstein, M. Villafuerte, G. Simonelli, S. Duhalde, Electrical conductivity mechanisms in zinc oxide thin films deposited by pulsed laser deposition using different growth environments. *Thin Solid Films*. **515**, 2379–2386 (2006).

[183] P. E. Gaillardon, D. Sacchetto, S. Bobba, Y. Leblebici, G. De Micheli, GMS: Generic memristive structure for non-volatile FPGAs. *IEEE/IFIP Int. Conf. VLSI Syst. VLSI-SoC*. **07**–**10**–**Octo**, 94–98 (2015).

[184] A. Thomas *et al.*, Tunnel junction based memristors as artificial synapses. *Front. Neurosci.* **9** (2015), doi:10.3389/fnins.2015.00241.

[185] Q. Xia, J. J. Yang, W. Wu, X. Li, R. S. Williams, Self-aligned memristor cross-point arrays fabricated with one nanoimprint lithography step. *Nano Lett.* **10**, 2909–2914 (2010).

[186] E. Gale, R. Mayne, A. Adamatzky, B. De Lacy Costello, Drop-coated titanium dioxide memristors. *Mater. Chem. Phys.* **143**, 524–529 (2014).

[187] J. Sheils, The Electric Vocabulary. *Phys. Educ.* **47**, 78–86 (2012).

[188] J. Lesurf, thesis, University of St. Andrews (2006).

[189] G. A. Gibson *et al.*, An accurate locally active memristor model for S-type negative differential resistance in NbOx. *Appl. Phys. Lett.* **108** (2016), doi:10.1063/1.4939913.

[190] S. K. Thangaraju, K. M. Munisamy, Electrical and joule heating relationship investigation using finite element method. *IOP Conf. Ser. Mater. Sci. Eng.* **88** (2015), doi:10.1088/1757-899X/88/1/012036.

[191] N. A. A. Shaari, N. S. M. Sauki, S. H. Herman, Effect of annealing time on memristive behavior of sol-gel spincoated ZnO-based memristive device. *AIP Conf. Proc.* **1774** (2016), doi:10.1063/1.4965105.

[192] C. Awino, V. Odari, T. Sakwa, Investigation of Structural and Electronic Properties of CH3NH3PbI3 Stabilized by Varying Concentrations of Poly(Methyl Methacrylate) (PMMA). *Coatings*. **7**, 115 (2017).

[193] V. Quemener, thesis, University of Oslo (2012).

[194] O.Madelung, M.Schulz, H.Weiss, *Semiconductors: Physics of II-VI and I-VII compounds, Semimagnetic Semiconductors* (Springer-Verlag Berlin Heidelberg, ed. 1, 1982).

[195] C. Ravidhas, C. Sanjeeviraja, thesis, Alagappa University (2015).

[196] E. Lee *et al.*, Direct Electron Injection into an Oxide Insulator Using a Cathode Buffer Layer. *Nat. Commun.* **6**, 1–6 (2015).

[197] S. M. Sayyah, A. B. Khaliel, H. Moustafa, Electronic structure and ground state properties of PMMA polymer: I. Step-by-step formation and stereo-regularity of the polymeric chain - AM1-MO treatment. *Int. J. Polym. Mater. Polym. Biomater.* **54**, 505–518 (2005).